



**Faculty of Graduate Studies**

**Innovative Electrochemical Investigation of Pharmaceuticals' Removal Using  
Iron Nanoparticles in Aqueous Solutions**

البحث الكهروكيميائي المبتكر في ازالة المستحضرات الصيدلانية باستخدام جزيئات الحديد النانوية للمحاليل  
المائية

This thesis was submitted in partial fulfillment of the requirements for the

**Master's Degree in Applied Chemistry**

From the Faculty of Graduate Studies at Birzeit University, Palestine

**Sojood Mahmoud Darwish**

**1195226**

**Supervisor:**

**Dr. Intiaz Darwish**

**2021/2022**

**Innovative Electrochemical Investigation of Pharmaceuticals' Removal Using  
Iron Nanoparticles in Aqueous Solutions**

**By**

**Sojood Mahmoud Darwish**

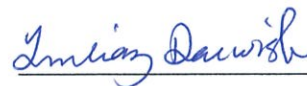
This thesis was defended successfully on 30/6/2022 and approved by:

Committee Members

Signature

**Dr. Imtiaz Darwish**

Supervisor  
Chemistry Department-Faculty Member  
Birzeit University



**Dr. Talal Shahwan**

Committee Member  
Chemistry Department-Faculty Member  
Birzeit University



**Dr. Ghassan Barghouti**

Committee Member  
Chemistry Department-Faculty Member  
Birzeit University



## Acknowledgement

---

**First and foremost, praise and appreciation to God, the Almighty, for showering His blessings on me throughout my study effort, allowing me to successfully complete the research.**

**There are no words to express the gratitude that I have for my supervisor, Dr. Intiaz Darwish, for allowing me to conduct research and providing me with invaluable guidance throughout this process. Her vision, genuineness, and motivation have carried me throughout all stages of my thesis. She showed me how to conduct research and present my findings in the most clear and concise manner possible. I was honored to have the privilege of working and studying under her supervision.**

**Apart from my adviser, I'd like to express my gratitude to the members of my thesis committee: Dr. Talal Shawan and Dr. Ghassan Barghouti, for their support, and insightful comments.**

**I owe my mom a debt of gratitude for her love, prayers, care, and sacrifices in teaching me to be the best version of myself. I also want to thank my sister Wafaa for her unwavering support and prayers and being an inspiration that has helped me complete the research work, whether directly or indirectly.**

**Last but not least, I want to express my deepest thanks and sincere appreciation to my friend Nardeen for her endless support and her encouragement until this research came to existence.**

## Table of Contents

Acknowledgement .....	III
Table of Contents .....	V
List of Abbreviations .....	VII
List of Schemes .....	V
List of Figures .....	VI
List of Tables .....	X
Abstract .....	XI
ملخص الرسالة بالعربية .....	XII
Chapter One: Theory and Introduction .....	1
1.1 <i>Water Pollution</i> .....	3
1.2 <i>Diclofenac Sodium</i> .....	5
1.3 <i>Mefenamic Acid</i> .....	7
1.4 <i>Electrolysis of Water</i> .....	9
1.5 <i>Nanoparticles</i> .....	10
1.6 <i>Electrochemical Techniques</i> .....	12
1.6.1 <i>Voltammetric Techniques</i> .....	13
1.6.2 <i>Electrochemical Cell</i> .....	13
1.6.3 <i>Diffusion Layer</i> .....	15
1.6.4 <i>Cyclic Voltammetry</i> .....	18
1.6.5 <i>Linear Sweep Voltammetry</i> .....	21
1.6.6 <i>Square Wave Voltammetry</i> .....	22
1.7 <i>The Aim of This Study</i> .....	25
Chapter Two: Experimental .....	26
2.    Experimental .....	27
2.1 <i>Materials</i> .....	27
2.2 <i>Samples' preparations</i> .....	27
2.3 <i>Synthesis of Iron (IV) Oxide and Zero Valent Iron Nanoparticles</i> .....	28

2.4	<i>Working procedure</i> .....	31
2.5	<i>Apparatus and Software/instrumentation</i> .....	32
2.6	<i>Analytical method</i> .....	33
Chapter Three: Results and Discussion.....		35
3.	Results and Discussion.....	36
3.1	<i>Conditions Optimization</i> .....	36
3.1.1	<i>Type of electrode</i> .....	36
3.1.2	<i>Effect of NPs Amount</i> .....	37
3.1.3	<i>Effect of time</i> .....	39
3.1.4	<i>Effect of Scan Rate</i> .....	48
3.1.5	<i>Effect of pH</i> .....	55
3.1.6	<i>Effect of Temperature</i> .....	64
3.2	<i>Electrochemical Characterization of MFA</i> .....	67
3.3	<i>Electrochemical Characterization of DCF Drug</i> .....	68
3.4	<i>Physicochemical characterizations DCF drug</i> .....	72
3.4.1	<i>IR Characterization</i> .....	72
3.4.2	<i>SEM and TEM characterization</i> .....	76
3.5	<i>Calibration Curves of the pharmaceutical's removal using NPs</i> .....	76
3.5.1	<i>Calibration Curves of DCF</i> .....	76
3.5.2	<i>Calibration Curves of MFA</i> .....	82
3.6	<i>Percentage Removal of Pharmaceuticals Using NPs</i> .....	89
3.6.1	<i>Percentage removal of DCF using nZVI and IO-NPs</i> .....	89
3.6.2	<i>Percentage Removal of MFA using nZVI and IO-NPs</i> .....	90
3.7	<i>Drug Adsorption</i> .....	92
Chapter Four: Conclusion .....		100
4.	Conclusion .....	100
Chapter Five: Future Studies and Recommendations .....		102
5.	Recommendations:.....	102
Bibliography.....		105

## List of Abbreviations

A	Amperes
Å	Angstroms
Ag	Silver
AgCl	Silver Chloride
aq	Aqueous
C	Concentration
CE	Counter electrode
CV	Cyclic Voltammetry
D	Diffusion Coefficient
DCF	Diclofenac
e <sup>-</sup>	Electrons
EDL	Electrochemical double layer
Emf	Electromotive force
E <sub>pa</sub>	Anodic peak potential
DigiSim®	Digital Simulation
E <sub>pc</sub>	Cathodic peak potential
E <sub>sw</sub>	Symmetrical wave pulse amplitude
ETs	Electrochemical techniques
EU	European Union
F	Faraday's Constant
f	Frequency
FAAS	Flame atomic absorption spectrometry
Fe <sub>2</sub> O <sub>3</sub>	Iron (III)Oxide
Fe <sub>3</sub> O <sub>4</sub>	Iron (IV)Oxide
FeO	Iron (II) Oxide
FL	Fluorescence
FT-IR	Fourier Transform Infrared
g	Gas
GCE	Glassy Carbon Electrode
H <sub>2</sub>	Hydrogen
H <sub>2</sub> O	Water
H <sub>2</sub> O <sub>2</sub>	Hydrogen Peroxide
HOMO	Highest Occupied Molecular Orbital
HPLC	High Performance Liquid Chromatography
I <sub>c</sub>	Charging Current
ICP-AES	Inductively coupled plasma atomic emission spectroscopy
IEP	Isoelectric point
I <sub>for</sub>	Forward current

IHP	Inner Helmholtz plane
$I_{\text{net}}$	Net current
IO-NPs	Iron Oxide nanoparticles
$I_p$	Potential peak
$I_p$	Peak current
$I_p^a$	Anodic peak current
$I_p^c$	Cathodic peak current
$I_{\text{rev}}$	Reverse current
K	Kelvin
$K^0$	Equilibrium constant
KBr	Potassium Bromide p48
KCL	Potassium Chloride
kJ	KiloJoules
l	Liquid
LSV	Linear Sweep Voltammetry
LUMO	Lowest Occupied Molecular Orbital
MFA	Mefenamic Acid
MRI	Magnetic Resonance Imaging
N	Stoichiometric number of electrons
$\text{Na}_2\text{HPO}_4$	Sodium Hydrogen Phosphate
$\text{NaBH}_4$	Sodium Borohydride
$\text{NaH}_2\text{PO}_4$	Sodium dihydrogen phosphate
NPs	Nanoparticles
NSAIDs	Non-steroidal anti-inflammatory drugs
$\text{O}_2$	Oxygen
$\text{O}_3$	Ozone
OHP	Outer Helmholtz plane
PBS	Phosphate buffer solution
R	Gas constant
RE	Reference electrode
$R^2$	Coefficient of determination
sol	Solution
SW	Square wave
SWV	Square wave voltammetry
T	Temperature
UV	Ultraviolet
V	Volts
v	Scan rate
VTs	Voltammetry techniques
WE	Working electrode
nZVI	Zero valent iron nanoparticles
$\Delta G^\circ$	Gibbs Free Energy
$\Delta H^\circ$	Enthalpy change
$\tau$	Time



## List of Schemes

SCHEME 1: DCF DRUG FORMS AT DIFFERENT PH VALUES-----	55
SCHEME 2: MEFENAMIC ACID FORMS AT DIFFERENT PH VALUES -----	61
SCHEME 3: REACTIONS FOR THE ELECTRO-OXIDATION OF DCF (MEKASSA ET AL. 2018) -----	71
SCHEME 4: IO-NPS -MEFENAMIC POSSIBLE INTERACTION MODEL UNDER ACIDIC MEDIA -----	94
SCHEME 5: MAGNETIC NANOPARTICLES SCHEMATIC MODEL (NZVI, AND $Fe_3O_4$ ). -----	95
SCHEME 6: NZVI –DCF POSSIBLE INTERACTION MODEL AT ACIDIC AND BASIC MEDIA -----	97
SCHEME 7: PROPOSED SMALL EXPERIMENTAL STATION OF NZVI ADSORBENT PACKED INSIDE A GLASS COLUMN -----	104

## List of Figures

- FIGURE 1: A VOLTAMMETRIC CELL SCHEME WHICH SHOWS THE CURRENT FLOWS BETWEEN THE SMALL WORKING ELECTRODE (WE) AND THE LARGE COUNTER ELECTRODE (CE). THE POTENTIOSTAT IS USED TO ADJUST THE POTENTIAL OF THE WORKING ELECTRODE IN COMPARISON TO THE CONSTANT POTENTIAL OF THE ROBUST REFERENCE ELECTRODE (RE). \_\_\_\_\_ 14
- FIGURE 2: SCHEMATIC OF THE ELECTRIC DOUBLE LAYER AT THE ELECTRODE|ELECTROLYTE INTERFACE AT A NEGATIVELY CHARGED ELECTRODE \_\_\_\_\_ 17
- FIGURE 3: A) TYPICAL POTENTIAL VARIATION AND B) THE SHAPE OF THE I-E CURVE IN THE POPULAR TECHNIQUE KNOWN AS CYCLIC VOLTAMMETRY WHERE  $I_p^C$  AND  $I_p^A$  ARE THE CATHODIC AND ANODIC PEAK CURRENT, AND  $E_p^C$  AND  $E_p^A$  ARE THE CATHODIC AND ANODIC PEAK POTENTIALS \_\_\_\_\_ 19
- FIGURE 4: IN THE COMMON TECHNIQUE KNOWN AS CYCLIC VOLTAMMETRY, (A) TYPICAL POTENTIAL FLUCTUATION BY VARYING THE ELECTRODE POTENTIAL IN THE SIMPLEST LINEAR FASHION FROM CERTAIN STARTING ( $E_s$ ) TO THE FINAL ( $E_f$ ) POTENTIAL. AND (B) THE FORM OF THE I-E CURVE ARE SHOWN. THE LATTER IS LINKED TO THE FORMAL POTENTIAL ( $E^\ominus$ ), WHICH IS A CRUCIAL THERMODYNAMIC PARAMETER FOR THE ELECTRODE PROCESS. THE MAXIMUM OF THE ASYMMETRIC PEAK-SHAPED VOLTAMMOGRAM, IS DEFINED BY THE PEAK-CURRENT ( $I_{p,A}$ ) AND THE PEAK-POTENTIAL ( $E_{p,A}$ ) \_\_\_\_\_ 20
- FIGURE 5: A) TYPICAL POTENTIAL FLUCTUATION BY VARYING THE ELECTRODE POTENTIAL IN THE SIMPLEST LINEAR FASHION FROM CERTAIN STARTING ( $V_1$ ) TO THE FINAL ( $V_2$ ) POTENTIAL B) TYPICAL VOLTAMMOGRAM CREATED BY CHANGING THE ELECTRODE POTENTIAL IN THE SIMPLEST LINEAR WAY FROM A SPECIFIC BEGINNING ( $V_1$ ) TO A SPECIFIC FINAL ( $V_2$ ) POTENTIAL. \_\_\_\_\_ 22
- FIGURE 6: SINGLE POTENTIAL CYCLE IN SQUARE-WAVE \_\_\_\_\_ 23
- FIGURE 7: A POTENTIAL WAVEFORM IN SWV IS SHOWN. THE DURATION OF THE POTENTIAL STEP (T) AND THE SCAN INCREMENT OF THE STAIRCASE POTENTIAL ( $\Delta E^\ominus$ ) ARE SHOWN IN THE INSET. A NORMAL SWV IS ALSO SHOWN COMPARED TO CV. \_\_\_\_\_ 24
- FIGURE 8: SYNTHESIS OF IRON (IV) OXIDE NANOPARTICLES WHICH STARTS BY MIXING FERROUS CHLORIDE AND FERRIC CHLORIDE IN A THREE-NECK VOLUMETRIC ROUND FLASK AND FOLLOWED BY ADDING AMMONIA. THE MIXTURE WAS KEPT AT AROUND 60 °C WITH A CONTINUOUS MIXING FOR TWO HOURS. NPS WERE COLLECTED AFTER USING SUCTION FILTRATION AND WERE KEPT OVERNIGHT IN A DESICCATOR. \_\_\_\_\_ 29
- FIGURE 9: SYNTHESIS OF NZVI WHICH STARTS BY MIXING FERRIC CHLORIDE HEXAHYDRATE IN A SOLUTION OF DE-OXYGENATED MILLI-Q WATER AND ABSOLUTE ETHANOL WITH A VOLUME RATIO OF 1:4 IN A THREE-NECK VOLUMETRIC ROUND FLASK AND FOLLOWED BY ADDING THE REDUCING AGENT AFTER DISSOLVING FERRIC CHLORIDE. NPS WERE COLLECTED AFTER USING SUCTION FILTRATION AND WERE KEPT OVERNIGHT IN A DESICCATOR. \_\_\_\_\_ 31

FIGURE 10: A REPRESENTATION IMAGE OF ELECTROCHEMICAL INSTRUMENTATION SETUP	33
FIGURE 11: CV RESPONSE FOR REMOVING 40 MG/L MFA USING GLASSY CARBON ELECTRODE (BLUE CV) AND GOLD WORKING ELECTRODE (ORANGE CV) AFTER ADDING 0.08 G OF IO-NPS IN THE AQUEOUS SOLUTION AT PH 10.06 IN 0.1 M KCL USING GCE, SURFACE AREA (0.069 CM <sup>2</sup> ), 300 MV/S	37
FIGURE 12: CV RESPONSE OF THE IO-NPS AMOUNT EFFECT RANGING FROM 0.04 TO 0.12 G ON THE PEAK CURRENT OF 40 MG/L MFA USING GCE AT PH 7.02 IN 0.1 M KCL USING GCE, SURFACE AREA (0.069 CM <sup>2</sup> ), 300 MV/S	39
FIGURE 13: CV RESPONSE FOR REMOVING 40 MG/L DCF AFTER ADDING 0.08 G OF ZVNPS AT PH 7.02 IN 0.1 M KCL USING GCE, SURFACE AREA (0.069 CM <sup>2</sup> ), 300 MV/S.	40
FIGURE 14: SWV FOR 40 MG/L DCF WITH AND WITHOUT NZVI IN 0.1M KCL AT GC ELECTRODE, IN A PH SOLUTION OF 7.02. SW AMPLITUDE, 25.0 MV; SW STEP, 4.0 MV; SW FREQUENCY, 15.0 HZ.	41
FIGURE 15: TIME PROFILE OF 20 MG/L DCF REMOVAL PERCENTAGE AT 0.45 V	43
FIGURE 16: CV RESPONSE FOR A TIME PROFILE FOR REMOVING 40 MG/L DCF AFTER ADDING 0.08 G OF IO-NPS AT PH 7.02 IN 0.1 M KCL USING GCE, SURFACE AREA (0.069 CM <sup>2</sup> ), 300 MV/S.	44
FIGURE 17: TIME PROFILE OF 40 MG/L MFA REMOVAL PERCENTAGE AT 0.74 V BY ADDING 0.08 G NZVI AT PH 7.02 IN 0.1 M KCL USING GCE, SURFACE AREA (0.069 CM <sup>2</sup> ), 300 MV/S.	46
FIGURE 18: CV RESPONSE FOR TIME PROFILE OF REMOVING 40 MG/L MFA USING 0.08 G OF NZVI AT PH 7.02 IN 0.1 M KCL USING GCE, SURFACE AREA (0.069 CM <sup>2</sup> ), 300 MV/S.	47
FIGURE 19: CV RESPONSE FOR TIME PROFILE OF REMOVING 40 MG/L MFA USING 0.08 G OF IO-NPS AT PH 7.02 IN 0.1 M KCL USING GCE, SURFACE AREA (0.069 CM <sup>2</sup> ), 300 MV/S.	48
FIGURE 20: THE EFFECT OF SCAN RATE ON THE ANALYTE'S CONCENTRATION IN LSV METHOD	49
FIGURE 21: CURRENT VS SCAN RATE FOR DCF REMOVAL USING IO-NPS AFTER 8 MINUTES, AT 0.41 V POTENTIAL, AND 10 <sup>-5</sup> SENSITIVITY AT DIFFERENT SCAN RATES (0.2, 0.18, 0.16, 0.14, 0.1, 0.08, 0.04, AND 0.02 V/S)	51
FIGURE 22: EFFECT OF SCAN RATE ON 40 MG/L DCF REMOVAL USING IO-NPS. SCAN RATE IS RANGING FROM 0.02 TO 0.2 V/S ON THE PEAK CURRENT OF 40 MG/L MFA USING GCE AT PH 7.02 IN 0.1 M KCL USING GCE, SURFACE AREA (0.069 CM <sup>2</sup> ), 300 MV/S	52
FIGURE 23: LSV RESPONSE ON THE PEAK CURRENT OF 40 MG/L DCF AT PH 7.02 IN 0.1 M KCL USING GCE, SURFACE AREA (0.069 CM <sup>2</sup> ) AT DIFFERENT SCAN RATES (0.04-0.2 V/S)	53
FIGURE 24: PEAK CURRENT VS SQUARE ROOT OF SCAN RATE WHICH WAS OBTAINED FROM LSV RESPONSE OF THE IO-NPS ON THE PEAK CURRENT OF 40 MG/L DCF AT PH 7.02 IN 0.1 M KCL USING GCE, SURFACE AREA (0.069 CM <sup>2</sup> ), 300 MV/S	54

- FIGURE 25: LSV RESPONSE FOR EFFECT OF PH ON 40 MG/L DCF REMOVAL USING 0.08 G OF IO-NPS IN A PH 4.04 IN 0.1 M KCL USING GCE, SURFACE AREA (0.069 CM<sup>2</sup>), 300 MV/S. \_\_\_\_\_ 58
- FIGURE 26: CV RESPONSE FOR EFFECT OF IO-NPS ON 40 MG/L DCF REMOVAL USING PH 4.04 AND 7.02 BUFFER SOLUTIONS IN 0.1 M KCL USING GCE, SURFACE AREA (0.069 CM<sup>2</sup>), 300 MV/S. \_\_\_\_\_ 59
- FIGURE 27: LSV RESPONSE FOR EFFECT OF PH ON 10 MG/L MFA REMOVAL USING 0.08 G OF IO-NPS IN A PH 10.06 AND 7.02 IN 0.1 M KCL USING GCE, SURFACE AREA (0.069 CM<sup>2</sup>), 150 MV/S. \_\_\_\_\_ 62
- FIGURE 28: CV RESPONSE FOR EFFECT OF PH ON 40 MG/L MFA REMOVAL IN A PH 4.04 IN 0.1 M KCL USING GCE, SURFACE AREA (0.069 CM<sup>2</sup>), 150 MV/S. \_\_\_\_\_ 64
- FIGURE 29: A LSV RESPONSE OF THE EFFECT OF TEMPERATURE 10°C ON THE PEAK CURRENT OF 40, 30, 20, 10, AND 5 MG/L M DCF AFTER ADDING 0.08 G OF NZVI IN THE AQUEOUS SOLUTION AT PH 7.02 IN 0.1 M KCL USING GCE, SURFACE AREA (0.069 CM<sup>2</sup>), 150 MV/S \_\_\_\_\_ 65
- FIGURE 30: A LSV RESPONSE OF THE EFFECT OF TEMPERATURE 10°C ON THE PEAK CURRENT OF 20 MG/L DCF AFTER ADDING 0.08 G OF IO-NPS IN THE AQUEOUS SOLUTION AT PH 7.02 IN 0.1 M KCL USING GCE, SURFACE AREA (0.069 CM<sup>2</sup>), 300 MV/S \_\_\_\_\_ 66
- FIGURE 31: LSV RESPONSE OF 40 MG/L MFA IN A IN A PH 7.01 IN 0.1 M KCL USING GCE, SURFACE AREA (0.069 CM<sup>2</sup>), 150 MV/S. \_\_\_\_\_ 67
- FIGURE 32: CV OF 40 MG/L DCF IN A IN A PH 7.02 IN 0.1 M KCL USING GCE, SURFACE AREA (0.069 CM<sup>2</sup>), SCAN RATE OF 300 MV/S, AND OVER A POTENTIAL RANGE FROM 0.3 TO 0.9 V \_\_\_\_\_ 69
- FIGURE 33: FOURIER TRANSFORM INFRARED SPECTROSCOPY (FTIR) SPECTRA: (BLUE) DICLOFENAC SODIUM DCF; (RED)-FE<sub>3</sub>O<sub>4</sub> PARTICLES WITH KBR; AND (GREEN) IS FE<sub>3</sub>O<sub>4</sub> WITH BOTH KBR AND DCF. \_\_\_\_\_ 73
- FIGURE 34: FOURIER TRANSFORM INFRARED SPECTROSCOPY (FTIR) SPECTRA: (BLUE) DICLOFENAC SODIUM DCF; (RED)-NZVI WITH KBR; AND (GREEN) IS NZVI WITH BOTH KBR AND DCF. \_\_\_\_\_ 75
- FIGURE 35: CVS OF 40 MG/L DCF IN IN A PH 7.02 PBS IN 0.1 M KCL USING GCE, SURFACE AREA (0.069 CM<sup>2</sup>), 300 MV/S. WITH AND WITHOUT IO-NPS \_\_\_\_\_ 77
- FIGURE 36: CALIBRATION CURVE FOR DCF REMOVAL USING IO-NPS AFTER 8 MINUTES, IN A PH 7.02 IN 0.1 M KCL. THE POTENTIAL WAS KEPT AT 0.4100V \_\_\_\_\_ 78
- FIGURE 37: LSV RESPONSE OF AN OVERLAY OF DIFFERENT CONCENTRATIONS OF DCF AFTER USING NZVI IN A IN A PH 7.02 IN 0.1 M KCL USING GCE, SURFACE AREA (0.069 CM<sup>2</sup>), SCAN RATE OF 300 MV/S OVER A POTENTIAL RANGE OF 0.6 TO 0.3 V \_\_\_\_\_ 80
- FIGURE 38: CALIBRATION CURVE FOR DCF REMOVAL USING NZVI IN A IN A PH 7.02 IN 0.1 M KCL USING GCE, SURFACE AREA (0.069 CM<sup>2</sup>), SCAN RATE OF 300 MV/S, AFTER 8 MINUTES, AT 0.40V POTENTIAL. \_\_\_\_\_ 81
- FIGURE 39: CVS RESPONSE OF 40 MG/L MFA AFTER USING NZVI IN A IN A PH 7.02 IN 0.1 M KCL USING GCE, SURFACE AREA (0.069 CM<sup>2</sup>), SCAN RATE OF 300 MV/S OVER A POTENTIAL RANGE OF 0.6 TO 0.3 V WITH AND WITHOUT IO-NPS \_\_\_\_\_ 83

FIGURE 40: CALIBRATION CURVE FOR MFA REMOVAL USING IO-NPS IN A PH 7.02 IN 0.1 M KCL USING GCE, SURFACE AREA (0.069 CM <sup>2</sup> ), SCAN RATE OF 300 MV/S, AFTER 7 MINUTES, AT 0.74V POTENTIAL, AND 10 <sup>-5</sup> SENSITIVITY	84
FIGURE 41: CV OF 30 MG/L MFA IN A PH 7.02 IN 0.1 M KCL USING GCE, SURFACE AREA (0.069 CM <sup>2</sup> ), SCAN RATE OF 300 MV/S OVER A POTENTIAL RANGE OF 0.4 TO 1.0 V WITH AND WITHOUT NZVI	86
FIGURE 42: CALIBRATION CURVE FOR MFA REMOVAL USING NZVI AFTER 7 MINUTES, AT 0.71 V POTENTIAL, AND 10 <sup>-5</sup> SENSITIVITY	87
FIGURE 43: DCF CONCENTRATION VS REMOVAL PERCENTAGE EFFICIENCY USING 0.08 G OF NZVI AND IO-NPS AFTER 8 MINUTES	90
FIGURE 44: MFA CONCENTRATION VS PERCENTAGE EFFICIENCY REMOVAL USING NZVI AND IO-NPS	92
FIGURE 45: ADSORPTION MECHANISM OF DCF DRUG ON IRON PARTICLES (AL-ABBASSI ET AL. 2020)	98
FIGURE 46: A COMPUTER- OPTIMIZED DCF DRUG THAT CONSTRUCTS HOMO & LUMO ORBITS (AL-ABBASSI ET AL. 2020)	98

## List of Tables

TABLE 1: PHYSICAL, CHEMICAL PROPERTIES OF DCF. _____	6
TABLE 2: PHYSICAL, CHEMICAL PROPERTIES OF MFA. _____	7
TABLE 3: TIME PROFILE OF DCF REMOVAL USING 0.08 G OF NZVI AND IO-NPS _____	42
TABLE 4: TIME PROFILE OF MFA REMOVAL USING NPS _____	45
TABLE 5: CHARACTERISTICS OF CALIBRATION CURVES FOR DCF REMOVAL USING IO-NPS AND NZVI _____	82
TABLE 6: CHARACTERISTICS OF CALIBRATION CURVES FOR MFA REMOVAL USING IO-NPS AND NZVI _____	88
TABLE 7: CALCULATED REMOVAL EFFICIENCY PERCENTAGES OF DCF USING 0.08 G FROM BOTH NZVI AND _____	89
TABLE 8: CALCULATED REMOVAL EFFICIENCY PERCENTAGES REMOVAL OF MFA USING 0.08 G FROM EACH OF NZVI AND IO-NPS _____	91

## Abstract

---

The goal of this project was to utilize electrochemical techniques for pharmaceuticals removal from wastewater aqueous solutions in the presence of nanoparticles (NPs). The removal of these chemicals is crucial in order to assess potential risks to human health through exposure to pharmaceuticals. Recently, electrochemical techniques have gained popularity due to their many advantageous properties including speed, selectivity, sensitivity, precision, and portability. To achieve the goal of this research, aqueous solutions with various concentrations were prepared. The concentrations were quantified using electrochemical techniques. Later, the effect of adding zero valent and iron oxide NPs to the solution was investigated and the results were compared due to the NPs addition. It was anticipated that the electrochemical current peak of the chemical is quenched upon NPs addition. Initially, cyclic voltammetry (CV) was applied under study without the NPs, and the process were repeated after the NP addition to scan the electrochemical current. As a result, the current signal was decreased due to the chemical interaction with NPs. During this investigation, mefenamic acid (MFA) and diclofenac (DCF) were selected as model pharmaceuticals. For the analysis, various variables such as chemical time, pH, and type of NP were monitored and optimized.

## ملخص الرسالة بالعربية

الهدف من هذا المشروع هو استخدام التقنيات الكهروكيميائية لإزالة المستحضرات الصيدلانية من المحاليل المائية لمياه الصرف الصحي في وجود الجسيمات النانوية (NPs). إن إزالة هذه المواد الكيميائية أمر بالغ الأهمية لتقييم المخاطر المحتملة على صحة الإنسان من خلال التعرض للمستحضرات الصيدلانية. في الأونة الأخيرة ، اكتسبت التقنيات الكهروكيميائية شعبية بسبب العديد من الخصائص المفيدة بما في ذلك السرعة والانتقائية والحساسية والدقة وقابلية النقل. لتحقيق هدف هذا البحث تم تحضير محاليل مائية بتركيزات مختلفة. تم قياس التركيز الكمي باستخدام التقنيات الكهروكيميائية. في وقت لاحق ، تم التحقيق في تأثير إضافة NPs مختلفة إلى المحلول وتمت مقارنة النتائج بسبب إضافة NPs. من المتوقع أن يتم إخماد ذروة التيار الكهروكيميائي للمادة الكيميائية عند إضافة NPs. في البداية ، تم تطبيق قياس الجهد الدوري (CV) تحت الدراسة بدون NPs ، وتكررت العملية بعد إضافة NP لمسح التيار الكهروكيميائي. كان من المتوقع أن تنخفض الإشارة الحالية بسبب التفاعل الكيميائي مع NPs. خلال هذا التحقيق ، تم اختيار حمض الميفيناميك (MFA) والديكلوفيناك (DCF) كأدوية نموذجية. بالنسبة للتحليل ، تمت مراقبة وتحسين المتغيرات المختلفة مثل الوقت الكيميائي ودرجة الحموضة ونوع NP.



## Chapter One: Theory and Introduction

---

This chapter serves as an overview of wastewater treatment using various techniques including traditional and electrochemical methods. Throughout the process of treating wastewater, an electrochemical cell with a three electrode system was used. In addition, this chapter concentrates on two main pharmaceuticals MFA and DCF which played a significant role in contaminating water. Lastly, different types of NPs have been discussed to test their efficiency in the drug removal from water.

There is a dramatic increase in pharmaceuticals in water due to the continuous increase in population. This has contributed to a raise in industrial activities, and contamination of air, soils and aquatic ecosystem. The traditional methods commonly used for detecting pharmaceuticals and quantifying pollutants' removal include; flame atomic absorption spectrometry (FAAS), gas/liquid chromatography-mass spectrometry, inductively coupled plasma atomic emission spectroscopy (ICP-AES), inductively coupled plasma mass spectrometry (ICP-MS), high performance liquid chromatography (HPLC)–ultraviolet (UV) and fluorescence (FL) detection, and quantitative polymerase chain reaction. Although these analytical methods can achieve the desired results, they require complicated instruments which are costly, high level of expertise, and time consuming (Jin and Maduraiveeran 2017).

Electrochemical techniques (ETs) are utilized for electrical measurements. ETs have been widely recognized recently for their high sensitivity, high speed analysis, simple sample preparation, and relative low operating costs. These techniques have contributed to a large area of research and development in chemistry health, biology, medicine, and environmental aspects (Panina 2011). Visually, the resulting current due to variation in the electrode potential is measured during a process of interest as a result of reduction or an oxidation on the surface of the electrode.

ETs include several techniques such as CV, linear sweep voltammetry (LSV), square wave voltammetry and stripping voltammetry (SWV) (Farghaly, Abdel Hameed, and Abu-Nawwas 2014). Previously, ETs have been used in many applications especially

in biological samples and for drug analysis. These techniques have the capacity to determine trace chemical species and pharmaceuticals' concentrations in different samples (Widrig et al. 1990). The three electrode cell used in ETs consists of a reference electrode, counter electrode, and working electrode. Glassy carbon electrode has been involved in many researches as a working electrode due to its high electrochemical and thermal stability (S. Sharma 2018).

### *1.1 Water Pollution*

Water pollution is a serious environmental problem that is caused either by natural sources (organic matter, soil erosion) or by human activities such as industrial, agricultural and domestic actions. The most frequently detected classes of pharmaceuticals are non-steroidal anti-inflammatory drugs (NSAIDs), such as DCF, ketoprofen, and mefenamic acid (MFA) (Szymonik, Lach, and Malińska 2017).

In addition, water pollution is considered among the most challenging environmental problems. Water pollution has increased by a new group known as emerging contaminants such as pharmaceuticals, pesticides, industrial chemicals, surfactants, and personal care products (Colombo et al. 2016). The presence of MFA in sewage waters has increased and its concentration exceeded the safe limit of 0.43 µg/L (Werner, McNeill, and Arnold 2005) In Palestine, 60% of the houses are connected to

sewage systems and the wastewater is discharged into valleys. Furthermore, only 1% of the collected water are properly treated (Prakash Rao and Michael Muller 2007). Pharmaceuticals are a diverse group and for that, DCF was also investigated since it exceeded the safe limit in previous studies around Al-Bireh plant and was measured to be 1500 ng/L in the influent stream (Wasser and Str 2013).

As a result, a number of techniques were developed to remove wastewater from pharmaceuticals. Removal process can range from single unit process to full-scale wastewater treatment which can be costly especially in developing countries like Palestine.

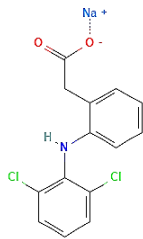
Many processes were applied to remove contaminants from wastewater, such as the oxidative degradation by ozone,  $O_3/H_2O_2$ , photo-Fenton, and the use of UV light with hydrogen peroxide which can provide good elimination of odor and color as well (Crini and Lichtfouse 2019). These techniques are characterized by the high operational costs and the slow removal kinetics. Thus, the use of nanoparticles was investigated in the removal of contaminants from water due to their high removal efficiency (Al-Rifai, Gabelish, and Schäfer 2007).

Other physical and chemical treatment processes have been reported in the past three decades including precipitation for its high efficiency in eliminating metals and fluorides, solvent extraction for large scale operations in water cycling, membrane filtration since solid waste generation is low and chemicals are not required in the process, adsorption/filtration for its wide variety of target contaminants, and coagulation process due to its simplicity and the chemical availability commercially (Crini and Lichtfouse 2019).

### *1.2 Diclofenac Sodium*

Diclofenac (DCF) is a phenyl-acetic acid derivative drug which belongs to the NSAID with analgesic anti-pyretic properties which has specific physical and chemical properties as presented in Table 1 (Swain, Nagamani, and Panda 2015). This drug is part of many prescriptions for the long term treatment of osteoarthritis (Panda et al. 2013), Parkinson (Swain, Nagamani, and Panda 2015), rheumatoid arthritis (Yilmaz et al. 2015), and ankylosing spondylitis (Patil, Naik, and Nandibewoor 2009). The sodium salt form of DCF works by reducing substances in the body that causes pain and inflammation. On the other hand, DCF has few side effects including vomiting, headache, dizziness, and nausea (Haichi Yu et al. 2021).

Table 1: Physical, chemical properties of DCF.

Item	DCF	Reference
Structure		(Biotechnology 2022a)
Formula	C <sub>14</sub> H <sub>10</sub> Cl <sub>2</sub> NNaO <sub>2</sub>	(Biotechnology 2022a)
IUPAC Name	sodium;2-[2-(2,6-dichloroanilino)phenyl]acetate	(Biotechnology 2022a)
Molecular weight	318.14 (g/mol)	(Biotechnology 2022a)
PKa	4.0	(Adeyeye and Li 1990)
Solubility mg/ml	1.36	(Kincl et al. 2004)
Melting Point	285-289 °C	(Petar TUDJA 2001)

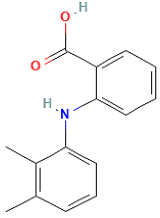
The focus to investigate DCF was mainly coming from the persistent toxic waste especially from the poor treatability drugs. Due to its extensive use, DCF has been found in wastewater treatment plant effluents with concentrations up to 10 µg/L, in surface (up to 15 µg/L) and groundwater (up to 0.15 µg/L), and in drinking water with quantities in the low ng/L range (Heim et al. 2020). The toxicity increases when combined with other medications found in the water. Because of the documented risk to the aquatic environment, the European Union (EU) classified DCF as an emerging pollutant and placed it on the first watch-list for monitoring (Heim et al. 2020). There are negative consequences in some species even at extremely low doses. The lowest measured effect concentration for cytopathology in rainbow trout livers, kidneys, and

gills was 1  $\mu\text{g/L}$  (Hui Yu et al. 2013). Recently, a study was done which revealed that relevant concentrations of DCF led to impairment of the general health of fishes and destroyed their renal and gills, at the lowest observed concentration of 5  $\mu\text{g/L}$  (Takamoto et al. 2004).

### 1.3 Mefenamic Acid

Many pharmaceuticals have been detected in aquatic systems at  $\text{ng.L}^{-1}$  or  $\text{pg. L}^{-1}$  which might come from production sites or direct disposal. Pharmaceuticals' toxicity and accumulation in living organisms can lead to serious environmental problems even at trace concentrations since they resist any biological degradation processes (Feier et al. 2018). In Table 2 different physical and chemical properties are determined in order to explain the behavior of MFA under various conditions.

**Table 2: Physical, chemical properties of MFA.**

Item	MFA	Reference
<b>Structure</b>		(Biotechnology 2022b)
<b>Formula</b>	$\text{C}_{15}\text{H}_{15}\text{C}_{12}\text{NO}_2$	(Biotechnology 2022b)
<b>IUPAC Name</b>	N-(2,3-dimethylphenyl)-2-aminobenzoic acid	(Biotechnology 2022b)
<b>Molecular weight</b>	241.28 (g/mol)	(Biotechnology 2022b)
<b>PKa</b>	4.5	(Biotechnology 2022b)
<b>Melting Point</b>	398.8 $^{\circ}\text{C}$	(Biotechnology 2022b)
<b>Solubility mg/ml</b>	0.2 mg/ml	(Kedarnath. 2011)

MFA, scientifically named 2- (2, 3-dimethylphenyl) amino benzoic acid, plays a huge role by reducing mild to moderate pain (Bukkitgar et al. 2019). On the bright side, it's usually used in treating different cases including musculoskeletal illness, osteoarthritis, and sports injuries (Bukkitgar et al. 2018). Unfortunately, if its concentration increases in water and sewage plants, it will have toxic effects especially with having high stability in the environmental mediums (Dolatabadi, Ahmadzadeh, and Ghaneian 2020). In addition, overdoses of MFA leads to toxic metabolite accumulation which turns to acute hepatic necrosis (Niazi, D.Torkman, and Khorshidi 2015).

Various advanced treatment techniques like membranes, adsorption, and photodegradation have been used in the past and were found to be ineffective at removing MFA from wastewater. As a result, more specialized advanced approaches are still required (M. Al-Jabari et al. 2018).

Such contamination is found in both surface water and wastewater and due to this result, different types of adsorbents have been considered in treating water from pharmaceuticals that cause resistance in natural bacteria populations (M. Al-Jabari et al. 2018).



### 1.4 Electrolysis of Water

Water electrolysis is the process of utilizing electricity to breakdown water into oxygen and hydrogen gas. This hydrogen gas can be used as hydrogen fuel, or it can be combined with oxygen to make oxyhydrogen gas, which is used in welding and other purposes (Carmo et al. 2013).

Electrolysis, also known as water splitting, occurs at a minimum potential difference of 1.23 volts between oxidation and reduction half-cell potentials, however at that voltage, external heat from the environment is necessary (Sataloff, Johns, and Kost 2006).

**Oxidation at anode:**  $2 \text{H}_2\text{O} (l) \rightarrow \text{O}_2(g) + 4 \text{H}^+(aq) + 4e^-$ ,  $E^\circ = 1.23 \text{ V vs. NHE}$

A reduction process occurs for pure water at the negatively charged cathode, with electrons (e) from the cathode being delivered.

**Cathode (reduction):**  $4\text{H}^+ (aq) + 4e^- \rightarrow 2\text{H}_2 (g)$ ,  $E^\circ = 0.00 \text{ V vs. NHE}$

**Overall reaction:**  $2 \text{H}_2\text{O}(l) \rightarrow 2 \text{H}_2(g) + \text{O}_2(g)$ ,  $E^\circ_{\text{cell}} = -1.23 \text{ V}$ ;  $\Delta G^\circ = 475$

**kJ/mol**

To combine half reactions, they must be either acid or base balanced.

At 25 °C and pH 0, ( $[\text{H}^+] = 1.0 \text{ M}$ ), the standard potential of the water electrolysis cell ( $E_{\text{cell}} = E_{\text{cathode}} - E_{\text{anode}}$ ) is -1.229 V (Sataloff, Johns, and Kost 2006).

### *1.5 Nanoparticles*

Nanotechnology is a new field of research that focuses on excising the structure of matter between 1 and 100 nanometers in the atomic, molecular, and super molecular levels in order to generate desired qualities and functionalities for a variety of applications (Koul et al. 2021). Nano-materials have unique features that make them ideal for a variety of applications, including mobility, food safety, catalysis, renewable energy, and healthcare (Kumari, Dhand, and Padma 2021).

Recently, tremendous amounts of attention have been witnessed in the nanomaterial-based electrochemical signal. Furthermore, nano-materials can add many properties to the ETs among conductivity, biocompatibility, and synergic effect leading to highly sensitive techniques (Zhu et al. 2015). Owing to nano-scale dimensions, NPs have proven to enhance sensitivity and selectivity. Moreover, they provide high surface area to volume ratio to drive electrode kinetics (Jin and Maduraiveeran 2017). Recently, sensors have been integrated with nano-materials. In addition, ETs can also measure an electrical signal which provides information about the concentration of the analyte and can also be used for the removal of pollutants in water since they have high sensitivity for low concentrations.

Recently, iron oxide nanoparticles (IO-NPs) have gained much attention due to their properties including super paramagnetism, great surface area (Zia, Phull, and Ali 2016), nontoxicity, and biodegradability (Cotin et al. 2018). Over the few past decades, IO-NPs have been used in research because of their high reactivity due to the variety in oxidation forms ( $\text{FeO} \leftrightarrow \text{Fe}_3\text{O}_4 \leftrightarrow \gamma\text{-Fe}_2\text{O}_3 \leftrightarrow \alpha\text{-Fe}_2\text{O}_3 \leftrightarrow \text{FeOOH}$ )

(Genuzio et al. 2016) (M. H. Al-Jabari et al. 2019). These nanoparticles have been used in variable therapeutic applications (Dadfar et al. 2019), agricultural and environment (Ali et al. 2016), catalysis (Ahmad, Phul, and Khan 2019), and magnetic resonance imaging (MRI) (Ahmad, Phul, and Khan 2019). An external magnetic field can be used for separating NPs as a response to their paramagnetic behavior. This separation can be used in order to avoid filtration problems such as filtration and membrane fouling in packed columns (Niazi, D.Torkman, and Khorshidi 2015).

Another type of iron based nanoparticles that played a huge role in waste water remediation and reducing human risks are zero valent iron nanoparticles (nZVI ). (Aragaw, Bogale, and Aragaw 2021). Soil and water pollution arise due to the presence of toxic chemicals and for the following reasons: nZVI have been obtained and tested on a large number of pilot studies. nZVI have achieved amazing results in the remediation capacity of ground water (Galdames et al. 2020) and as a sorbent for numerous inorganic and organic contaminants in aqueous solutions (Trakal et al. 2019). These NPs have several properties that allow them migrate below ground which helps especially when the chemicals lie beneath buildings (Pramudita, Iskandar, and Indarto 2018). In addition, nZVI can reduce many solvent concentrations to nearly zero within days (Baalousha, Lead, and Ju-Nam 2011). On the other hand and despite of the advantages, they can form micro-scale aggregates due to the weak surface charges of iron which limits their use in situ remediation.

Due to the aggregation, many properties will be affected including mechanical strength and mobility (Pramudita, Iskandar, and Indarto 2018).

### *1.6 Electrochemical Techniques*

Electrochemical techniques (ETs) are used in many fields for analytical purposes. Generally, these techniques are used in testing pharmaceuticals activity through redox reactions which involve electron transfer between the electrode and the electrolyte at the electrode surface (Doménech-Carbó et al. 2015). ETs have gained a great interest in the developing countries where limited resources and limited affordability of costly other techniques such as spectroscopy and chromatography. Compared to other techniques, ETs are easier to be modified, cheaper, sensitive, able to recognize analyte components in many systems (biological, environmental, or neurological), and more importantly they can be portable to fields (Martínez-Huitle et al. 2015). The simplicity of automation, adaptability, moderate working conditions, high efficiency, and mobility of ETs for wastewater treatment are the most essential benefits (Martínez-Huitle et al. 2015).

This class of analytical techniques depends on scanning potential and measuring current of the analyte providing a low detection limit. The three main categories of ETs are: voltammetry techniques (VTs) (applying a potential and measuring the resulting current), coulometry (the current is measured over a period of time in a cell), and potentiometry (measures the potential between two electrodes) (Lasia 2013). The measurements depend on few aspects such as electrolyte solution,

cleanliness of the surface, the surface interactions, and the electrode material (S Mendoza et al. 2015).

### *1.6.1 Voltammetric Techniques*

It is very hard to give a complete explanation of VTs since it involves many branches in thermodynamics, kinetics of electrochemistry, and physical chemistry (Bard and Faulkner 2001). The term voltammetry is derived from voltamperometry which expresses a function of voltage. In general, if an electrode is placed in an electrolyte, it is possible to study the charge transfer between the electrode surface and the electrolyte solution (Scholz 2015).

### *1.6.2 Electrochemical Cell*

In voltammetry, the conduction and charge transport was monitored in the solution. In order to measure the current, an electrode (working electrode) is made smaller than the second one (auxiliary electrode) so that the current cannot be limited to the larger one. Figure 1 shows a schematic of a typical cell, which includes the working electrode (WE), which has the lowest electrode surface area, the reference electrode (RE), and the counter electrode (CE). Metal electrodes have gained a huge interest in the electrochemistry branch due to their high conductivity and ease of fabrication such as noble metals, gold, carbon materials, and platinum (Lakard, Pavel, and Lakard 2021). Glassy carbon electrode (GCE) was also been used as a working electrode based on its lower detection limit of pharmaceuticals due to the higher currents obtained for the oxidation peaks (Maria et al. 1997). In addition, it has

numerous advantages including its biocompatibility, not toxic, high sensitivity, and not getting affected by the oxidation and reduction processes leading to fouling (Lakard, Pavel, and Lakard 2021). Moreover, the production of chemisorption of oxygen on the carbonaceous electrode's surface with C = O groups is thought to be the cause of a carbonaceous electrode's pH sensitivity (Shigemitsu, Matsumoto, and Tsukahara 1979).

The electrochemical processes at the counter electrode are often unknown, and hence irrelevant to the measurement's conclusion.

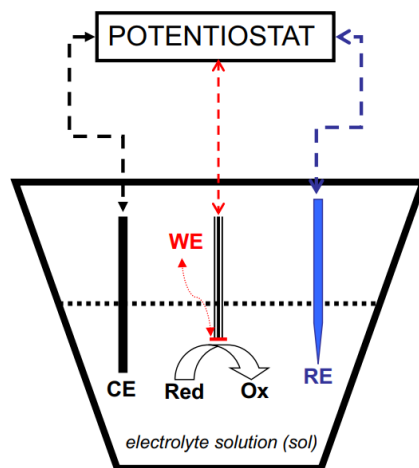


**Figure 1: A voltammetric cell scheme which shows the current flows between the small working electrode (WE) and the large counter electrode (CE). The potentiostat is used to adjust the potential of the working electrode in comparison to the constant potential of the robust reference electrode (RE).**

The reference electrode should be durable and have a consistent chemical composition, as this impacts its electrical potential. Its function is to act as a reference

point for controlling the relative potential of the working electrode using a potentiostat. The electrochemical reaction and the ensuing flow are propelled by the electrical potential difference between the solution and the working electrode (Mirceski, Skrzypek, and Stojanov 2018).

The potential of the electrolyte solution is identical to the potential of the metallic phase of the reference electrode in most potentiostats for 3-electrode measurements. The potential difference between the working electrode's metallic phase and the electrolyte solution is therefore equivalent to the potential difference between the working and reference electrodes. The potentiostat controls the voltage between the working and counter electrodes to achieve the correct potential difference between the working electrode and the electrolyte solution (Mirceski, Skrzypek, and Stojanov 2018).

### *1.6.3 Diffusion Layer*

The field of chemistry that examines the electron transport at an electrode is known as electrochemistry. The electroactive species must be transported from the bulk solution to the electrode vicinity for a redox reaction to occur.

When the potential of the working electrode is negative, a chemical species in solution get reduced by taking electrons at the interface between electrode and solution. Oxidation, on the other hand, happens when the working electrode's potential is positive enough that a species contributes an electron to the electrode. An electrochemical species must diffuse into the region of the electrode in order to be oxidized or reduced.

When a particle larger than one nanometer is dispersed in water, a reaction occurs at the solid-liquid interface because both the solid and liquid parts have different energy levels, resulting in tension at their interface once they come into close contact. Basically, all substances have a negative surface charge when dispersed in water. Because of the high dielectric constant of water, all substances have a negative surface charge when dispersed in it. On the other hand, media with a lower dielectric constant have an anionic surface charge. A well-ordered and immovable layer covers the surface of the particle like a skin, attracted by the surface charge. This layer is also known as the fixed layer or stern layer.

Cations neutralize the anionic surface charge, but because ions are often surrounded by water molecules, they are too large to completely neutralize the charge, leaving a residual anionic charge. This residual anionic charge attracts more ions from the surrounding water, starting to form a second layer around the particle.



A basic scheme for a metal electrode in contact with an electrolyte solution is shown in Figure 2. The inner Helmholtz plane (IHP) is the plane that passes across the centers of the particularly adsorbed species on the electrode surface. Since the ratios of cations and anions change in such a way that their charges compensate, the surplus charge decays toward the solution bulk in the diffuse layer. Within the compact layer and up to the outer Helmholtz plane, the potential varies linearly in the EDL. In the diffuse layer, it then decays exponentially. This is significant because there is no electric field emanating out from charged electrode outside the EDL, i.e., ions are not impacted by the electrode potential outside the EDL, and hence no migration can occur.

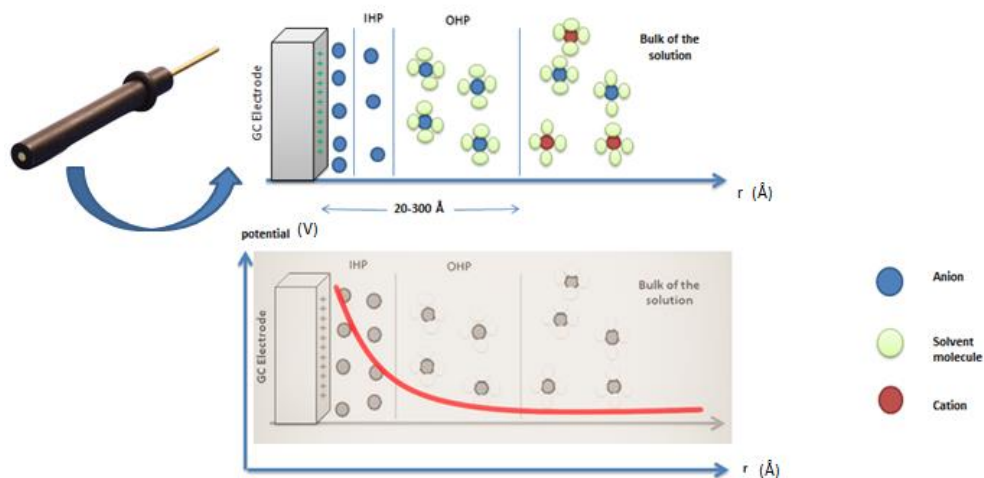


**Figure 2: Schematic of the electric double layer at the electrode|electrolyte interface at a negatively charged electrode**

When an electrode is put in solution, it may become positively or negatively charged due to a lack of or excess of electrons at the electrode surface. At a given distance

from the electrode's surface, species with opposing charges are drawn to it from the solution, which normally extends a few Angstroms (Å) into the solution depending on the ionic strength of the solution. The electrochemical double layer (EDL) is the overall arrangement of the charged interface, which gets more diffuse as distance from the electrode surface rises. The electrical double layer operates as a capacitor with two charged layers separated by a fixed distance due to charge separation at the electrode-solution interface.

#### *1.6.4 Cyclic Voltammetry*

The voltammograms can be observed over a wide potential range to observe the redox behavior. CV studies various redox reactions during the pharmaceutical analysis (Gupta et al. 2011) and is mainly used to determine the redox reactions and to understand the reaction intermediates. As it can be seen in Figure 3, CV depends on varying the applied potential at a working electrode in the forward reaction and swept back to initial voltage (Bard and Faulkner 2001).

The current detected in this method increases as scan rate and concentration increases according to Randles-Sevcik equation at 25 °C.

$$i_p = 2.686 \times 10^5 n^{3/2} A c^0 D^{1/2} \nu^{1/2} \dots\dots(1)$$

With A in cm<sup>2</sup>, D in cm<sup>2</sup> s<sup>-1</sup>, c in mol/cm<sup>3</sup> and ν in Vs<sup>-1</sup>, and the peak current in amperes.

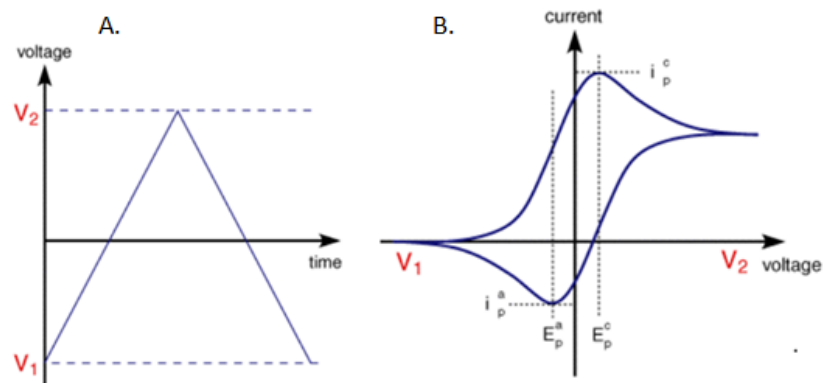


Figure 3: A) Typical potential variation and B) the shape of the I-E curve in the popular technique known as cyclic voltammetry where  $i_p^c$  and  $i_p^a$  are the cathodic and anodic peak current, and  $E_p^c$  and  $E_p^a$  are the cathodic and anodic peak potentials

Figure 3 is driven by the interfacial redox reaction (2) due to the basic thermodynamic properties (e.g., Gibbs free energy) and the mass transfer process referred as diffusion.



The term (sol) denotes dissolved species, while  $n$  denotes the stoichiometric number of electrons. Only at the working electrode|electrolyte contact does the redox reaction (2) take place. If the experiment continues with reversely directed potential sweeps, one may clearly predict that the electrode reaction (2) will drift to the opposite, left-hand side (reduction).

CV is the term for this type of voltammetric experiment. The first half of the cyclic voltammetry is clearly identical to Figure 4, whereas the second half uses the reverse potential sweep to drift the reaction in the other direction (reduction of  $\text{Ox}_{\text{sol}}$  to  $\text{Red}_{\text{sol}}$ ). The forward and reverse components of the related CV in Figure 4 show the oxidative and reductive changes of the electrode equilibrium, respectively. The oxidation (also known as anodic) and reduction (also known as cathodic) currents are given a positive and negative sign, respectively.

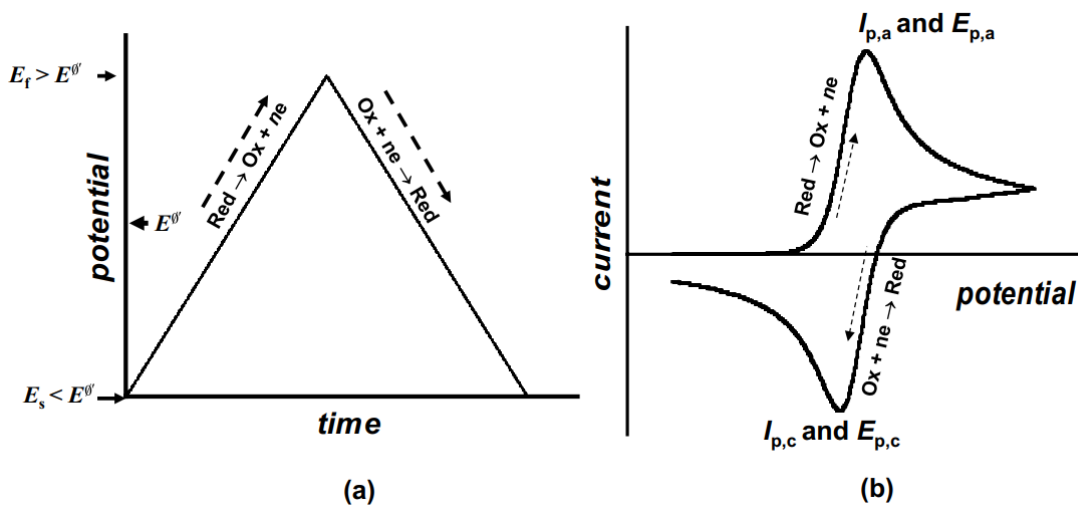


Figure 4: In the common technique known as cyclic voltammetry, (a) typical potential fluctuation by varying the electrode potential in the simplest linear fashion from certain starting ( $E_s$ ) to the final ( $E_f$ ) potential, and (b) the form of the I–E curve are shown. The latter is linked to the formal potential ( $E^{\theta'}$ ), which is a crucial thermodynamic parameter for the electrode process. The maximum of the asymmetric peak-shaped voltammogram, is defined by the peak-current ( $I_{p,a}$ ) and the peak-potential ( $E_{p,a}$ )

The most important points in CV are the peak current ( $i_p^c$ ,  $i_p^a$ ), peak potentials ( $E_p^c$ ,  $E_p^a$ ). From the peak potentials, it can be easily determined if the process is reversible or irreversible.

$$\Delta E_p^o = |E_p^a - E_p^c| = 2.303 \frac{RT}{nF} \dots\dots(3)$$

Where  $n$  is number of electrons,  $F$  = Faraday constant (96,485 C/equiv),  $R$  = 8.314 J/mol·K, and  $T$  is temperature at 25 °C.

If the difference between the anodic and cathodic peak potentials, known as peak-to-peak separation ( $E_p$ ), is 57 mV, and the width at half max on the forward scan of the peak is 59 mV, then it's considered reversible (Bard and Faulkner 2001). For a reversible reaction,  $\Delta E_p^o$  should be  $0.0592/n$  V. If the peak separation is  $> 0.0592/n$  V, it is considered to be irreversible (Sandra Mendoza et al. 2015).

### *1.6.5 Linear Sweep Voltammetry*

Linear sweep voltammetry (LSV) is performed at a fixed potential range and it is scanned from a lower to a higher voltage limit to obtain an oxidation peak as shown in Figure 5. Moreover, the current is plotted as a function of voltage. The sweep produced is similar to the forward scan in CV (Yan et al. 2017).

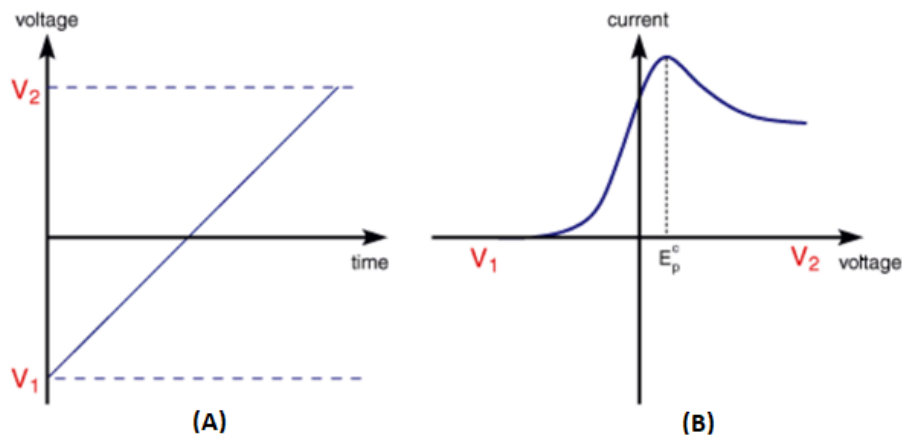


Figure 5: a) Typical potential fluctuation by varying the electrode potential in the simplest linear fashion from certain starting ( $V_1$ ) to the final ( $V_2$ ) potential b) Typical voltammogram created by changing the electrode potential in the simplest linear way from a specific beginning ( $V_1$ ) to a specific final ( $V_2$ ) potential.

The rate of potential variation with time (sweep rate, or scan rate,  $v$ ) is the technique's main parameter. The sweep rate is defined as a ratio of the potential interval  $\Delta E^0$  ( $\Delta E^0 = E_f - E_s$ , where  $E_f$  and  $E_s$  are the final and starting potentials, respectively) to the time interval  $\Delta t$  which is required to cross the potential route  $E$ , resulting in  $v = \Delta E^0 / \Delta t$ . The entire duration of the experiment, which might range from minutes to milliseconds, is clearly determined by  $v$  (Mirceski, Skrzypek, and Stojanov 2018).

### 1.6.6 Square Wave Voltammetry

Square wave voltammetry (SWV) is well known for providing symmetrical wave pulse amplitude  $E_{sw}$ . What make it special are; it's high sensitivity, high speed, and the subtraction of the background current. The signal is composed of a staircase waveform with a step height of  $\Delta E^0$  and the duration of each step is  $\tau$  where the scan

rate can be determined from these two important features (Razmi, Ezzati, and Khorablou 2019).

$$v = \Delta E^0 / \tau \dots\dots(4)$$

Where  $v$  is the scan rate,  $\Delta E^0$  is the step height in volts and  $\tau$  is the duration of each step in seconds.

As can be seen in Figure 6, the period of two pulses is the same, denoted by  $t_p = \frac{\tau}{2}$ , where  $\tau$  is the duration of the potential step, as previously described. Square-wave amplitude is the height of a single pulse ( $E_{sw}$ ). The SW frequency  $f = \frac{1}{2t_p}$  is frequently used to demonstrate the latter parameter. The latter is the essential time parameter of the SW voltammetric experiment, as we can see. The scan increment  $\Delta E$  of the staircase ramp, the SW amplitude ( $E_{sw}$ ), and the length of the potential pulse  $t_p$  are the primary parameters of the SW potential modulation. The SW potential waveform may be associated with scan rate defined as the product of the frequency and the scan increment,  $v = f \Delta E^0$

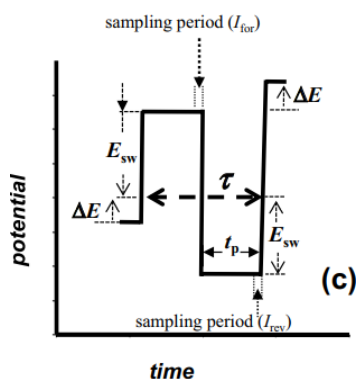


Figure 6: Single potential cycle in square-wave

SWV has higher sensitivity than CV since the voltammogram is achieved by replacing the continuous potential ramp with a staircase potential-time function. The current in this method is usually measured after each potential step. The forward current ( $I_{\text{for}}$ ) and reverse current ( $I_{\text{rev}}$ ) components of the SWV are made up of a sequence of current values measured at the end of each forward and reverse pulse. Furthermore, by subtracting the corresponding values of the forward and reverse current values as presented in Figure 7, a new voltammetric curve known as net current may be created. (Mirceski, Skrzypek, and Stojanov 2018).

$$I_{\text{net}} = I_{\text{for}} - I_{\text{rev}} \dots (5)$$

Where  $I_{\text{net}}$  is the net current, ( $I_{\text{for}}$ ) and ( $I_{\text{rev}}$ ) are the forward and reverse current of the SWV response respectively.

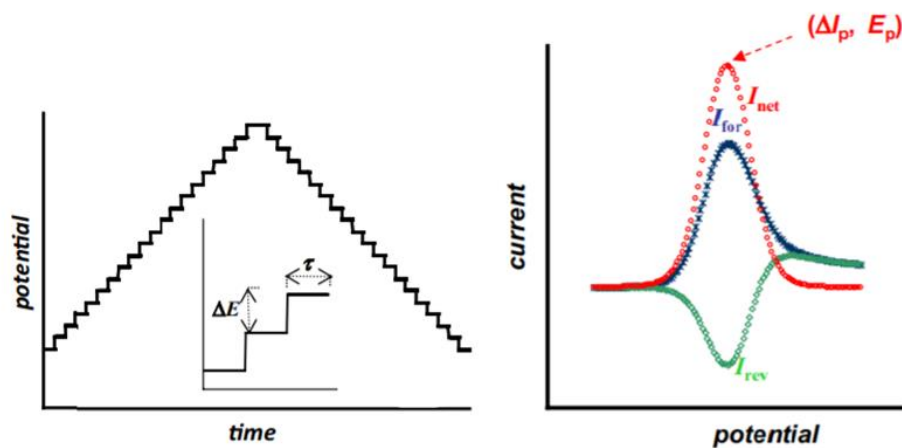


Figure 7: A potential waveform in SWV is shown. The duration of the potential step ( $\tau$ ) and the scan increment of the staircase potential ( $\Delta E^\circ$ ) are shown in the inset. A normal SWV is also shown compared to CV.



### *1.7 The Aim of This Study*

This research mainly focuses on detecting pharmaceuticals from aqueous samples using glassy carbon electrode due to its chemical stability, and good electrical conductivity. In addition, ETs are expected to provide results by detecting the desired chemicals in low concentrations.

This study aims to assess the removal of contaminants (DCF and MFA) from water samples using different ETs: CV, SWV, and LSV which were integrated by the use of IO-NPs and nZVI. The use of NPs is expected to remove pharmaceuticals from contaminated water since NPs are known for being highly profitable, and having high surface area in nature (Tambe Patil 2015).

Different parameters have been also considered in this research in order to investigate their effect on the pharmaceuticals' removal from wastewater such as pH, temperature, scan rate, types of NPs, and types of electrodes.

## Chapter Two: Experimental

---

A number of experimental laboratory studies were required in order to provide the data needed to remove pharmaceuticals from wastewater using NPs. Oxidation and reduction peaks were obtained in the laboratory in order to detect MFA and DCF in aqueous samples. Water samples were prepared and different parameters — pH, temperature, type of electrodes, and type of NPs — were adjusted in order to evaluate their effects on the removal process. Finally, the test methods, apparatus, and test results are discussed in this chapter.

## 2. Experimental

### 2.1 Materials

Iron(II) chloride tetrahydrate  $\geq 99.0\%$ , Iron(III) chloride 97%, ammonia solution abt. 29% extrapure, ACS, 97.0-102.0%  $\text{FeCl}_3 \cdot 6\text{H}_2\text{O}$ , sodium borohydride  $\geq 96\%$ , 2-[(2,3-Dimethylphenyl)amino]benzoic acid (MFA), potassium chloride  $\geq 99\%$ , diclofenac sodium, sodium dihydrogen phosphate dihydrate, di-Sodium hydrogen phosphate heptahydrate, ferric chloride hexahydrate  $\text{FeCl}_3 \cdot 6\text{H}_2\text{O}$ , 0.47M  $\text{NaBH}_4$ , Absolute ethanol, absolute methanol. The aqueous solutions were prepared using Milli-Q water with a resistivity of 18.2  $\text{M}\Omega \cdot \text{cm}$ . All chemicals were purchased from Sigma-Aldrich Chemical Company (Milwaukee, U.S.A)

### 2.2 Samples' preparations

A stock solution of 40 mg/L MFA was prepared by dissolving 0.0040g MFA in a buffer solution ( $\text{Na}_2\text{HPO}_4 \cdot 7\text{H}_2\text{O}$ ,  $\text{NaH}_2\text{PO}_4 \cdot 2\text{H}_2\text{O}$ , KCl solution) in a 100 ml volumetric flask. Minimum amount of methanol were added to dissolve MFA solution with slight heating when needed to ensure its solubility. Standard solutions of MFA were prepared using serial dilutions with the same buffer solution to attain 30, 20, 10, 5, 0.5, and 0.3 mg/L MFA solution.

Similarly, stock solution of 40 mg/L DCF was prepared by dissolving 0.0040 g in a 100 ml buffer solution which was adjusted to pH 7.02 value using sodium hydroxide. Standard solutions of DCF were prepared by applying serial dilutions with the same buffer to attain 30, 20, 10, 5, and 2.5 mg/L DCF solution.

### *2.3 Synthesis of Iron (IV) Oxide and Zero Valent Iron Nanoparticles*

Iron oxide nanoparticles were synthesized under a basic medium by dissolving  $\text{Fe}^{+2}$  and  $\text{Fe}^{+3}$ . In this process, 10 ml of deionized water was added with a 12.5 ml of 29% ammonia solution in a two necked bottom flask. The set up was put in silicon oil and the system was kept under 60 °C as can be seen in Figure 8. Ferrous ( $\text{FeCl}_2 \cdot 4\text{H}_2\text{O}$ ) and ferric chloride ( $\text{FeCl}_3 \cdot 6\text{H}_2\text{O}$ ) at 1:2 molar ratio was added to the solution precisely 2.65 and 5.30 g, respectively. The reason of these impurities is deviation of  $\text{Fe}^{+2}/\text{Fe}^{+3}$  ratios from the mentioned value. Existence of oxygen in the reaction media leads to this deviation which oxidizes  $\text{Fe}^{+2}$  ions to  $\text{Fe}^{+3}$ . The reaction mixture was stirred for 2 hours on a hot plate. After adding ammonia, the solution color went from orange to black indicating that magnetite IO-NPs were prepared.

IO-NPs were collected using suction filtration followed by washing NPs with Milli-Q water to maintain a pH 7 followed by washing the NPs using absolute ethanol to remove unreacted species.

After being filtered, NPs were stored for 24 h in a desiccator till next day for experimental use (Iriarte-Mesa et al. 2020).



Experimental investigation shows that passing nitrogen gas through the reactant solution has two advantages: 1- preventing existence of oxygen in the reaction medium 2- leading to smaller sizes of nanoparticles.

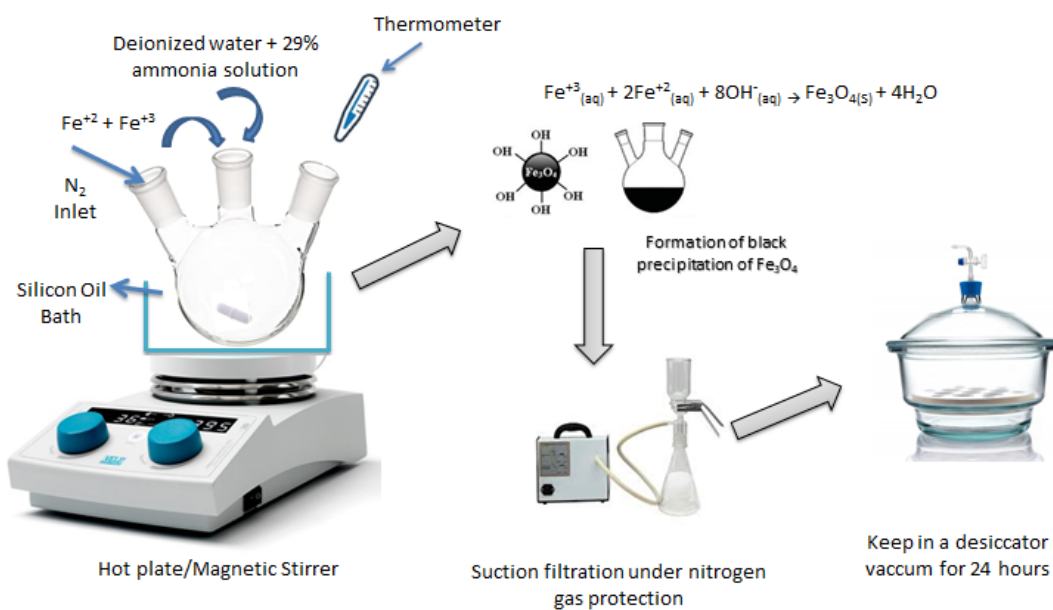


**Figure 8: Synthesis of iron (IV) oxide nanoparticles which starts by mixing ferrous chloride and ferric chloride in a three-neck volumetric round flask and followed by adding ammonia. The mixture was kept at around 60 °C with a continuous mixing for two hours. NPs were collected after using suction filtration and were kept overnight in a desiccator.**

On the other hand, nZVI were prepared by adding 4.84 g of ferric chloride hexahydrate in a solution of de-oxygenated Milli-Q water into a 500 ml three-neck volumetric flask and absolute ethanol with a volume ratio of 1:4. A 0.47M of the reducing agent NaBH<sub>4</sub> was added after dissolving the ferric chloride with a rate of 1-2 drops per second using a dropping funnel as it can be seen in Figure 9. The nanoparticles' solution was reduced from Fe<sup>+3</sup> to Fe<sup>0</sup> after consuming all the reducing agent quantity.

The following chemical process was used to make nZVI with ferric chloride precursor solution as an iron source and sodium borohydride as a strong reductant as can be seen in equation (6).



The mixture kept under nitrogen for 20 minutes and nanoparticles were collected. Later on, NPs were washed using absolute ethanol three times in order to avoid oxidation of the produced NPs and were dried using suction filtration (S. M. Sulaiman and Al-Jabari 2021). The NPs were transferred to a desiccator in an inert atmosphere and were kept overnight until next day (Eljamal et al. 2018).

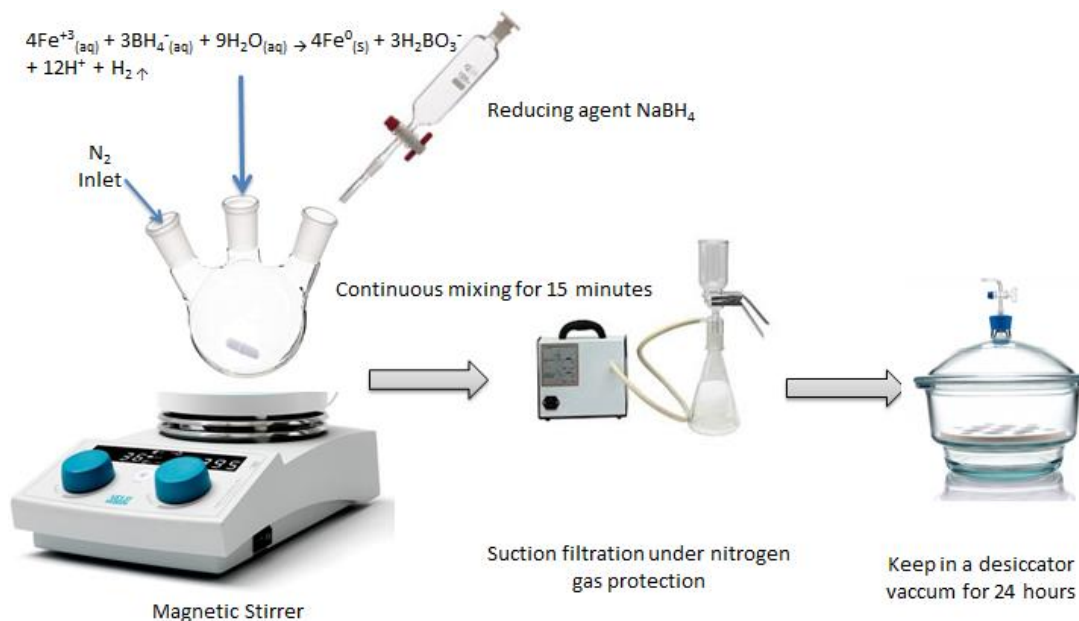


Figure 9: Synthesis of nZVI which starts by mixing ferric chloride hexahydrate in a solution of de-oxygenated Milli-Q water and absolute ethanol with a volume ratio of 1:4 in a three-neck volumetric round flask and followed by adding the reducing agent after dissolving ferric chloride. NPs were collected after using suction filtration and were kept overnight in a desiccator.

#### 2.4 Working procedure

50 ml volumetric flask was used to prepare MFA solution. Proper amounts of MFA solution was transferred to the cell which is manufactured to carry the electrodes at which the redox reactions occur. Meanwhile, the surface of the glassy carbon electrode was cleaned using alpha alumina powder 0.3 micron and CVs of the samples were recorded over a potential range for detecting MFA. Similar procedure was also applied for DCF. CVs were recorded to detect DCF drug redox reactions. In addition, Square wave voltammetry was also performed over a potential range to show the reduction peak.

### *2.5 Apparatus and Software/instrumentation*

A CHI760 Workstation is a multi-channel potentiostat applicable for cyclic voltammetry, linear sweep voltammetry, chronoamperometry, impedance spectroscopy, charge discharge characteristics, and other approaches for studying reaction kinetics, sensing materials, corrosion, and energy conversion. A three-electrode system consisted of an Ag/AgCl (sat. KCl), platinum auxiliary electrode, and a GCE as a working electrode was used for the pharmaceuticals detection over a specific potential range for each drug as shown in Figure 10.

pH of the buffer solution was determined using a Metrohm-750 desktop pH-meter. Meanwhile, fourier transform infrared (FT-IR) spectra were recorded for DCF, MFA, nZVI, IO-NPs, and NPs after the drug adsorption. Each sample was recorded in KBr pellets in the frequency range of 400–4000  $\text{cm}^{-1}$  using Bruker TENSOR II spectrometer.



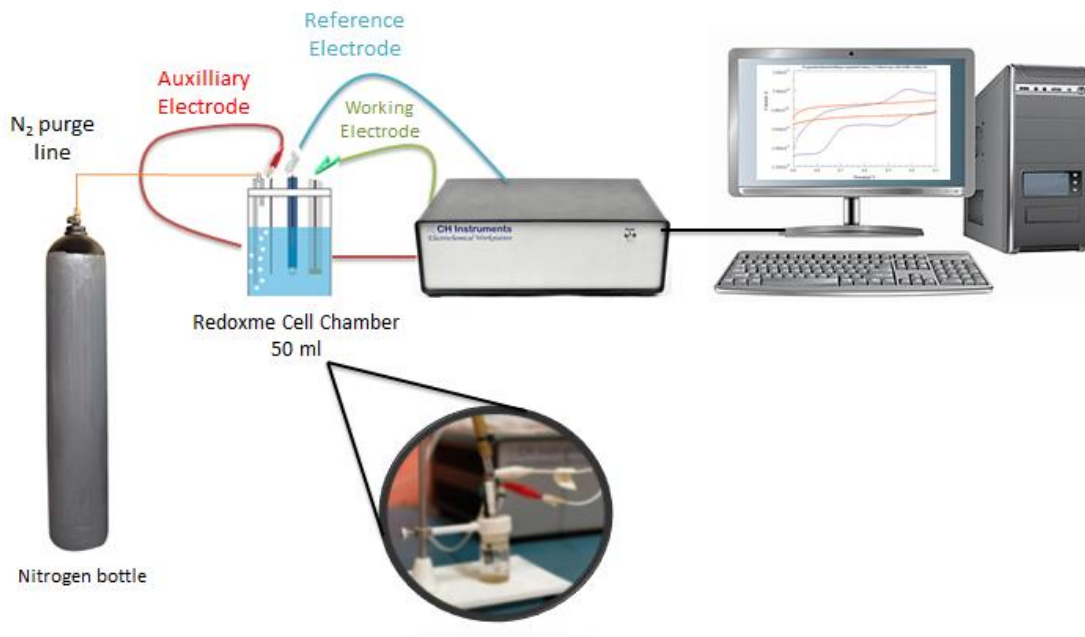


Figure 10: A representation image of electrochemical instrumentation setup

## 2.6 Analytical method

MFA has exceeded the safe limit concentration in sewage water worldwide which is  $0.45\mu\text{g/L}$  (Colombo et al. 2016). For that matter, MFA was obtained and aqueous samples with known concentrations were used as standards. Potassium chloride (KCl) was used without any further purification and all solutions were prepared in Milli-Q water. Electrochemical measurements were carried out in a conventional three-electrode cell; a reference electrode (Ag/AgCl), a platinum wire was used as a counter electrode, and a glassy carbon which was used as a working electrode.

Initially, cyclic voltammetry was applied followed by optimizing the conditions in order to study their effects on the electrochemical behavior. The current was measured using glassy carbon electrode and current peak was obtained. Afterward, NPs were added to the solution to work as adsorbents and the sample was scanned as well to obtain another CV under same conditions for samples without NPs.

Water was used as a solvent since the main aim is to solve a problem in the wastewater and to avoid complexation issue between the analyte and the solvent.

## Chapter Three: Results and Discussion

---

Data was presented into more comprehensive forms such as CV, SWV and LSV graphs. Along with presenting data, results were depicted in the form of calibration curves, tables, and other suitable forms. Analysis-comparison, trend lines were also provided. In addition, data was discussed and a brief conclusion was included.

### 3. Results and Discussion

#### 3.1 Conditions Optimization

##### 3.1.1 Type of electrode

Essentially, the electrochemical behavior of 40 mg/L DCF was investigated using two types of electrodes in a pH =10.06 phosphate buffer solution. The first working electrode was glassy carbon electrode which showed a promising potential to detect lower concentrations unlike the gold electrode.

In both electrodes, a CV scan was swept from 0.4 to 1.0 V and then was swept back in the same potential range as presented in Figure 11. The current started to increase until it reached a maximum value at around 0.7 V and then it started to decrease. In addition, the peak shape was sharper as GCE was used and wider by using gold working electrode indicating a faster oxidation by using GCE.

Initially gold working electrode was used according to its ability to detect the oxidized MFA. Although there was no shift in the peak potential when GCE was used, the peak current was higher than gold working electrode and as a result, GCE has been used for detecting MFA and DCF.

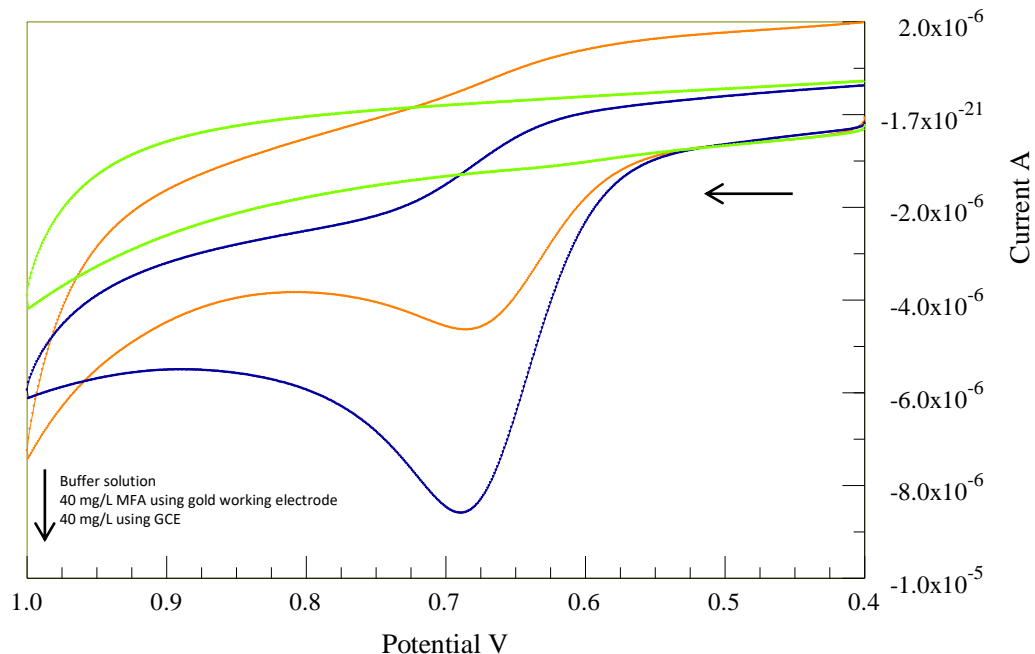


**Figure 11:** CV response for removing 40 mg/L MFA using glassy carbon electrode (blue CV) and gold working electrode (orange CV) after adding 0.08 g of IO-NPs in the aqueous solution at pH 10.06 in 0.1 M KCl using GCE, surface area (0.069 cm<sup>2</sup>), 300 mV/s

### 3.1.2 Effect of NPs Amount

Amount of NPs used is an important factor in any removal process. The large surface area of NPs can indicate the amount of the desired drugs that can be adsorbed on their surface (Beiraghi et al. 2014). A comparison of CV was recorded for oxidation of MFA after placing different amounts of NPs to discuss their affect. In previous studies, it was recorded that 0.25 g of IO-NPs was capable of removing DCF at different concentrations with high removal efficiency (S. M. Sulaiman and Al-Jabari 2021). On the basis of the previous study, similar amounts were added to a 40 mg/L

MFA solution to obtain a comparison with different adsorbent dose which were 0.04 g, 0.08 g, and 0.12 g.

A CV was performed for each dose to see the change in current peak as shown in Figure 12. As can be seen, the larger the dose the higher the adsorption of MFA on the NPs surface and the less amount dissolved in solution. Unfortunately, the larger the adsorbent's amount, the slower the adsorption which is due to agglomeration which reduces the surface area of NPs. Particle aggregation is a fundamental mechanism that reduces the surface free energy of the particles by increasing their size and lowering their surface area. The adherence of particles to one another by weak forces causes the aggregation of nanoparticles, resulting in (sub)micron-sized entities.

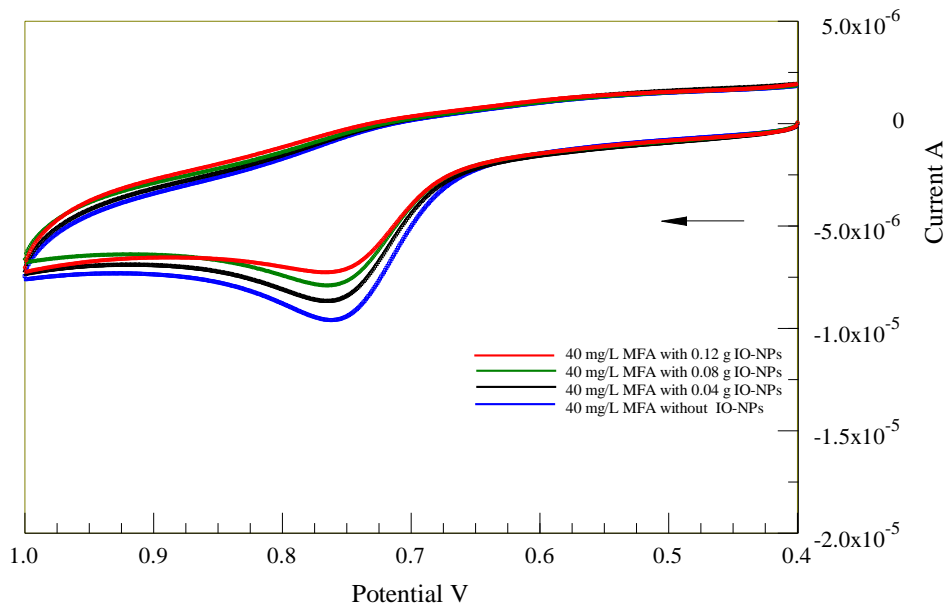


Figure 12: CV response of the IO-NPs amount effect ranging from 0.04 to 0.12 g on the peak current of 40 mg/L MFA using GCE at pH 7.02 in 0.1 M KCl using GCE, surface area (0.069 cm<sup>2</sup>), 300 mV/s

### 3.1.3 Effect of time

#### 3.1.3.1 Effect of time on DCF

The removal efficiency of DCF using the two types of adsorbents nanoparticles was studied. The results shown in Figure 13 indicate that nZVI has the ability to remove the reduced form of DCF almost completely at a potential around 0.45 V since the cathodic peak has disappeared. In addition, both oxidation peaks decreased up to a certain point which means DCF the current decreased due to the pharmaceuticals' adsorption on the NPs surface.

The reduction peak of DCF obtained in pH 7.02 at GCE and the peak current of DCF was lowered after adding 0.08 g of nZVI. Figure 13 shows the uptakes of the DCF as a function of contact time.

The adsorption effectiveness of DCF rose from 47.92 % to 60.67 %, when the contact duration was increased from 2 to 8 minutes as can be seen in Table 3. As a result, the best contact duration was determined to be 8 minutes, which may be employed in future research.

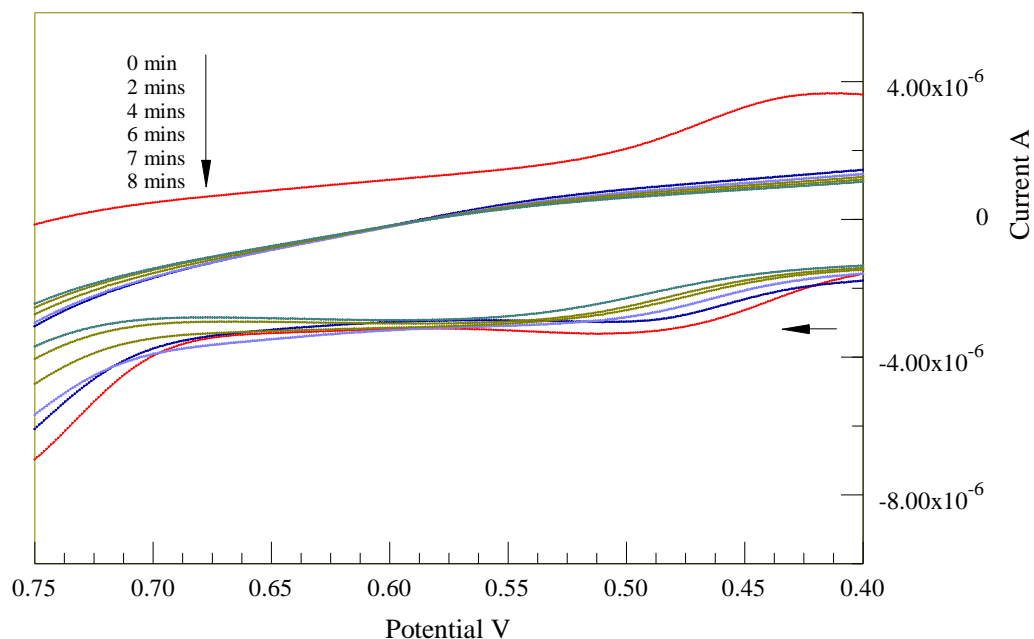


**Figure 13:** CV response for removing 40 mg/L DCF after adding 0.08 g of ZVNP at pH 7.02 in 0.1 M KCl using GCE, surface area (0.069 cm<sup>2</sup>), 300 mV/s.

The analyte DCF's electrochemical response was studied by SWV technique using GCE which is represented in Figure 14. The presence of N-H group in the DCF structure was primarily responsible for the rapid and high adsorption of DCF which



can be observed in Figure 13 by forming Hydrogen bonding with either  $\text{-OH}$  group under basic media or with  $\text{H}^+$  on the NPs surface from water. In addition, removal percentage was calculated for 40 mg/L and found to be 50% after nZVI addition to the water sample.

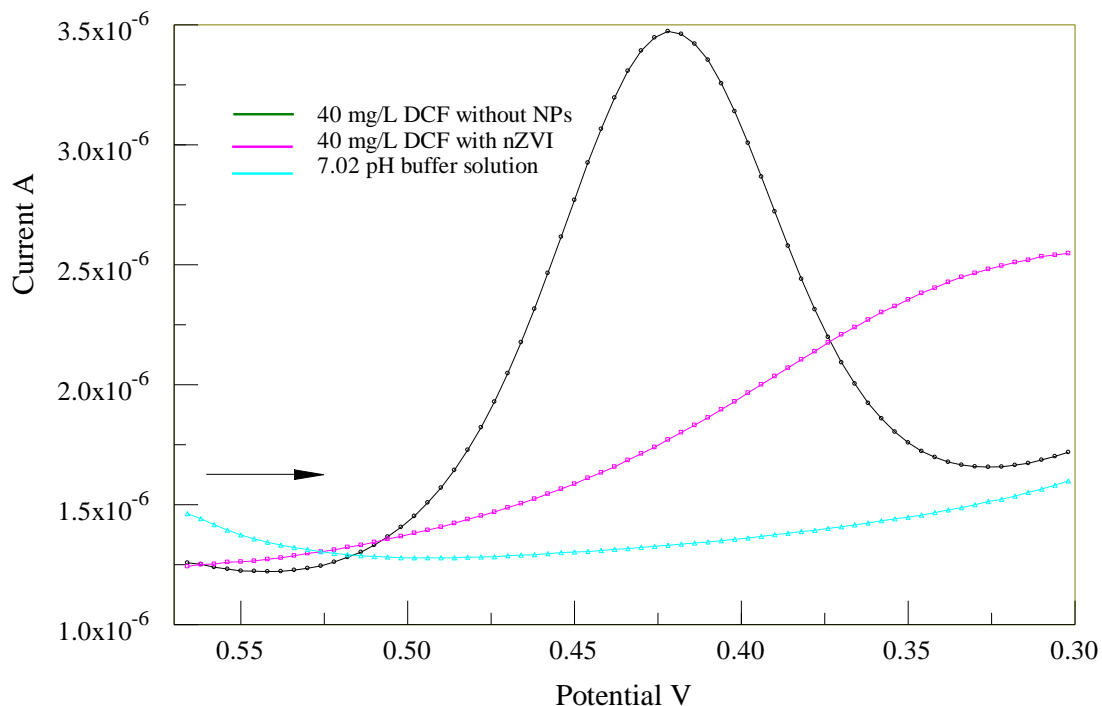


**Figure 14:** SWV for 40 mg/L DCF with and without nZVI in 0.1M KCl at GC electrode, in a pH solution of 7.02. SW amplitude, 25.0 mV; SW step, 4.0 mV; SW frequency, 15.0 Hz.

As a result, NPs were able to adsorb a large amount of DCF in a very short time (8 minutes). This rapid adsorption equilibrium is beneficial for water treatment systems.

From Table 3, the adsorption effectiveness of DCF on IO-NPs rose from 12.10 % to 36.31 %, when the contact duration was increased from 2 to 8 minutes. The results

show that the current becomes almost fixed as the time increases proposing that DCF concentration have reached a fixed concentration at the NPs' surface.

**Table 3: Time profile of DCF removal using 0.08 g of nZVI and IO-NPs**

Time (Minutes)	Time profile of 20 mg/L DCF removal using nZVI at 0.45 V potential			Time profile of 20 mg/L DCF removal using IO-NPs at 0.45 V potential		
	Current detected without NPs ( $\mu\text{A}$ )	Current detected with NPs ( $\mu\text{A}$ )	Removal percentage (%)	Current detected without NPs ( $\mu\text{A}$ )	Current detected with NPs ( $\mu\text{A}$ )	Removal percentage (%)
0	3.39	3.39	0.00	3.67	3.67	0.00
2	3.39	1.76	47.92	3.67	3.23	12.10
4	3.39	1.61	52.49	3.67	3.07	16.24
6	3.39	1.51	55.31	3.67	2.84	22.60
7	3.39	1.43	57.79	3.67	2.61	28.99
8	3.39	1.33	60.67	3.67	2.34	36.31

Figure 15 indicates clearly that the most significant performance was obtained when the adsorption is established at around 8 minutes. Removal percentage was close as

the time increased indicating that the adsorption has reached the maximum value at around 8 minutes which reached up to a value of 60%. From the removal percentage evaluated for both types of NPs, it is seen that nZVI were able to accomplish higher removal percentage.

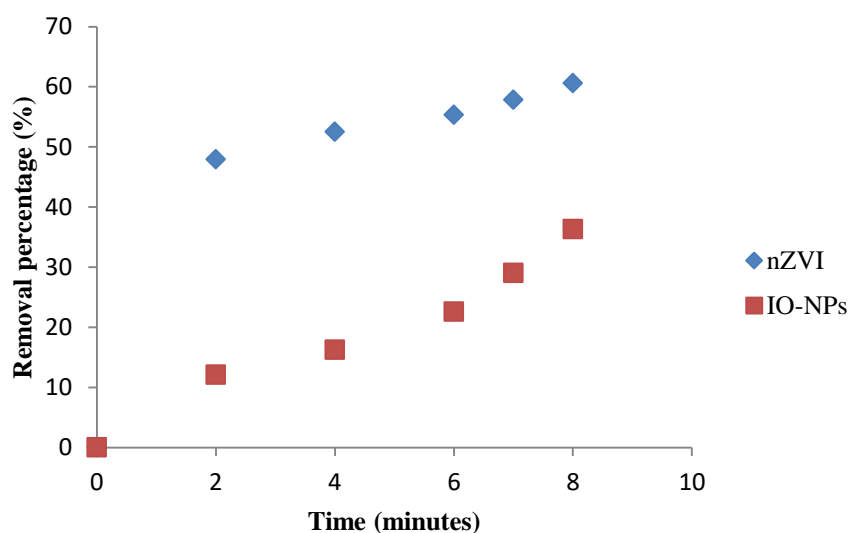


Figure 15: Time profile of 20 mg/L DCF removal percentage at 0.45 V

Meanwhile, the current in the peaks have decreased in Figure 16 using IO-NPs. Removal efficiency on 20 mg/L DCF at room temperature was evaluated using IO-NPs. The samples were analyzed at different time intervals (0, 2, 4, 6, 7, and 8 min).

As time increases, the larger the drug's amount adsorbed on the surface without desorption occurring on the surface

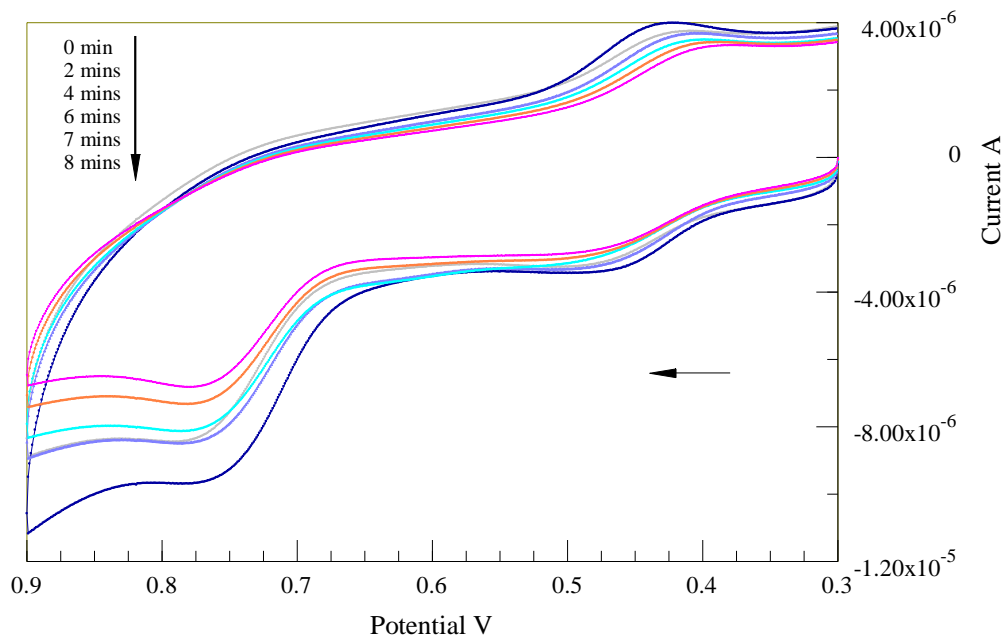


Figure 16: CV response for a time profile for removing 40 mg/L DCF after adding 0.08 g of IO-NPs at pH 7.02 in 0.1 M KCl using GCE, surface area (0.069 cm<sup>2</sup>), 300 mV/s.

### 3.1.3.2 Effect of time on MFA

To compare the time profile for MFA, different concentration of MFA was performed because it gave more precise results for the removal percentage of MFA rather than 20 mg/L as has been reported for DCF. Table 4 compares between nZVI and IO-NP at different times to show the removal percentage. nZVI gave a similar result as IO-NPs for MFA, Yet, the desorption occurred at a shorter time around 9 minutes which is shown in Figure 18. This indicates that the interactions are stronger with using IO-NPs. On the other hand, the adsorption effectiveness of MFA rose from 6.88 % to

39.83 %, when the contact duration was increased from 2 to 8 minutes by using nZVI and decreased to a 23.13 % at 9 minutes as can be seen in Table 4.

**Table 4: Time profile of MFA removal using NPs**

Time profile of 40 MFA removal using 0.08 g IO-NPs at 0.74 V potential				Time profile of 40 MFA removal using 0.08 g nZVI at 0.74 V potential			
Time (Minutes)	Current detected without NPs ( $\mu\text{A}$ )	Current detected with NPs ( $\mu\text{A}$ )	Removal percentage (%)	Time (Minutes)	Current detected without NPs ( $\mu\text{A}$ )	Current detected with NPs ( $\mu\text{A}$ )	Removal percentage (%)
0	13.36	13.36	0.00	0	12.50	12.50	0.00
2	13.36	10.88	18.56	2	12.50	11.64	6.88
3	13.36	9.20	31.10	3	12.50	10.06	19.52
4	13.36	8.36	37.42	5	12.50	9.29	25.63
5	13.36	7.93	40.62	7	12.50	8.30	33.54
7	13.36	6.39	52.12	8	12.50	7.52	39.83
10	13.36	11.00	17.67	9	12.50	9.60	23.13

As can be seen clearly in Figure 17, removal percentage kept increasing until it reached a maximum value at around 7 minutes and then it dropped down. The decrease in the removal percentage shown in Figure 17 indicates increasing the MFA percentage in the solution instead of being adsorbed on the NPs which can be explained as a reason due to the desorption of MFA from nZVI.

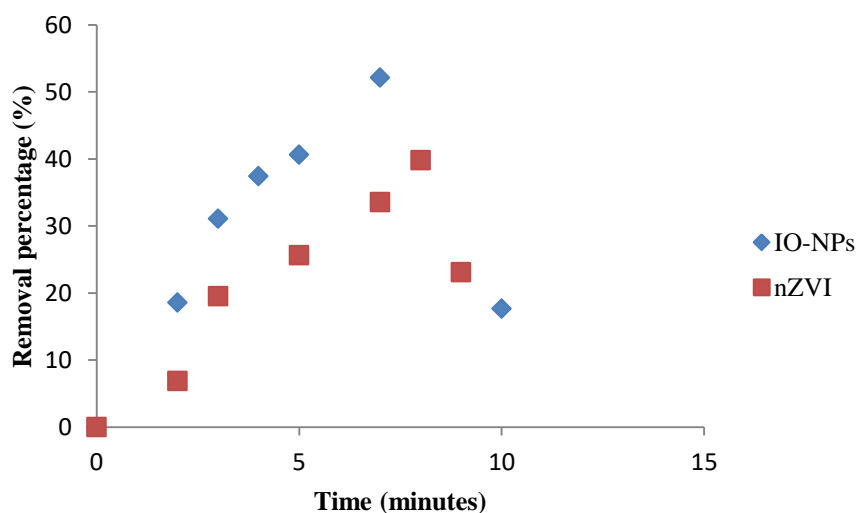


**Figure 17:** Time profile of 40 mg/L MFA removal percentage at 0.74 V by adding 0.08 g nZVI at pH 7.02 in 0.1 M KCl using GCE, surface area (0.069 cm<sup>2</sup>), 300 mV/s.

A CV scan was performed starting from 0.4 V to 1.0 V and was directly swept back to show the oxidation peak of MFA. A decrease in the current was noticed as time was increasing indicating that MFA was adsorbed on NPs surface and reducing its amount in water samples. Due to desorption of MFA from the nZVI surface at around 9 minutes as presented in Figure 18, it didn't provide an effective NP to be used for

the future experiments. In addition, the percentage removal was smaller compared to the one obtained by IO-NPs.

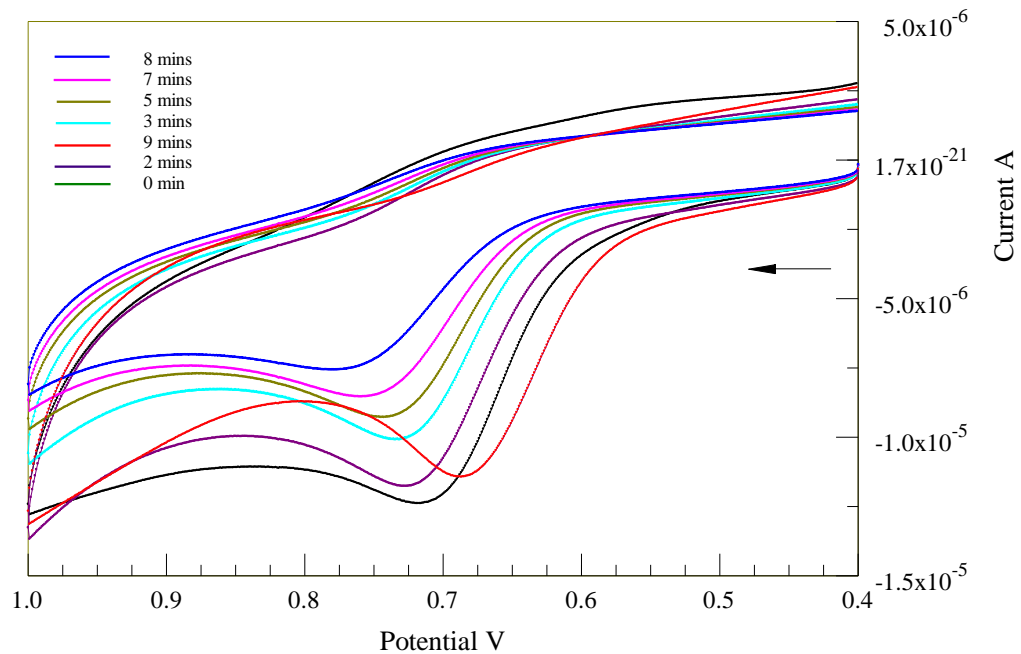


**Figure 18: CV response for time profile of removing 40 mg/L MFA using 0.08 g of nZVI at pH 7.02 in 0.1 M KCl using GCE, surface area (0.069 cm<sup>2</sup>), 300 mV/s.**

Meanwhile, IO-NPs showed higher removal percentage of MFA. The adsorption percentages were evaluated from Figure 19. The current started to decrease as time was passing showing good removal of MFA. The removal percentage increased from 18.56 % to 57.79 %, when the contact time was increased from 2 to 7 minutes by using IO-NPs and decreased to a 17.67 % at 10 minutes which indicates desorption of MFA from IO-NPs as shown in Table 4.

As a result, the optimal contact time was considered as 7 minutes which can be used in future experiments for removing MFA by using IO-NPs.

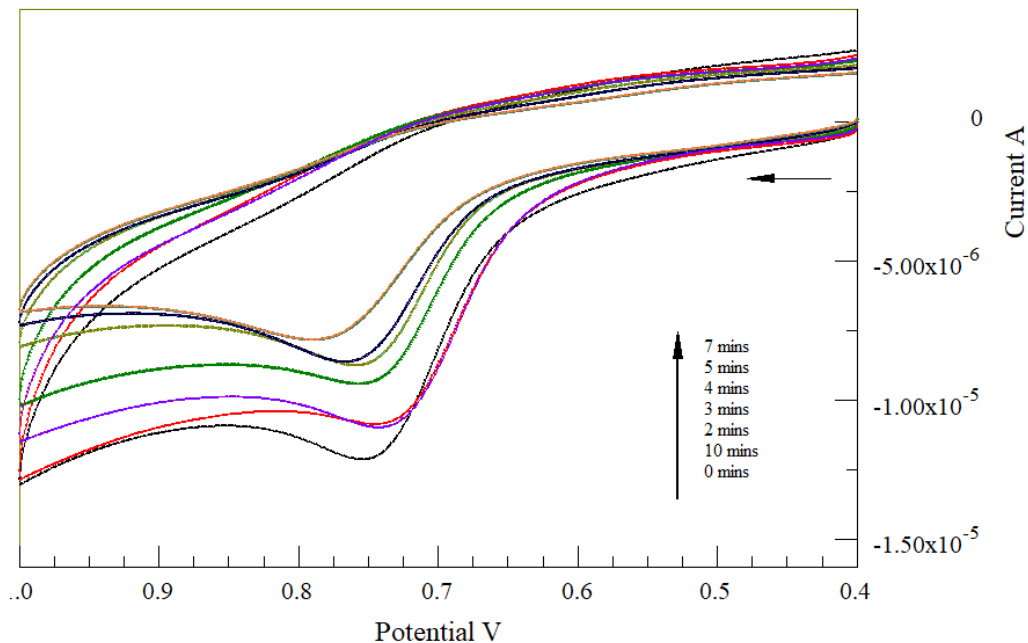


**Figure 19:** CV response for time profile of removing 40 mg/L MFA using 0.08 g of IO-NPs at pH 7.02 in 0.1 M KCl using GCE, surface area (0.069 cm<sup>2</sup>), 300 mV/s.

#### 3.1.4 Effect of Scan Rate

Figure 20 clearly shows how the current increases with increasing scan rate. Scan rate is related to the diffusion layer and the movement of species between the electrode and the solution interface. As the species get to the electrode surface, they gain or donate electrons to the electrode depending on its potential. The opposite charge species keep diffusing towards the electrode with the opposite charge until all sites get filled and diffusion of oxidized or reduced species starts to happen toward the solution. In fact the slower the scan rate the longer the time needed to record the scan



and therefore the diffusion layer components surrounding the electrode differed depending on the scan rate. Figure 20 shows the results of a series of LSV studies conducted at various speeds. As the scan rate rises, the voltammogram area grows as well, and the peak current occurs at higher voltage levels.

These results are as predicted, and they are comparable to those provided by others (Leftheriotis, Papaefthimiou, and Yianoulis 2007). The diffusion coefficient for the current peak can be determined using the Randles–Sevcik formula. It is expected for the diffusion coefficient to decrease with decreasing scan rate.

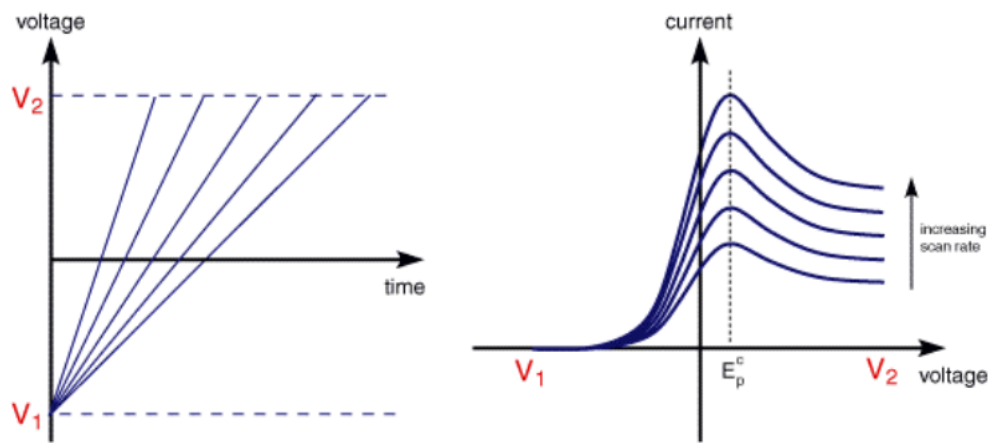


Figure 20: The effect of scan rate on the analyte's concentration in LSV method

From performing LSV of different scan speeds it has been observed that the peak current increases with the scan speed.

It's crucial to understand that current is defined as charge (or electrons passed) per unit time. The current going through the electrode in CV is restricted by the diffusion of species to the electrode surface. The diffusion flux is affected by the concentration gradient near the electrode. Also, the concentration gradient is influenced by the species concentration at the electrode and the rate at which the species may diffuse through solution. The Nernst equation states that altering the cell voltage changes the concentration of the species at the electrode surface. As a result of the larger voltage sweep, the concentration gradient at the electrode is bigger, resulting in a higher current which can be seen clearly in Figure 20 and Figure 21.

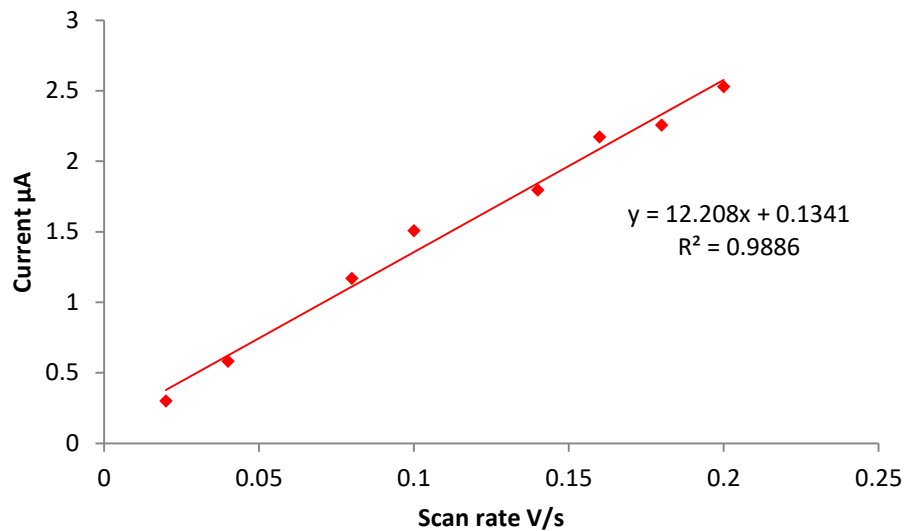
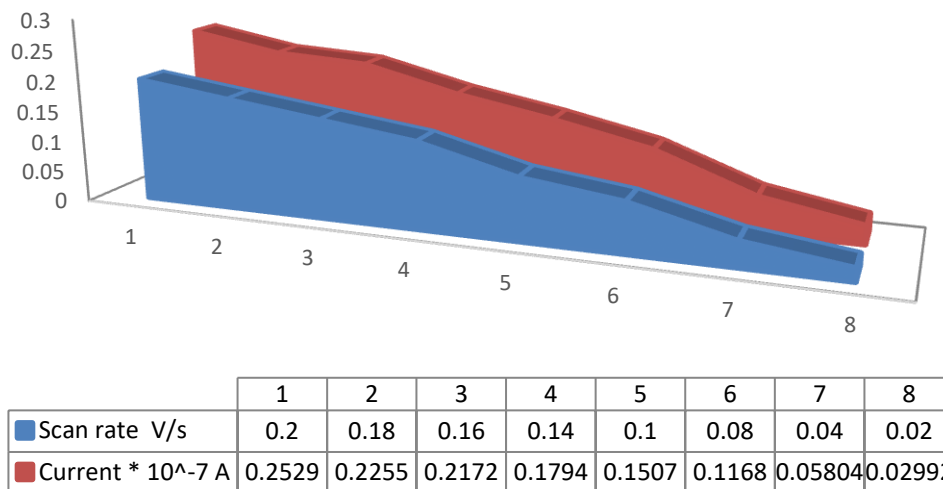


Figure 21: Current Vs scan rate for DCF removal using IO-NPs after 8 minutes, at 0.41 V potential, and  $10^{-5}$  sensitivity at different scan rates (0.2, 0.18, 0.16, 0.14, 0.1, 0.08, 0.04, and 0.02 V/s)

The electrochemical behavior was carried out and the reduction peak current was detected. Figure 22 presents a directly proportional relationship between scan rate and current, the faster the rate, the higher the current. Current increased from 0.29 to 2.52  $\mu\text{A}$  as scan rate increased from 0.02 to 0.2 V/s.



**Figure 22:** Effect of Scan rate on 40 mg/L DCF removal using IO-NPs. Scan rate is ranging from 0.02 to 0.2 V/s on the peak current of 40 mg/L MFA using GCE at pH 7.02 in 0.1 M KCl using GCE, surface area (0.069 cm<sup>2</sup>), 300 mV/s

The data was obtained from LSV response of a 40 mg/L DCF solution after adding IO-NPs at different scan rates which can be seen in Figure 23.

Different LSV of 40 mg/L have been obtained from 0.7 to 0.3 V to show the reduction peak and measure the cathodic peak for detecting DCF without using NPs at different scan rates. As can be seen in Figure 23 shows the directly proportional relationship between scan rates and DCF concentration.

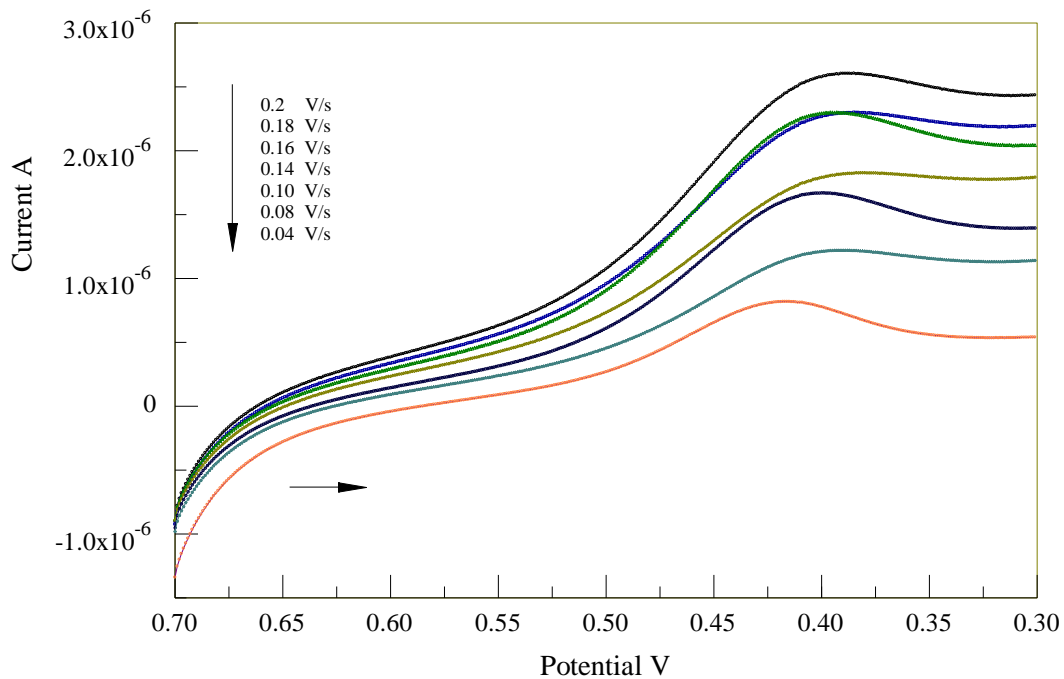


**Figure 23:** LSV response on the peak current of 40 mg/L DCF at pH 7.02 in 0.1 M KCl using GCE, surface area (0.069 cm<sup>2</sup>) at different scan rates (0.04-0.2 V/s)

Reduction peak current was plotted against square root of scan rate in Figure 24 and a straight line was obtained which confirms that the reduction was controlled by a diffusion process. The figure shows a very good linear relationship between peak current and scan rate.

Therefore, a linear relationship between both current and the square root of scan rate was found corresponding to the equation:

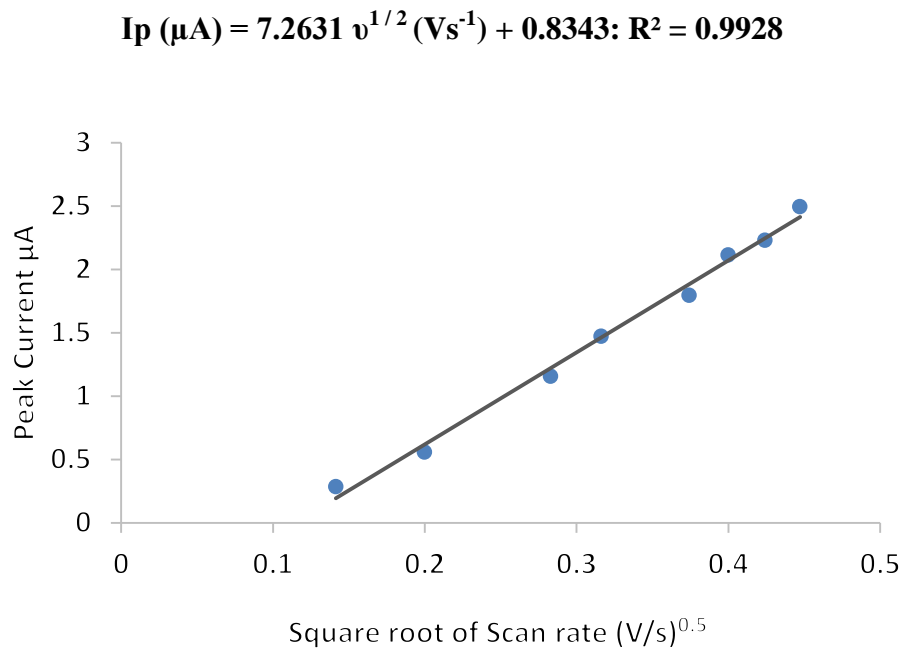


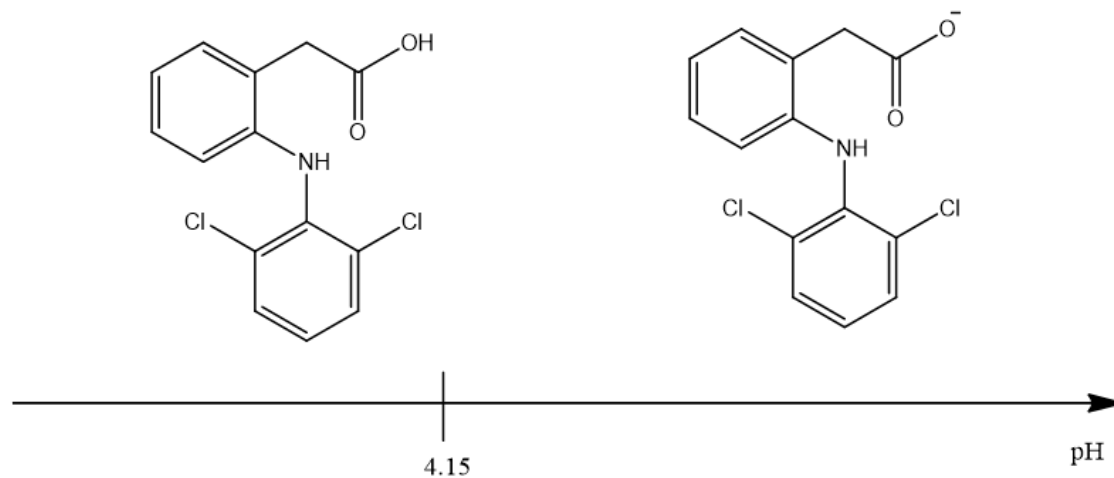
**Figure 24: Peak Current Vs Square Root of scan rate which was obtained from LSV response of the IO-NPs on the peak current of 40 mg/L DCF at pH 7.02 in 0.1 M KCl using GCE, surface area (0.069 cm<sup>2</sup>), 300 mV/s**

The coefficient of determination ( $R^2$ ) in Figure 24 shows a good linearity since its close to a 1 value and indicates that data points are not scattered. In addition, the slope was found to be 7.2631 as Figure 24 shows and it shows a direct proportionality between the square root of scan rate and peak current.

### 3.1.5 Effect of pH

#### 3.1.5.1 Effect of pH on DCF

The effect of pH on the current was inspected utilizing cyclic voltammetry. MFA and DCF were prepared in different buffers. CVs were performed at two pH values (4.04, and 7.02) for the electrochemical investigation of the pharmaceutical's removal. Alkaline media wasn't applied in DCF investigation since the chemical structure of DCF doesn't differ from the one at pH 7.04 as it was stated in previous study (Guzmán-Hernández et al. 2017). Since the structure is the same in basic media as the one in 7.04 pH buffer solution as Scheme 1 shows, acidic media was tested instead.



Scheme 1: DCF drug forms at different pH values

Attributed to this, it was found in previous research that the highest removal of DCF was at pH 3 due to the hydrogen bonding between DCF and nZVI. In basic media, DCF deprotonates forming COO<sup>-</sup> group. In addition, oxidation occurred on the surface of NPs forming a positive charge which forms electrostatic interactions.

Furthermore, nZVI presence in aqueous solution results in adhesion of H<sup>+</sup> ions on the surface which comes from water molecules. Due to this, hydrogen bonding is expected to form between H<sup>+</sup> and (–COO<sup>-</sup>) in DCF generating Fe(II)-DCF complex (S. M. Sulaiman and Al-Jabari 2021). With increasing pH, the removal efficiency decreased as well because of the repulsion forces between similar charges on DCF as Scheme 1 reveals and the OH<sup>-</sup> group accumulated on the NPs. Furthermore, the hydroxide ions block active surface sites by creating shells around nZVI particles, causing clogging (S. M. Sulaiman and Al-Jabari 2021).

The point of zero charge (pH<sub>pzc</sub>) provides details on the charges on the adsorbent surface as well as the point at which the material's net surface charge (positive and negative charges) are equal.

Based on previous data, it can be concluded that the pH<sub>pzc</sub> was around 6.0 and that the net charge on the surface of Fe<sup>0</sup> is positive when pH < pH<sub>PZC</sub> and negative when pH > pH<sub>PZC</sub> (Al-Kindi et al. 2021).



At pH 7.02, the creation of hydrogen bonds by positively ionizing the  $\text{Fe}^0$  surface and deprotonating DCF(-CO-) or by forming the Fe(II)-DCF complex might have formed since DCF has a negative surface and nZVI had a positive charge (N.Al-Rimawi et al. 2022). On the other hand, as pH decreases to  $< 4.15$ , DCF structure starts having (COOH) group and nZVI start having a positive surface. Due to the similar charges, hydrogen bonding start to form instead of electrostatic interactions.

As the pH decreases, more protons would be more accessible affecting the adsorbent's surface charge (Al-Kindi et al. 2021). Electrostatic attraction becomes stronger between the DCF and the adsorbent which clearly presented in Figure 25 as the peak current decreases. On the other hand, basic media might not perform the best removal percentage since nZVI and DCF have a negative surface and repulsion forces might occur instead.

Removal percentage was evaluated of DCF after using nZVI under 4.04 pH media. It was found that the removal has occurred immediately and the % removal reached up to a value of 97.05 % for 40 mg/L DCF which was higher than the one obtained for 40 mg/L under 7.02 pH (65.54).

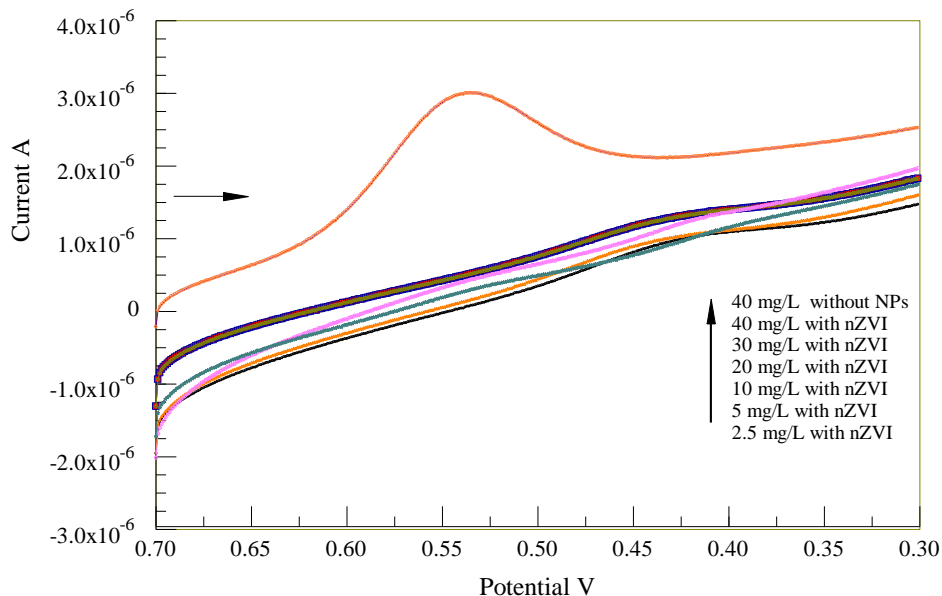


**Figure 25: LSV response for effect of pH on 40 mg/L DCF removal using 0.08 g of IO-NPs in a pH 4.04 in 0.1 M KCl using GCE, surface area (0.069 cm<sup>2</sup>), 300 mV/s.**

DCF removal percentage was compared between pH 4.04 and 7.02 buffer solutions. It was found that percentage removal in pH 4.04 (24.60%) was almost the same as the one in pH 7.02 (25.30%).

As can be seen in Figure 26, the peak potential of DCF shifted toward more negative values with using nZVI at pH 7.02. This confirms that the extent of the reaction was affected and the reaction occurred favors the products making  $K > 1$  according to the change in Gibbs free energy and its connection with electrical measurements based on Nernst equation 6.

$$\Delta G^{\circ} = - nF\Delta E^{\circ} \dots(7)$$

Where  $\Delta G^\circ$  is free Gibbs energy,  $F$  is Faraday's constant,  $\Delta E^\circ$  is the potential difference which is called the electromotive force (emf),  $E$ , of the cell, and  $n$  is the stoichiometric coefficient of the electrons in the cell's half-reactions into which the cell reaction can be divided (Sataloff, Johns, and Kost 2006).

The steepness of the graph in Figure 26 has changed as pH of the solution was adjusted to different values. CV of 40 mg/L DCF in a 4.04 pH buffer solution has shown a reduction peak at potential 0.53 V with a current peak  $3.90 \mu\text{A}$ . The reduction peak at pH 4.04 was steeper than the one obtained at pH 7.02. The steeper the curve the faster the species get oxidized which reflects the kinetic aspect of the process.

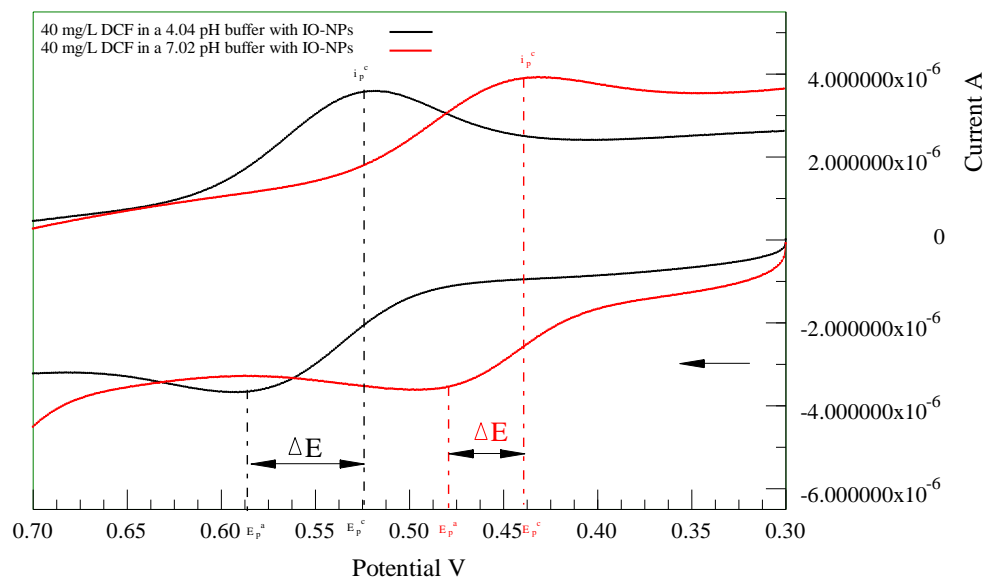


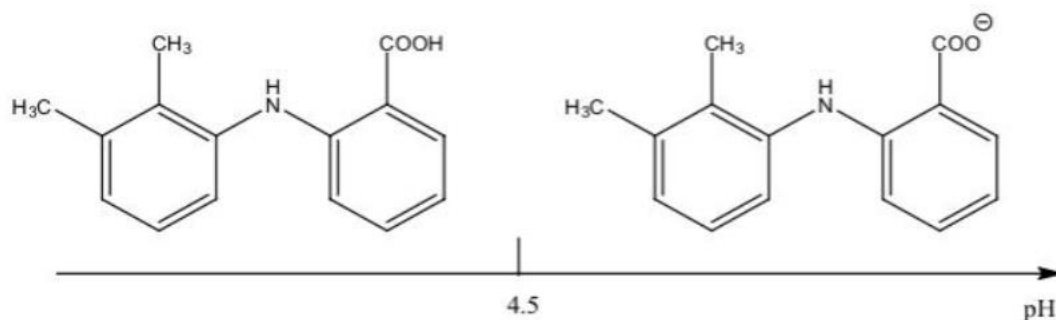
**Figure 26:** CV response for effect of IO-NPs on 40 mg/L DCF removal using pH 4.04 and 7.02 buffer solutions in 0.1 M KCl using GCE, surface area ( $0.069 \text{ cm}^2$ ), 300 mV/s.

Moreover, a peak shift was observed as the buffer solution changed. As pH decreased a shift to the more positive direction took place as illustrated in Figure 26.

The reduction peak potential  $E_p^c$  changed from 0.42 V to 0.53V as the pH changed from 7.02 to 4.04 as presented in Figure 26. Throughout applying Equation (7),  $\Delta G^\circ$  was calculated to be  $-23.04$  kJ/mol. This result indicates that the process prefers the products comparing to neutral media making  $K < 1$ .

#### *3.1.5.2 Effect of pH on MFA*

MFA exists in different forms depending on the solution pH. When MFA was prepared in a pH 4.02 buffer solution, it was expected to have a structure with a positive nitrogen atom which was protonated in an acidic media and another negative charge from the carboxylic group as Scheme 2 shows. On the other hand, in 7.02 and 10.06 pH buffer solution, MFA was able to interact with the NPs surface due to the electrostatic interaction between the negative charge and the adsorbent's surface (AL-Abbassi et al. 2020)



**Scheme 2: Mefenamic acid forms at different pH values**

The pKa value of MFA in aqueous medium was found to be 4.5; therefore, surface of electrode becomes negatively charged on carboxylic acid group (COO<sup>-</sup>) at pH 7.02 and 10.06 values.

While removing MFA using IO-NPs in basic media, the magnetic NPs start having a negative charge and the analyte adsorption increases in pH value up to 10 which is shown in Figure 27 and this also agrees with a previous study (Beiraghi et al. 2014). The adsorption efficiency is greatly reliant on different factors mainly the charge and the morphology of the pharmaceuticals which is presented in Scheme 2. As pH was increasing, the adsorption capacity is supposed to increase as it exceeds its pKa value (5.4) and starts having a new form with a negative charge. Figure 24 shows how the current was almost the same for pH 7.02 and 10.06. The result agrees with the results assumed in the beginning since both pH values exceed pKa of MFA.

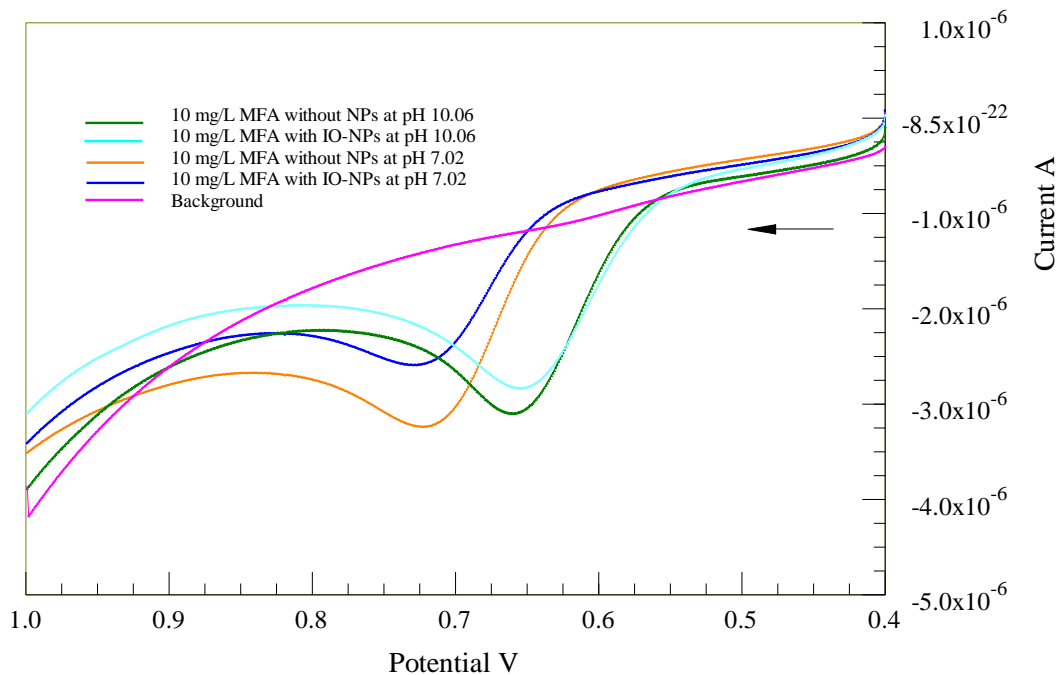


**Figure 27: LSV response for effect of pH on 10 mg/L MFA removal using 0.08 g of IO-NPs in a pH 10.06 and 7.02 in 0.1 M KCl using GCE, surface area (0.069 cm<sup>2</sup>), 150 mV/s.**

$\Delta G^\circ$  was found to be + 6.91 kJ/mol when the solution was prepared at pH 10.06. This indicates that the oxidation at pH 10.06 has a value of  $K < 1$  (favoring the reactants) compared to 7.02 buffer solution which has  $K > 1$  (favoring the product). In addition, as  $\Delta G^\circ < 0$ , it means that  $K > 1$  and that the reaction favors the adsorption process on the NPs surface. As a result, MFA removal percentage was compared between pH 10.06 and 7.02 buffer solutions. The use of neutral buffers was preferred since that percentage removal in pH 10.06 (8%) was less than the one in pH 7.02 (20%).

Based on previous data, it can be concluded that the  $pH_{pzc}$  was around 6.5 and that the net charge on the surface of  $Fe^0$  is positive when  $pH < 6.5$  and negative when  $pH >$

6.5. At pH 7.02, the creation of hydrogen bonds by negatively ionizing the  $\text{Fe}^0$  surface and deprotonating MFA might have formed. On the other hand, as pH decreases to  $< 4.5$ , MFA structure starts having (COOH) group and IO-NP start having a positive surface. Due to the similar charges, repulsion forces might occur and removal percentage decreases (Jonoush, Rezaee, and Ghaffarinejad 2020).

MFA was also prepared in a 4.04 pH solution. For this experiment, the oxidation peak didn't appear in the CV shown in Figure 28. In this case,  $\text{pH} < \text{pKa}$  of MFA and the drug had a different structure with a positive charge and the peak response of MFA disappeared. At pH 4.5, neutralization occurred since MFA structure carries a positive charge on  $\text{NH}_2^+$  group and a negative sign on  $\text{COO}^-$ . Additionally, MFA starts to precipitate especially under a pH lower than its pKa value As it has been reported recently (AL-abbassi et al. 2020).

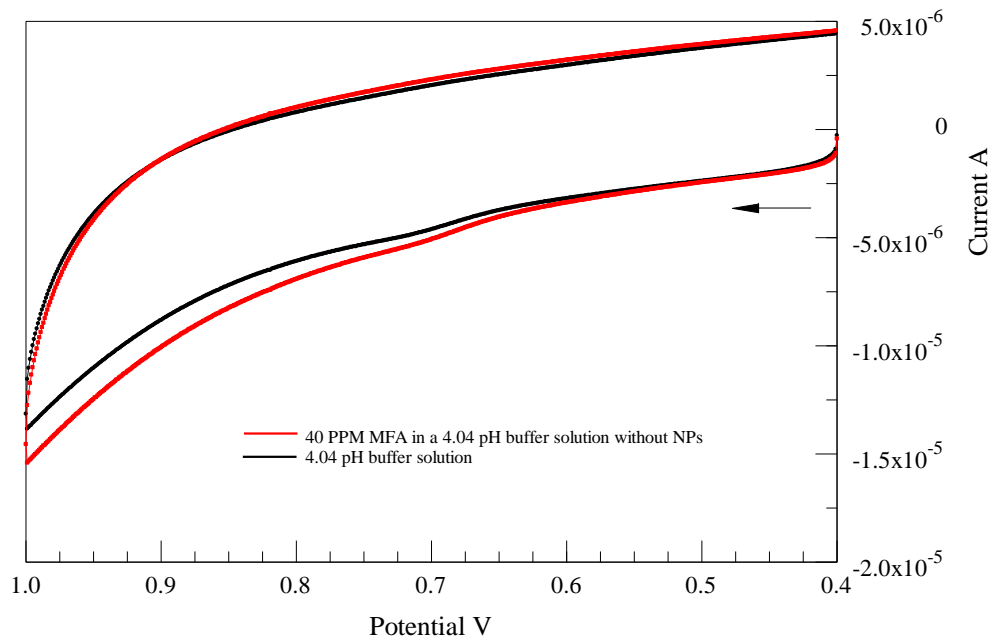


Figure 28: CV response for effect of pH on 40 mg/L MFA removal in a pH 4.04 in 0.1 M KCl using GCE, surface area ( $0.069 \text{ cm}^2$ ), 150 mV/s.

### 3.1.6 Effect of Temperature

#### 3.1.6.1 Effect of temperature on DCF

Effect of temperature on removal of drugs; MFA by IO-NPs and DCF by nZVI was investigated at 291, 281 K and different concentrations of 40, 30, 20, 10, and 5 mg/L. Different concentrations of DCF were scanned after the addition of nZVI under 10 °C. As temperature decreased, the removal percentage was evaluated from Figure 29 and was found to be 53.41 % for 40 mg/L DCF. On the other hand, percentage removal at room temperature was slightly higher for the same concentration and was found to be 65.54%. This result can be explained due to the higher kinetic energy and higher solubility of DCF which speeds up the adsorption process on the NPs surface.



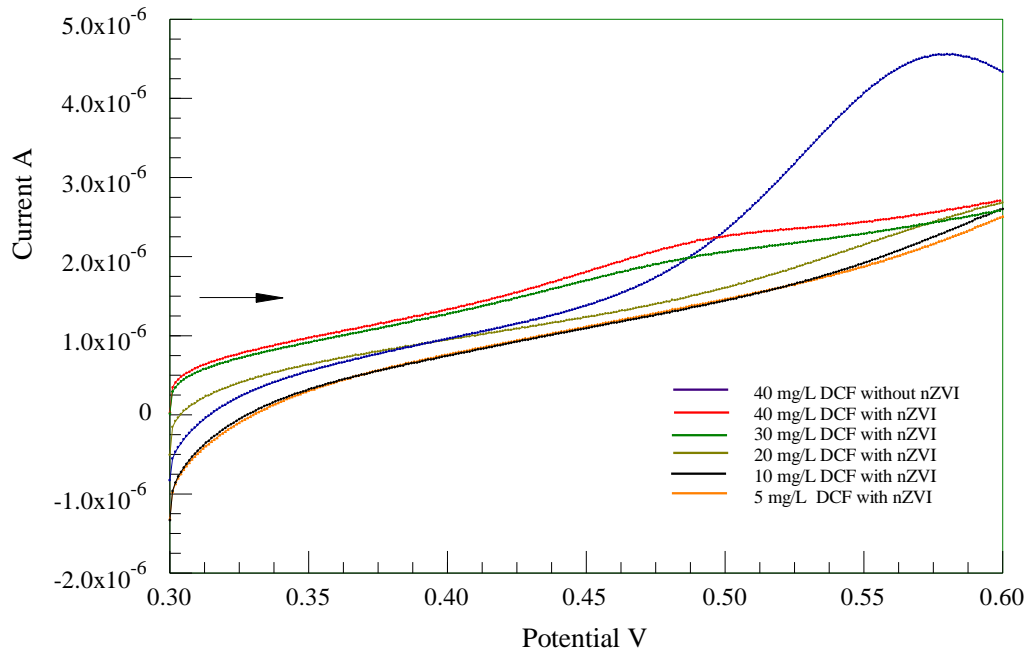


**Figure 29:** A LSV response of the effect of temperature 10°C on the peak current of 40, 30, 20, 10, and 5 mg/L m DCF after adding 0.08 g of nZVI in the aqueous solution at pH 7.02 in 0.1 M KCl using GCE, surface area (0.069 cm<sup>2</sup>), 150 mV/s

Drug removal under high temperature wasn't performed in this study since it was reported that as the temperature increases above 25°C, the adsorption didn't change and the removal didn't exceed the one at room temperature (S. M. Sulaiman and Al-Jabari 2021). As temperature increased, kinetic energy increased which led to an increase in the adsorbed amounts of the adsorbent on the NPs surface due to increasing the mobility and higher ability to contact with the NPs' surface.

### 3.1.6.2 Effect of Temperature on MFA

For MFA, oxidation peak current without IO-NPs didn't change from the one with IO-NPs after decreasing temperature as it's represented in Figure 30. As a consequence, it indicates that the process doesn't favor low temperature and the

adsorption was more effective as temperature was increasing in the range of room temperature. Meanwhile, a slight shift towards a more positive direction occurred when the removal was performed at room temperature compared to the one at 10°C which resulted a  $+\Delta G^\circ$  value. This also specify that the reaction has a K value larger than 1. In addition, the shape of the peak represented the kinetic aspect of the reaction. The scan at temperature 10°C wasn't as steep as the one at room temperature which means that the reaction is slower and the adsorption takes longer time at lower temperature values.

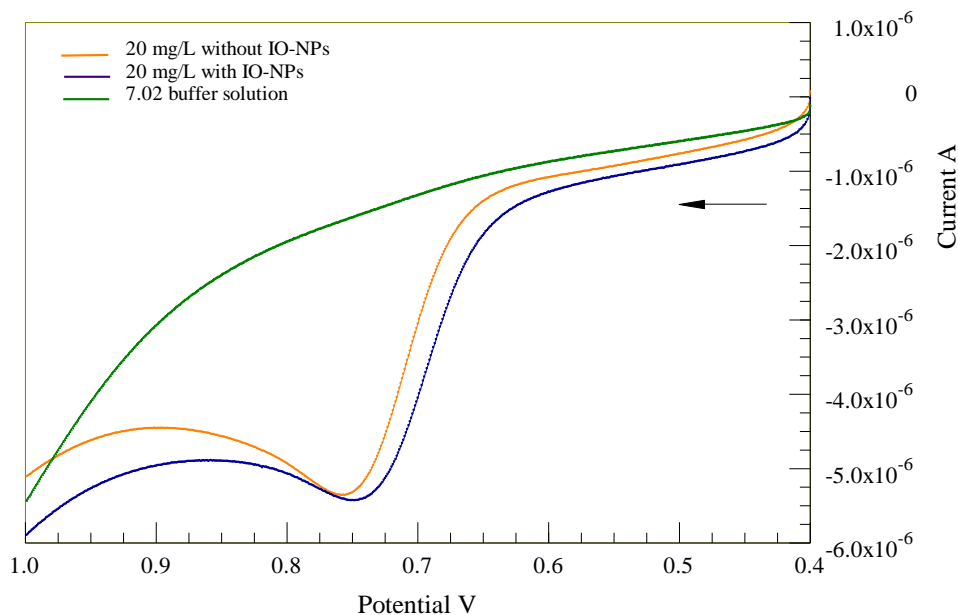


**Figure 30:** A LSV response of the effect of temperature 10°C on the peak current of 20 mg/L DCF after adding 0.08 g of IO-NPs in the aqueous solution at pH 7.02 in 0.1 M KCl using GCE, surface area (0.069 cm<sup>2</sup>), 300 mV/s

The impact of high temperature on the MFA removal wasn't investigated in this research. The influence of temperature of MFA was determined by other researchers

in the range of 15°C—55°C and the results indicated that percentage removal has reached to 99% at 55°C (S. Sulaiman and Shahwan 2017). The reason behind this result might be the increase in kinetic energy. Another reason might be that increasing the temperature improves the solubility of MFA drug in the medium, increasing their adsorption capability (Bakr et al. 2018).

### 3.2 Electrochemical Characterization of MFA

MFA has showed only one oxidation peak at around 0.72V as can be seen in Figure 31 after the LSV was swept from 0.4 V to 1.0 V. The anodic peak of the electrochemical oxidation of MFA was performed. In this system, a 1 e<sup>-</sup> transfer is involved in this process (Bukkitgar et al. 2014).

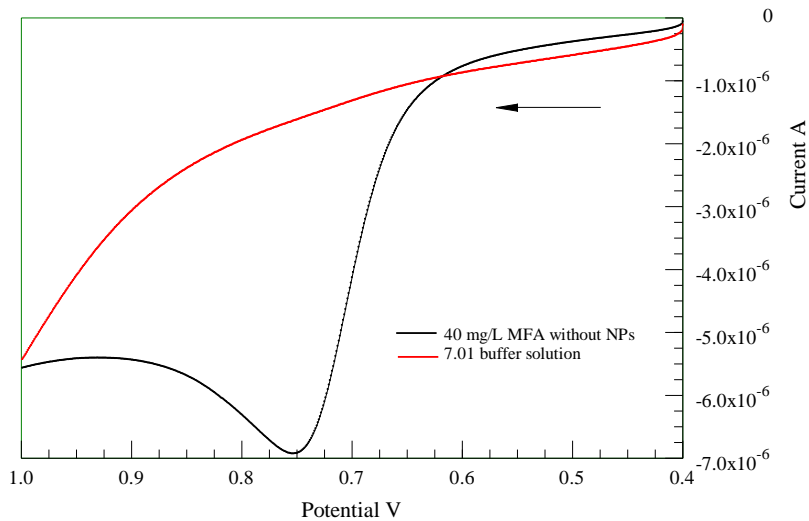
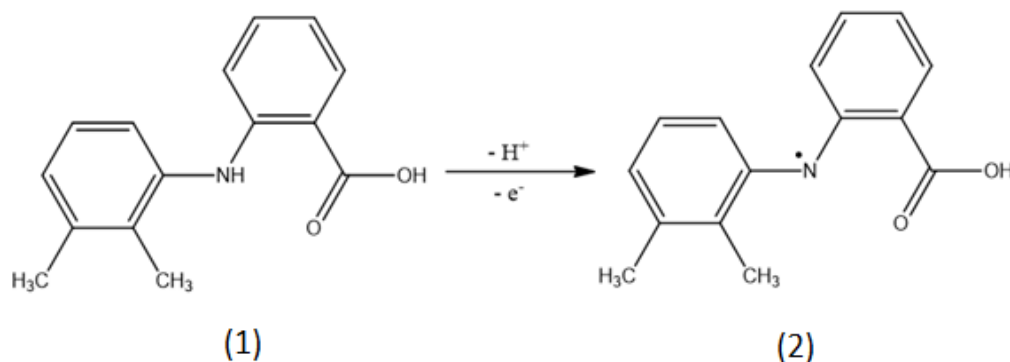


**Figure 31: LSV response of 40 mg/L MFA in a pH 7.01 in 0.1 M KCl using GCE, surface area (0.069 cm<sup>2</sup>), 150 mV/s.**

With this knowledge, the reaction can be presented for the oxidation of MFA at the surface of GCE. The reaction is given in the reaction below.



In the reaction above, the nitrogen electron was lost instead of the one for carboxylic acid because of the conjugated effect which stabilize the structure by delocalizing the radical form.

### 3.3 Electrochemical Characterization of DCF Drug

The cyclic voltammograms (CVs) are obtained in the presence of 40 mg/L DCF. The glassy carbon electrode (GCE) exhibit two oxidation peaks at around 0.5 and 0.8 V respectively, when the sweep was initiated in the positive direction. Another peak was also detected for reduction at around 0.45 V. All peaks were observed on the

reverse scan indicating that the electron transfer on the GCE is irreversible. The scan rate was fixed at  $0.3\text{V s}^{-1}$ .

The CV measurement of DCF in Figure 32 supports the DCF oxidation scheme. DCF produces a single irreversible oxidation peak at roughly  $0.80\text{ V}$  in the scan cycle, as seen in Figure 32, which can be attributed to DCF oxidation to 5-OH DCF (peak (2)). A reduction peak was seen in the reverse scan at around  $0.45\text{ V}$  (peak (3)) indicating the presence of DCF 2,5-quinone imine, with an oxidation peak at about  $0.50\text{ V}$ .

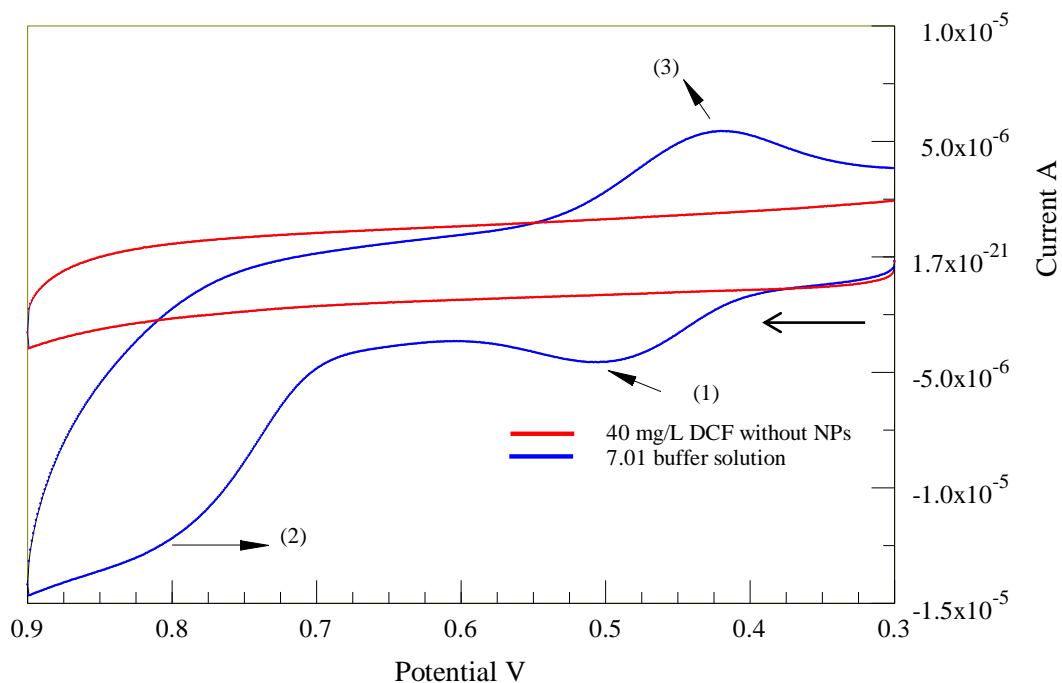
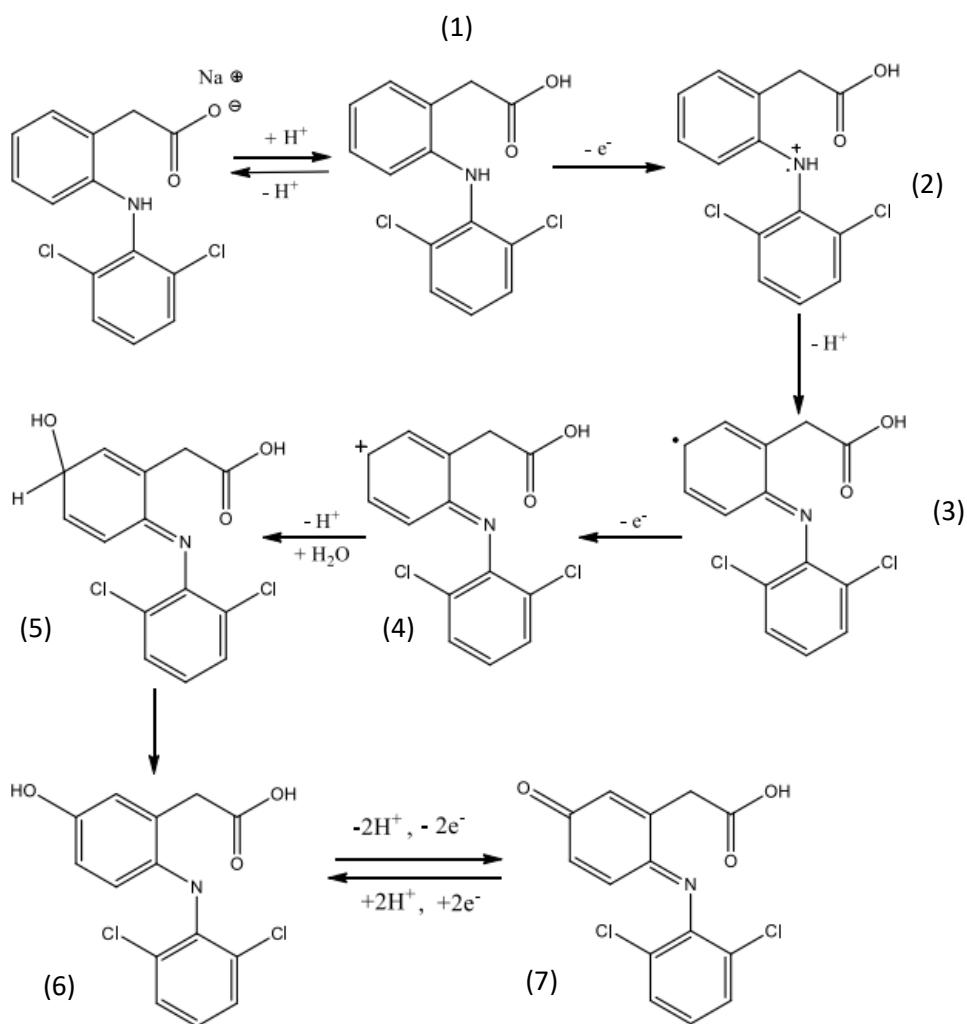


**Figure 32:** CV of 40 mg/L DCF in a in a pH 7.02 in 0.1 M KCl using GCE, surface area ( $0.069\text{ cm}^2$ ), scan rate of  $300\text{ mV/S}$ , and over a potential range from  $0.3$  to  $0.9\text{ V}$

$\Delta E^{\circ}$  was measured for DCF for the conversion of 5-OH DCF to DCF 2, 5-quinone imine and was found to be 0.042 V. According to  $\Delta E^{\circ}$  value, it was assumed that it could be the cause of this reversible redox pair since it is  $< 59/n$  mV.

Scheme 3 depicts the electrochemical activity of DCF. The first step includes the removal of one electron (1), which results in the production of a radical cation with a nitrogen core (2). The radical cation undergoes rearrangement and de-protonation, resulting in a carbon-centered radical para to the amino group (3), followed by a second electron withdrawal to form a carbocation (4). The carbon cation combines with water and the intermediate aromatizes to produce 5-OH DCF (5). As a result of the loss of  $2e$  and  $2H^{+}$ , DCF is oxidized to 5-OH DCF (Mekassa et al. 2018).

A reversible electrode reaction using  $2e$ ,  $2H^{+}$  forms quinone imine (7) from the 5-OH DCF intermediate.



Scheme 3: Reactions for the electro-oxidation of DCF (Mekassa et al. 2018)

The oxidation peak (around 0.80 V) was unstable and dropped sharply during subsequent scan cycles, whereas the reversible redox pair produced highly persistent redox peaks. It only further demonstrates that the development of the unstable 5-hydroxy DCF intermediate causes the first anodic peak, but the formation of stable

equilibration between 5-OH DCF and DCF 2,5-quinone imine causes the redox pair to be stable. As a result, for the measurement of DCF in this study, the voltammetric signals corresponding to the other anodic peak current (around 0.50 V) were frequently recorded (Mekassa et al. 2018).

The linear relationships between MFA and DCF peak current  $I_p$  and the concentration in the Randles-Sevcik equation indicated that current is directly proportional to the analyte's concentration.

$$i_p = (2.69 \times 10^5) n^{3/2} A C D^{1/2} v^{1/2}$$

Where  $i_p$  is the peak current in amperes (A), the constant has a unit of  $A \text{ s V}^{-1/2} \text{ mol}^{-1}$ ,  $n$  is number of electrons appearing in the half reactions,  $A$  the electrode area in  $\text{cm}^2$ ,  $C$  is concentration in  $\text{mol.cm}^3$ ,  $D$  is the diffusion coefficient in  $\text{cm}^2.\text{s}^{-1}$ , and  $v$  is the scan rate in  $\text{V.s}^{-1}$  (Townshen 1983).

### *3.4 Physicochemical characterizations DCF drug*

#### *3.4.1 IR Characterization*

In order to inspect any possible interactions between drugs DCF and NPs, Fourier transform infrared (FT-IR) was performed. Initially, FT-IR spectra of DCF drug are shown in Figure 33. The spectrum clearly shows well-defined peaks at around  $3386.75 \text{ cm}^{-1}$  (N-H amine),  $748.22 \text{ cm}^{-1}$  ( $\delta$  C-H<sub>aromatic</sub>),  $448.26 \text{ cm}^{-1}$  (C-Cl),  $3203.76 \text{ cm}^{-1}$  (COOH carboxylic acid),  $1281.66 \text{ cm}^{-1}$  (C-N),  $3079.61 \text{ cm}^{-1}$  (C-H<sub>aromatic</sub>), and  $1500.35 \text{ cm}^{-1}$  (C=C). different peaks are in agreement with previous studies such as



1503  $\text{cm}^{-1}$  for (C=C), 1289  $\text{cm}^{-1}$  for (C-N), and 3383.75  $\text{cm}^{-1}$  for (N-H amine) (S. M. Sulaiman and Al-Jabari 2021).

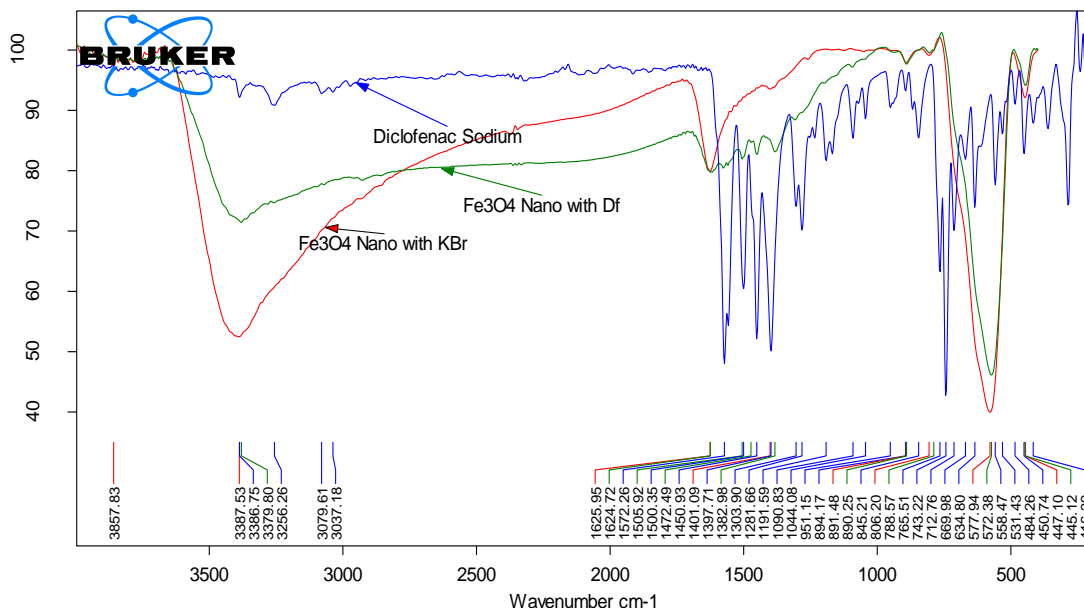


**Figure 33: Fourier transform infrared spectroscopy (FTIR) spectra: (blue) diclofenac sodium DCF; (red)- Fe<sub>3</sub>O<sub>4</sub> particles with KBr; and (green) is Fe<sub>3</sub>O<sub>4</sub> with both KBr and DCF.**

Later, the surface of the iron (IV) oxide NPs was characterized with KBr and spectra was recorded as it can be seen in Figure 33. The bare super magnetic NPs were determined by 577.94  $\text{cm}^{-1}$  (the vibration of Fe-O bonds). In addition, the surfaces of the NPs were covered by O-H groups in the process of preparing Fe<sub>3</sub>O<sub>4</sub> NPs by the chemical co-precipitation. Due to the presence of hydroxyl group, other peaks have appeared at around 1625.95 and 3387.53  $\text{cm}^{-1}$ . The data presented is in line with earlier studies.

The vibration of Fe-O bond was shown in (Kan et al. 2009) at around  $580\text{ cm}^{-1}$  and in the range of  $579\text{-}635\text{ cm}^{-1}$  (Wan Nor et al. 2018). O-H groups have been detected at around  $1630\text{ cm}^{-1}$  since they cover the magnetic NPs surface (K. Yang et al. 2010). Fe-OH bond was also identified at  $1609$  and  $3369\text{ cm}^{-1}$  (Wan Nor et al. 2018).

The following step was recording FT-IR spectrum of dried nZVI at room temperature which was homogenized with a sample of KBr which is presented in Figure 34. The spectrum was obtained for the range between  $500$  and  $4,000\text{ cm}^{-1}$ . A peak at  $3,425.61\text{ cm}^{-1}$  was detected and attributed to hydroxyl stretching vibration and the other peak at  $1,630.70\text{ cm}^{-1}$  which was ascribed to O-H bending vibration of the adsorbed water on the surface. These two peaks indicate that nZVI go through oxidation which led to the formation of ferrioxyhydroxide layer (FeO-OH) on the NPs' surface.

The stretching band of Fe-O occurred at  $476.89$  and  $1030.22\text{ cm}^{-1}$ . The results supports previous data which shows the oxidation of NPs from the stretch of O-H bond at  $3,421\text{ cm}^{-1}$ . Furthermore, bending vibration was identified at around  $1641\text{ cm}^{-1}$  (Singh, Misra, and Singh 2011).

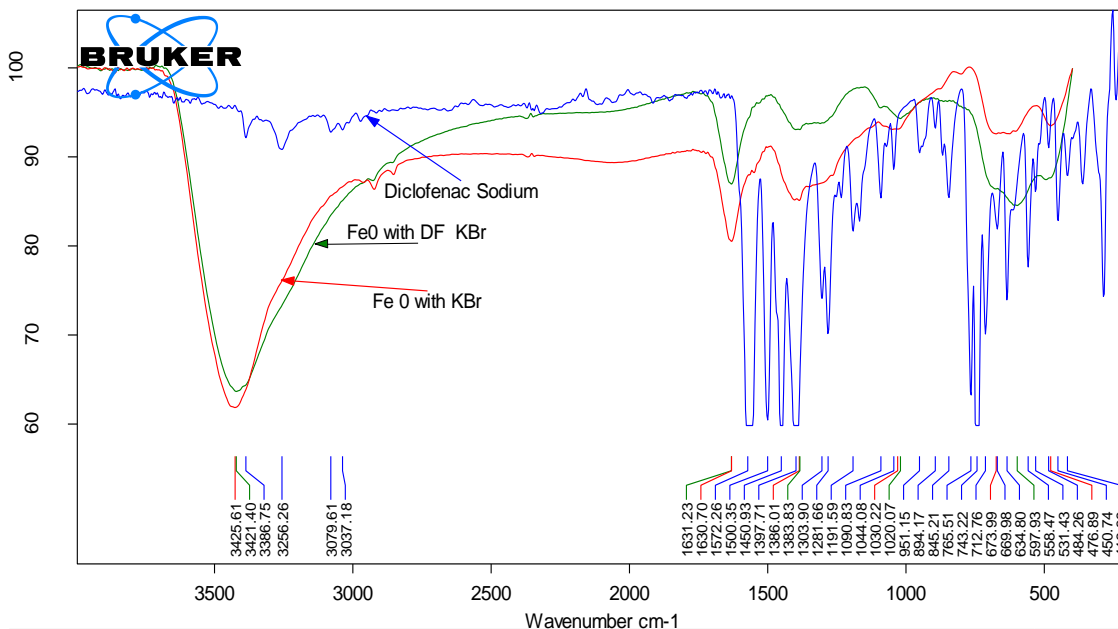


**Figure 34: Fourier transform infrared spectroscopy (FTIR) spectra: (blue) diclofenac sodium DCF; (red)-nZVI with KBr; and (green) is nZVI with both KBr and DCF.**

DCF was further characterized after the adsorption process by FTIR in the wavelength range of 400–4000  $\text{cm}^{-1}$  to determine the chemical bonding on the surface of NPs and the desired analytes as seen in Figure 33 and Figure 34. Due to the small amounts used in this method, it wasn't able to detect a change on the NPs since the largest amount used, the analyte's peaks didn't appear on the NPs surface since the largest amount used in this research was 40 mg/L.

Number of new bands appeared at in FT-IR spectrum Figure 33 for the adsorption of DCF on IO-NPs surface (1382.98, 1472.49, 1505.92, and 1624.72  $\text{cm}^{-1}$ ) bands were attributed to the presence of DCF after adsorption on IO-NPs.

### *3.4.2 SEM and TEM characterization*

SEM and TEM were used to characterize the synthesized adsorbents (nZVI). SEM and TEM methods were used to analyze the surface morphology of Fe<sup>0</sup> of the same batch used in this study. A chain-like structure of spherical NPs with an average diameter of 60 nm was formed by aggregating Fe<sup>0</sup> NPs as evidenced by the structure and surface morphology of Fe<sup>0</sup>. The effectiveness of the contaminants' removal might decrease because the aggregation of Fe<sup>0</sup> NPs diminishes their surface area and restricts their ability to disperse in the solution (N.Al-Rimawi et al. 2022).

## *3.5 Calibration Curves of the pharmaceutical's removal using NPs*

### *3.5.1 Calibration Curves of DCF*

Firstly, DCF determination after the adsorption on the NPs was carried out in PBS solution. Figure 35 shows CV for 40 mg/L concentration of DCF. A calibration curve was obtained for the reduction peak current shown around a potential of 0.41 V after 8 minutes of IO-NPs. A linear increase of currents was observed with increasing concentrations of DCF. The result indicates that it is feasible to electrochemically detect DCF.

Figure 35 shows how all three peaks current decreases as we add IO-NPs. For calibration curve, the reduction peak at around 0.41 V was chosen to indicate the relationship between current and concentration.

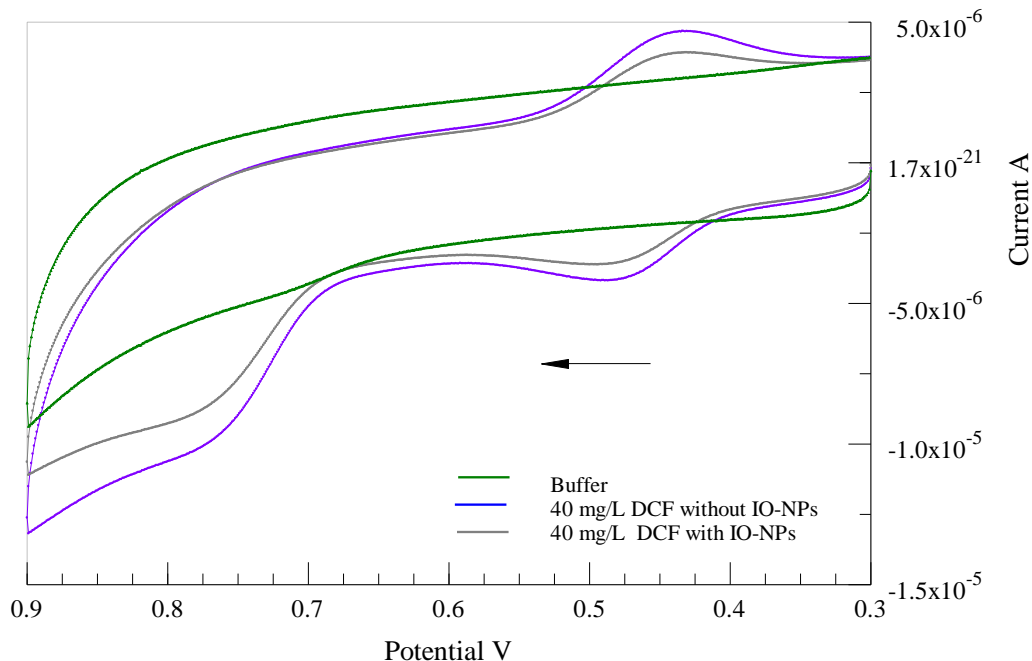


**Figure 35: CVs of 40 mg/L DCF in a pH 7.02 PBS in 0.1 M KCl using GCE, surface area (0.069 cm<sup>2</sup>), 300 mV/s. with and without IO-NPs**

To better show the effect of the IO-NPs addition, calibration curves for different DCF concentrations were constructed while keeping the NPs dose and pH value the same.

Figure 36 shows a series of data points for the cathodic current obtained: 7.02 pH buffer solution serving as a background, DCF solutions prepared in a 7.02 pH buffer without IO-NPs, and DCF solutions prepared in a 7.02 pH buffer with IO-NPs. The slopes of calibration curves presented in Table 5 shows improvement in

electrochemical detection when the potential was held constant at 0.4100 V. Slopes for each calibration curve were compared which refer to the sensitivity and removal extent. The slope of line B after NPs addition was found to be less than line A which means its less steeper and the drug was removed with IO-NPs addition.

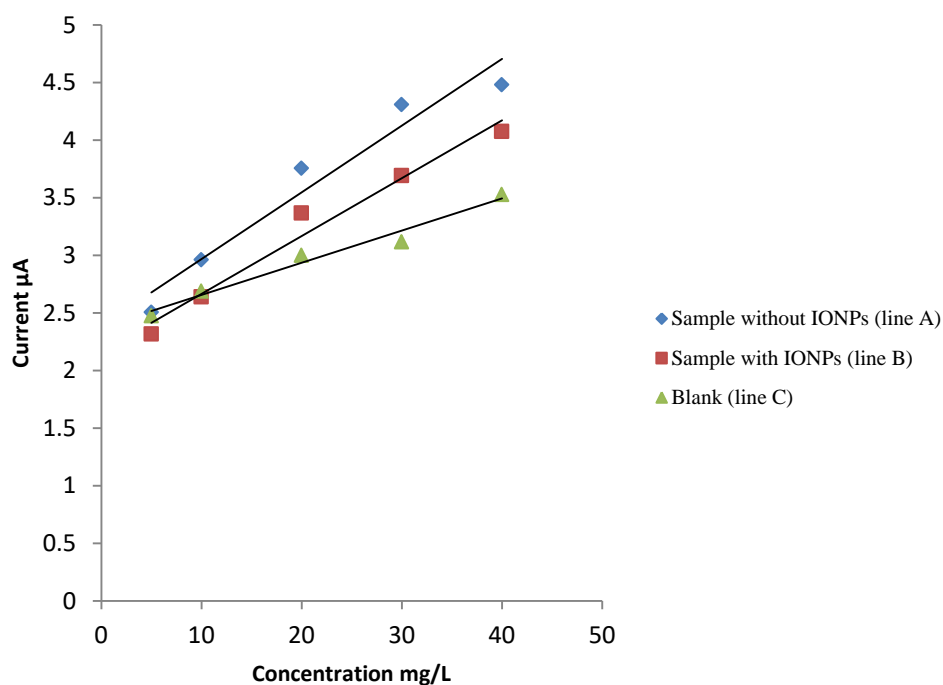


Figure 36: Calibration curve for DCF removal using IO-NPs after 8 minutes, in a pH 7.02 in 0.1 M KCl. The potential was kept at 0.4100V

On the other hand, coefficient of determination  $R^2$  of calibration curves were determined for each line.  $R^2$  is a measure of how well a set of data fits a calibration curve. It was found to be smaller for lines A and C than for line B which means that

data points for line A and C fits the calibration line the most. As we use IO-NPs to remove DCF, it was reported in Table 7 that the drug's concentration decreases, this agrees with the slopes magnitude and the steepness calibration line with and without NPs. The percentage removal was reported to be 9.10% for 40 mg/L DCF after IO-NPs in Table 7.

Later on, DCF was removed almost completely by using nZVI as can be seen in Figure 37 due to the electrostatic attraction forces between nZVI and either carboxylic or amine group on the DCF surface.

LSV in Figure 37 shows how the reduction peak current at potential around 0.4 V has faded as nZVI were added to the water sample. LSV for 40 mg/L DCF solution with nZVI has showed a high removal percentage up to 65.54 % as Table 7 shows.

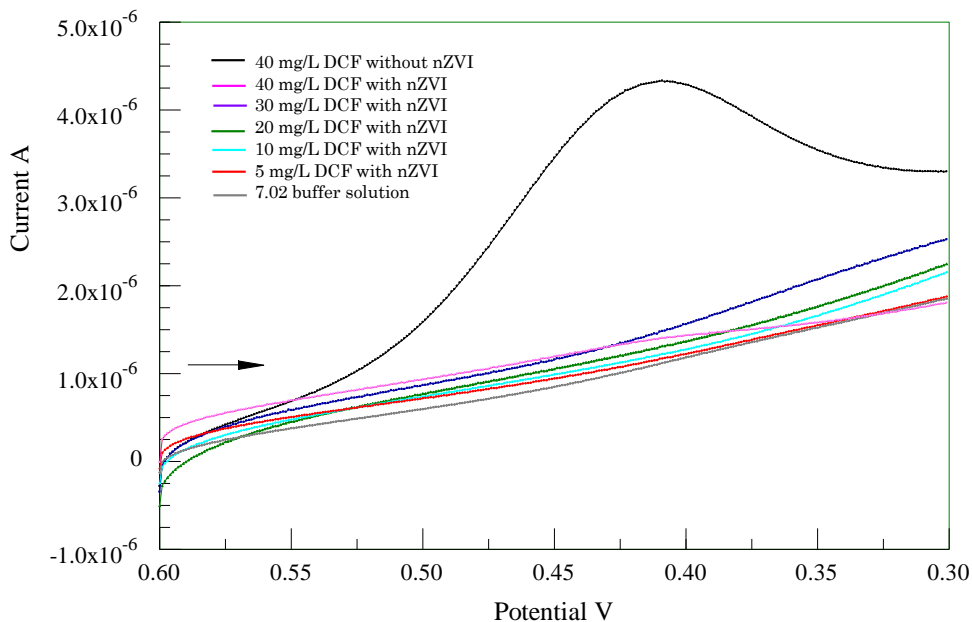


**Figure 37: LSV response of an overlay of different concentrations of DCF after using nZVI in a pH 7.02 in 0.1 M KCl using GCE, surface area ( $0.069 \text{ cm}^2$ ), scan rate of  $300 \text{ mV/s}$  over a potential range of  $0.6$  to  $0.3 \text{ V}$**

A more detailed analysis is shown in Figure 38. The reduction peak was chosen to indicate the relationship between current and concentration. Calibration curves for different DCF concentrations —  $40$ ,  $30$ ,  $20$ ,  $10$ ,  $5$  and  $2.5 \text{ mg/L}$  — were constructed while keeping the nZVI amount the same under  $7.02 \text{ pH}$  value. Figure 38 shows a series of data points generated:  $7.02 \text{ pH}$  buffer solution, DCF solutions prepared in a  $7.02 \text{ pH}$  buffer without nZVI, and DCF solutions prepared in a  $7.02 \text{ pH}$  buffer with nZVI. The slopes of calibration curves presented in Table 5 which represent the process sensitivity.



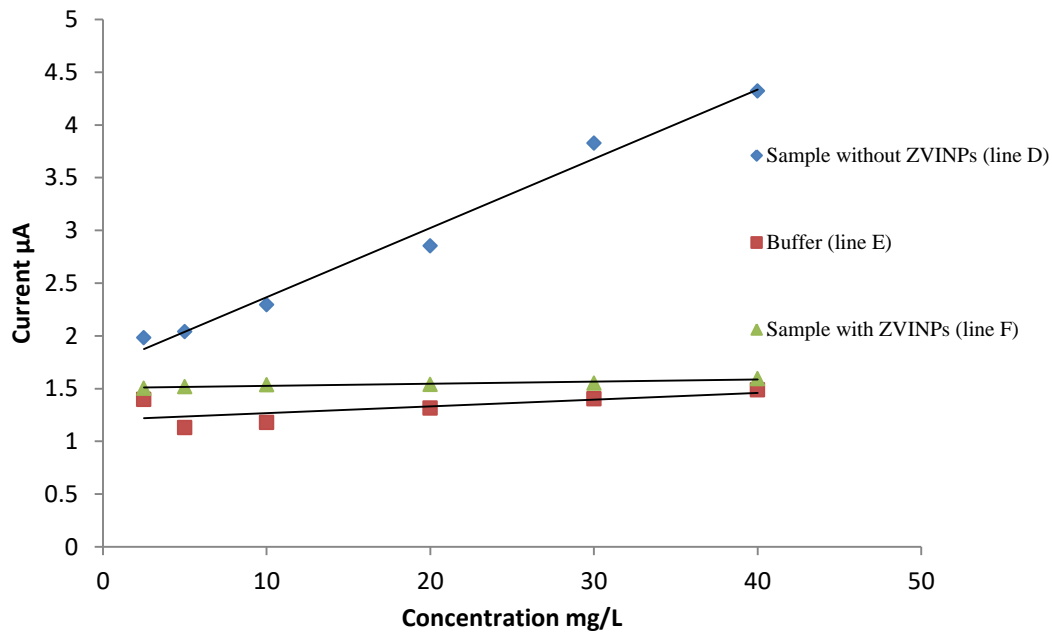


Figure 38: Calibration curve for DCF removal using nZVI in a in a pH 7.02 in 0.1 M KCl using GCE, surface area (0.069 cm<sup>2</sup>), scan rate of 300 mV/s, after 8 minutes, at 0.40V potential.

For nZVI, slope of line F (0.0064 µA/ mg/L) in Table 5 was smaller than for line D (0.0650 µA/ mg/L). The slope values indicate that line D is steeper than line F, meaning that the amount of DCF in water sample has decreased due to adsorption on the nZVI.

**Table 5: Characteristics of calibration curves for DCF removal using IO-NPs and nZVI**

Type of NPs	Type of solution	Line equation	R <sup>2</sup>	Sensitivity
IO-NPs	Blank	$y = 0.0279x + 2.3762$	0.9729	0.02
	40 mg/L DCF sodium without NPs	$y = 0.0579x + 2.3867$	0.9461	0.05
	40 mg/L DCF sodium with NPs	$y = 0.0502x + 2.1625$	0.9717	0.05
nZVI	Blank	$y = 0.002x + 1.5043$	0.9072	0.02
	40 mg/L DCF sodium without NPs	$y = 0.0657x + 1.7107$	0.9860	0.06
	40 mg/L DCF sodium with NPs	$y = 0.0064x + 1.203$	0.4680	0.06

DCF is known of having two Cl groups which might form a repulsion forces between the IO-NPs and DCF drug and inhibited the adsorption and removing process from the aqueous solutions. As a result nZVI were a better option to remove DCF sodium as Table 7 shows.

### 3.5.2 Calibration Curves of MFA

MFA was removed at first by using IO-NPs as can be seen in Figure 39 due to the electrostatic attraction forces and H-bonding between IO-NPs and MFA drug. Peak

current values are determined using CV technique with a scan rate of 0.3 V/s, and the potential was swept from 0.4 V to 1.0 V using GCE Vs Ag/AgCl.

The slopes of calibration lines that interpolate experimental data were used to calculate the sensitivity. Figure 39 shows how oxidation peak current for a 40 mg/L MFA solution decreases as we added IO-NPs. For calibration curve, the oxidation peak at around 0.7 V was chosen to indicate the relationship between current and concentration.

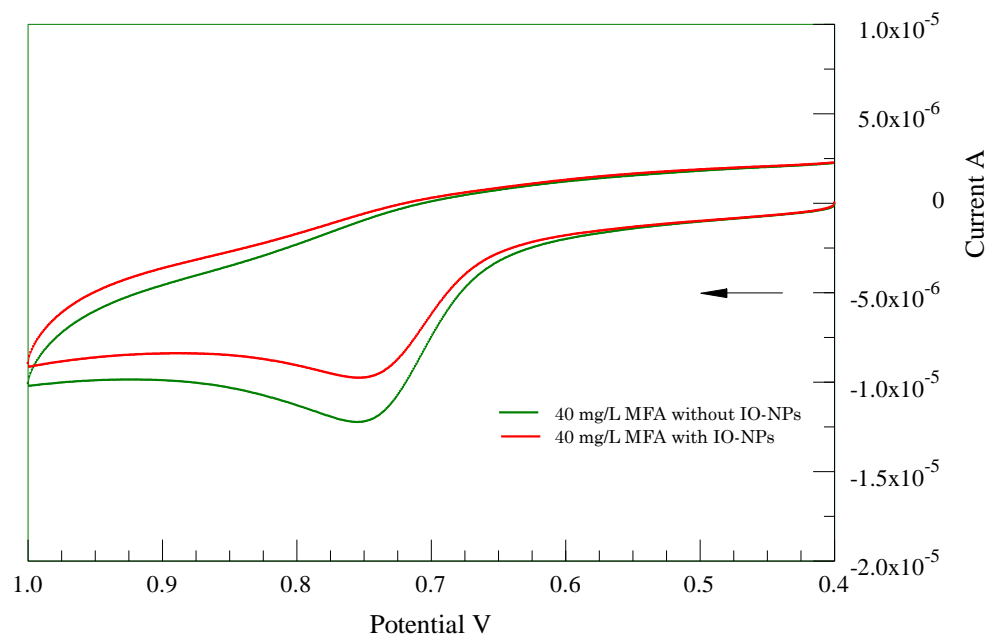


Figure 39: CVs response of 40 mg/L MFA after using nZVI in a pH 7.02 in 0.1 M KCl using GCE, surface area ( $0.069 \text{ cm}^2$ ), scan rate of 300 mV/s over a potential range of 0.6 to 0.3 V with and without IO-NPs

To better show the effect of IO-NPs addition, calibration curves for different MFA concentrations were constructed while keeping the NPs dose (0.08g) and (7.02) pH value the same for all experiments as presented in Figure 40. The calibration Curves in Figure 40 shows a series of data points for the anodic current obtained: 7.02 pH buffer solution serving as a background, MFA solutions prepared in a 7.02 pH buffer without IO-NPs, and MFA solutions prepared in a 7.02 pH buffer with IO-NPs. The slopes of calibration curves were presented in Table 6 which shows improvement in electrochemical removal when the potential was held constant at 0.74V.

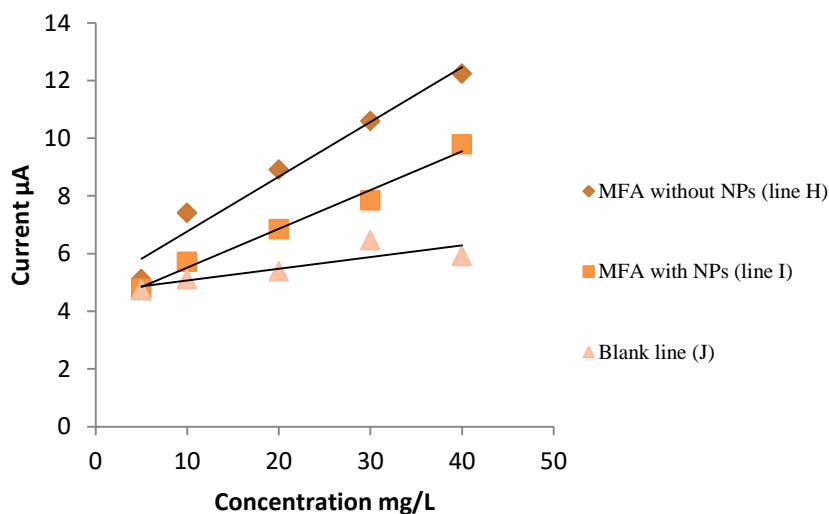
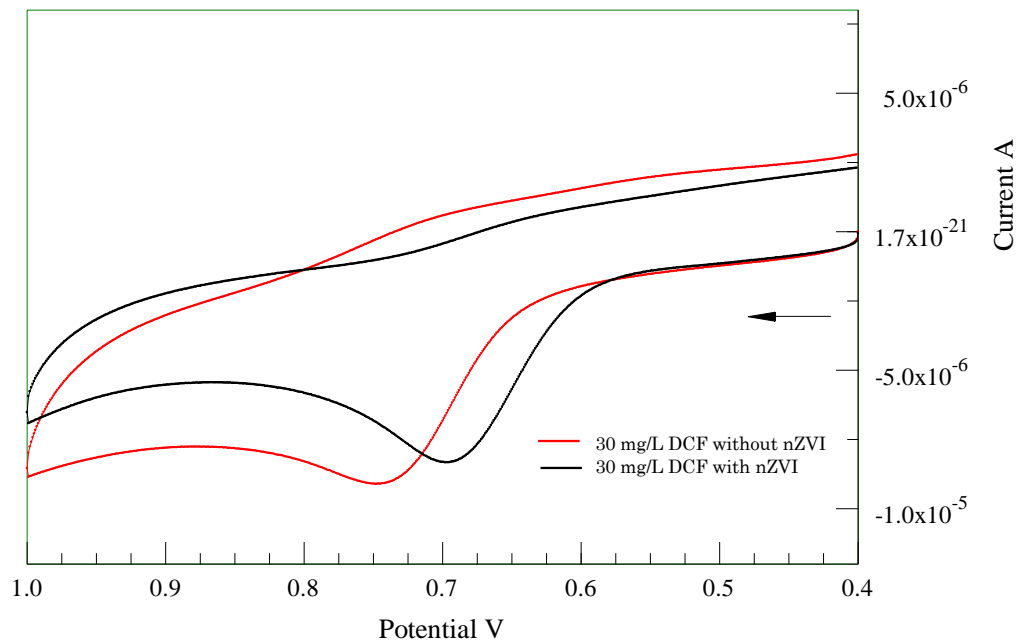


Figure 40: Calibration curve for MFA removal using IO-NPs in a pH 7.02 in 0.1 M KCl using GCE, surface area (0.069 cm<sup>2</sup>), scan rate of 300 mV/s, after 7 minutes, at 0.74V potential, and 10<sup>-5</sup> sensitivity

Slopes for each calibration curve were compared in order to refer to the sensitivity and the removal extent of MFA removal in water samples. The sensitivity from slope magnitude of line I after IO-NPs addition was less than for line H. according to the steeper calibration curve, the amount of MFA removed has increased after IO-NPs addition.

In addition to Figure 40 which demonstrates that IO-NPs do provide a good adsorbent to remove the desired drug, Table 8 includes the removal percentage of MFA from water samples which reached to a magnitude of 20.07 % for a 40 mg/L MFA prepared solution after adding 0.08 g of IO-NPs.

Lastly, MFA removal was tested by using nZVI which was illustrated in Figure 41. An increase in the anodic current peak has appeared around a potential of 0.7 V without nZVI. Meanwhile, after nZVI were added, a shift in the oxidation peak has occurred as CV in Figure 41 shows with a  $\Delta E^{\circ}$  magnitude of -0.04 V. AS a result,  $\Delta G^{\circ}$  was calculated by Nernst equation and found to be +4.72 kJ/mol which indicates that the reaction doesn't favor the products as nZVI were added.



**Figure 41: CV of 30 mg/L MFA in a pH 7.02 in 0.1 M KCl using GCE, surface area ( $0.069 \text{ cm}^2$ ), scan rate of 300 mV/s over a potential range of 0.4 to 1.0 V with and without nZVI**

The anodic peak was chosen to indicate the relationship between current and MFA concentration. Calibration curves for different MFA concentrations — 40, 30, 20, 10, and 5 mg/L — were constructed as seen in Figure 42 while keeping the nZVI dose the same under 7.02 pH value. Figure 42 shows a series of data points generated: 7.02 pH buffer solution, MFA solutions prepared in a 7.02 pH buffer without nZVI, and MFA solutions prepared in a 7.02 pH buffer with nZVI.

The slopes of calibration curves presented in Table 5 which represent the process sensitivity compared for water sample.

It was concluded that removal percentage didn't exceed 5% as represented in Table 8.

This result can also be predicted from the calibration curve slope which was (0.1110  $\mu\text{A}/\text{mg/L}$ ) for line L similar to the slope of line K without NPs (0.1205  $\mu\text{A}/\text{mg/L}$ ) as

Figure 42 shows.

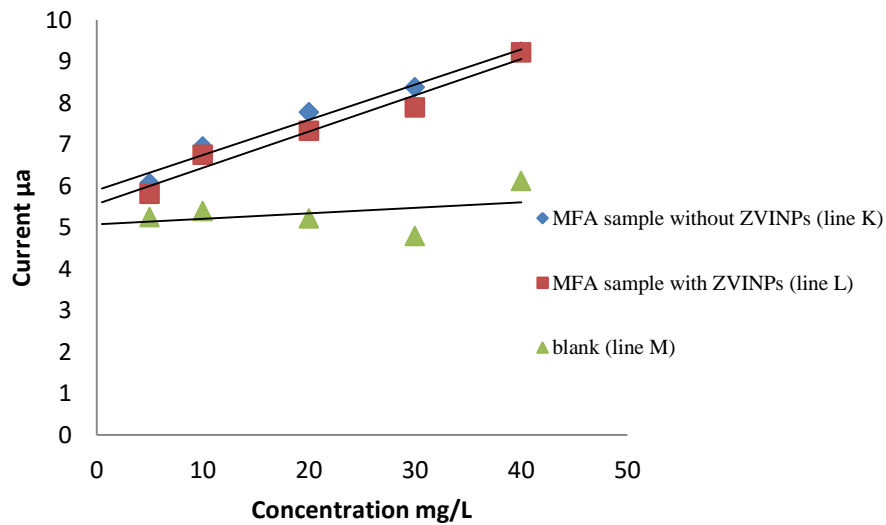


Figure 42: Calibration curve for MFA removal using nZVI after 7 minutes, at 0.71 V potential, and  $10^{-5}$  sensitivity

The main characteristics of the MFA calibration curves are summarized in Table 6 which includes sensitivity, coefficient of determination and the equation line of each calibration curve for MFA removal using IO-NPs and nZVI.

**Table 6: Characteristics of calibration curves for MFA removal using IO-NPs and nZVI**

Type of NPs	Type of solution	Line equation	R <sup>2</sup>	Sensitivity
IO-NPs	Blank	$y = 0.0407x + 4.6611$	0.7294	0.04
	40 mg/L MFA without NPs	$y = 0.1898x + 4.8686$	0.9664	0.18
	40 mg/L MFA with NPs	$y = 0.1345x + 4.1702$	0.9849	0.13
nZVI	Blank	$y = 0.0062x + 5.2771$	0.0472	0.00
	40 mg/L MFA without NPs	$y = 0.1205x + 4.605$	0.8394	0.12
	40 mg/L MFA with NPs	$y = 0.111x + 5.1419$	0.8778	0.11

For Table 6, R<sup>2</sup> value was found to be greater for IO-NPs than nZVI. This means that the data points are more scattered for nZVI. It also shows that the regression line fits the data more for IO-NPs.



### 3.6 Percentage Removal of Pharmaceuticals Using NPs

#### 3.6.1 Percentage removal of DCF using nZVI and IO-NPs

In general, removal efficiency percentage is a percentage representation of the removal efficiency for a specific pollutant or contaminant parameter across a water treatment facility; it can be measured by comparing influent and effluent concentrations over time. From current values on the Y axis in calibration curves, we can define the removal percentage which can be found in Table 7. Removal efficiency of DCF was determined according to Equation 8 (M. Al-Jabari et al. 2018).

$$R(\%) = \frac{C_0 - C_t}{C_0} \times 100\% \dots\dots(8)$$

Where  $C_0$  is the pharmaceuticals' concentration in a solution without NPs, and  $C_t$  is the pharmaceuticals' concentration in a solution with NPs after 8 minutes of 0.08g of NPs addition.

**Table 7: Calculated removal efficiency percentages of DCF using 0.08 g from both nZVI and IO-NPs**

Nanoparticles	Read at	Removal	Removal	Removal	Removal	Removal	Removal
	Potential	%	%	%	%	%	%
	V	40 mg/L	30 mg/L	20 mg/L	10 mg/L	5 mg/L	2.5 mg/L
<b>Iron zero</b>	0.41	65.54	63.37	53.92	48.73	44.60	29.51
<b>Iron oxide</b>	0.41	9.10	14.32	10.38	10.93	7.58	4.32

On one hand, the data in Figure 43 clearly shows that DCF removal percentage increases significantly with using nZVI as concentrations increases indicating a promising method to remove DCF drug from wastewater samples. On the other hand, IO-NPS were able to remove DCF up to a certain point which was lower than the one obtained using nZVI.

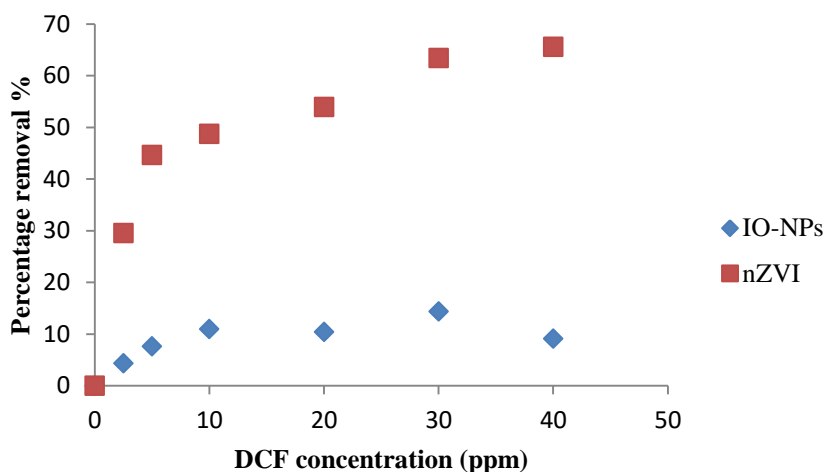


**Figure 43: DCF concentration Vs removal percentage efficiency using 0.08 g of nZVI and IO-NPs after 8 minutes**

### 3.6.2 Percentage Removal of MFA using nZVI and IO-NPs

Equation 8 was also used for MFA removal percentage calculations which are presented in Table 8. A difference between nZVI and IO-NPs is shown as the removal percentage increases with IO-NPs due to stronger electrostatic interactions rather than with nZVI.

**Table 8: Calculated removal efficiency percentages removal of MFA using 0.08 g from each of nZVI and IO-NPs**

<b>Nanoparticles</b>	<b>Read at</b>	<b>Removal</b>	<b>Removal</b>	<b>Removal</b>	<b>Removal</b>	<b>Removal</b>
	<b>Potential</b>	<b>%</b>	<b>%</b>	<b>%</b>	<b>%</b>	<b>%</b>
	<b>V</b>	<b>40 mg/L</b>	<b>30 mg/L</b>	<b>20 mg/L</b>	<b>10 mg/L</b>	<b>5 mg/L</b>
<b>Iron zero</b>	0.71	0.18	5.85	5.72	2.93	4.14
<b>Iron oxide</b>	0.74	20.07	25.92	23.13	22.94	6.47

Current was measured in CVs at a fixed potential for nZVI at around 0.71 for all MFA concentrations after 7 minutes. On the other hand, current was read at 0.74 after IO-NPs addition in MFA samples.

The data in Figure 44 clearly shows that MFA removal percentage increases as concentrations increases indicating a promising method to remove MFA drug from wastewater samples by using IO-NPs. nZVI were not able to provide a percentage removal higher than 5% in all concentrations unlike IO-NPs which was able to remove almost 25% in a 30 mg/L MFA sample.

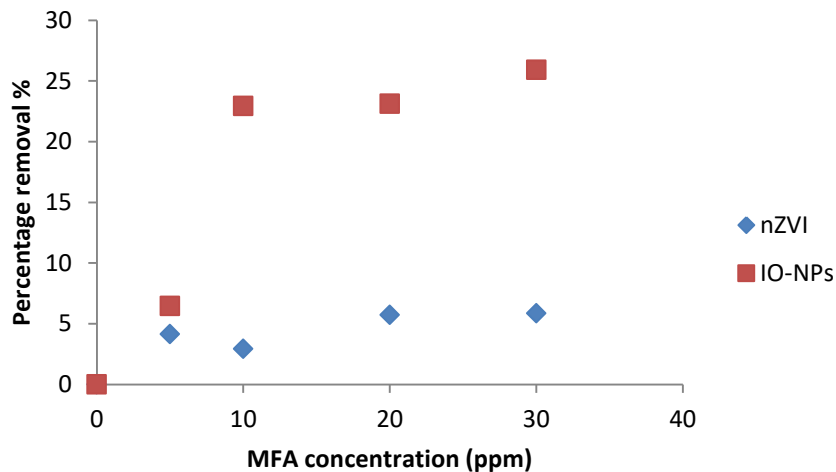


Figure 44: MFA concentration Vs percentage efficiency removal using nZVI and IO-NPs

### 3.7 Drug Adsorption

As indicated by the presented results in general, it seems like the removal process takes place due to different interactions between MFA and NPs (nZVI and IO-NPs). The predicted reasons for the removal are likely due electrostatic interactions including ion dipole interaction, dipole-dipole, and H bonding, as presented in Scheme 4 and 6.

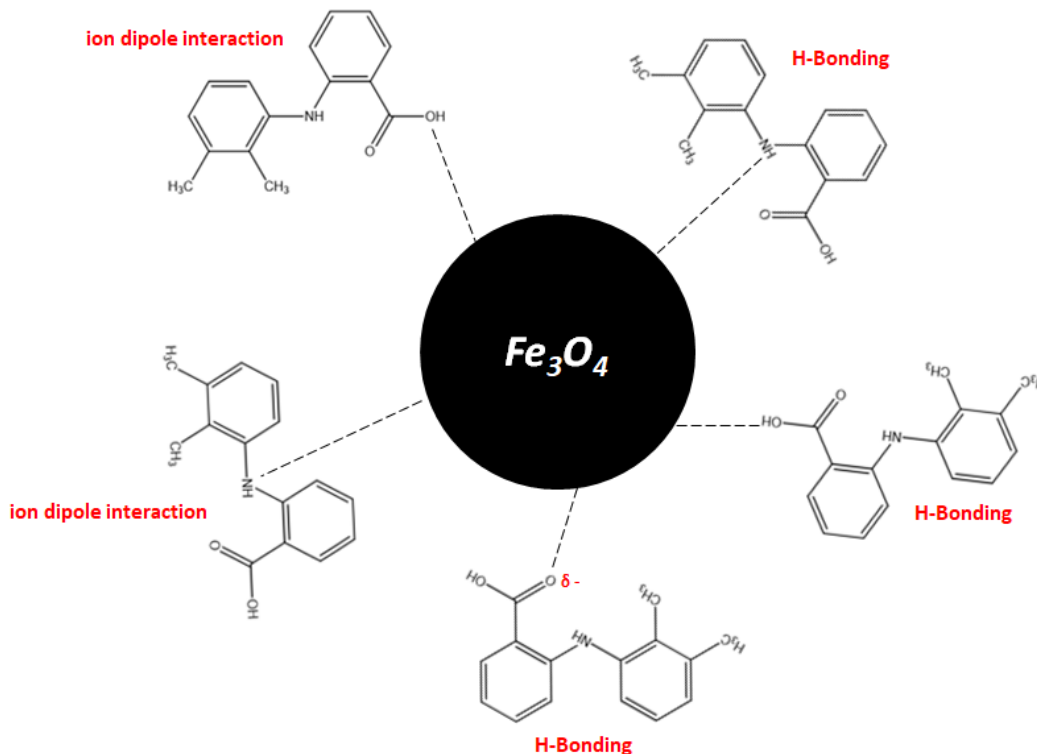
Intermolecular forces (electrostatic interactions) are often weaker than covalent bonds. At 100°C, it takes 927 kJ to break both O-H bonds in 1mol of H<sub>2</sub>O and overcome intramolecular forces, but only 41 kJ to transform 1 mol of water into vapor and overcome intermolecular forces (B. B. Sharma and Rajan 2022). The combination of both attracting and repulsive components makes up these intermolecular interactions. Dipole-dipole interaction is the physical interaction

between two dipolar molecules. One of the molecules' partially negative portions is attracted to the partially positive portion of another polar molecule. Hydrogen bonding is a strong dipole-dipole type of interaction. Bonds of this sort are stronger than dipole-dipole interactions, but not as strong as covalent and ionic bonds. Molecules must contain hydrogen connected to a highly electronegative atom (F, O, and N) and a lone pair of electrons on a tiny highly electronegative atom for hydrogen bonding to occur.

The net surface charge of MFA can be indicated using zeta potential analyzer and found to be zero at pH 7 in phosphate buffer solution. This implies that the adsorption mechanism of MFA wasn't a result of electrostatic interaction. Meanwhile, deprotonated MFA which holds a negative charge can be adsorbed on the NPs surface due to electrostatic interactions under basic media (Sompornpailin et al. 2020).

Nanoparticles have numerous properties due to their high surface area and strong interactions with pharmaceuticals to help with their removal. MFA has a carboxylic group which has a high affinity for metallic oxides NPs, As a result of the positive charge on iron (IV) and negative charge on MFA from carboxylic group under basic media (S. Yu and Chow 2004). The adsorption of MFA is promoted by the electrostatic interaction between the negatively charged molecule and the positively charged iron (IV) as can be seen in Scheme 4. It could also partially be attributed by the electrostatic interaction which can be promoted by the terminal  $-OH/O^-$  and the

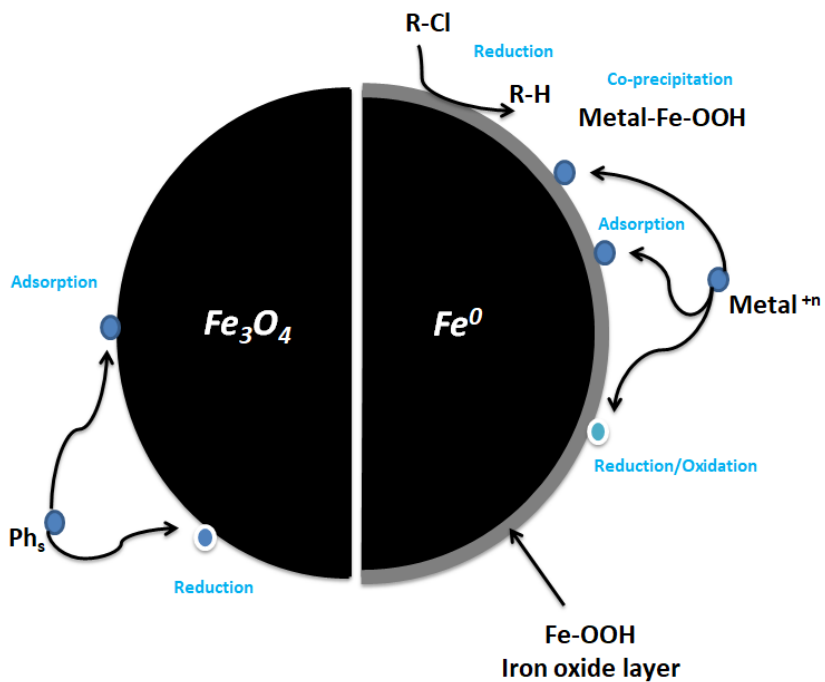
positively amine group  $-\text{NH}_2$ . Another reason of the numerous interactions might come from the hydrogen bonding with hydroxyl groups on metal oxide surface (Sompornpailin et al. 2020).



**Scheme 4: IO-NPs -Mefenamic possible interaction model under acidic media**

In essence,  $\text{Fe}^0$  provides reducing capacity which is presented in Scheme 5, while the ferric oxide shell provides reactive and electrostatic interaction sites with heavy metals according to the standard potential  $E^0$  which is mainly composed of reduction and sorption (J. Yang et al. 2019). Furthermore, the particle size of nZVI may be controlled, and the surface has a lot of reactive sites. The better efficacy of nZVI in

eliminating heavy metals from wastewater is due to its high reduction capacity and wide specific surface area as seen in Scheme 5 (Kharisov et al. 2014).



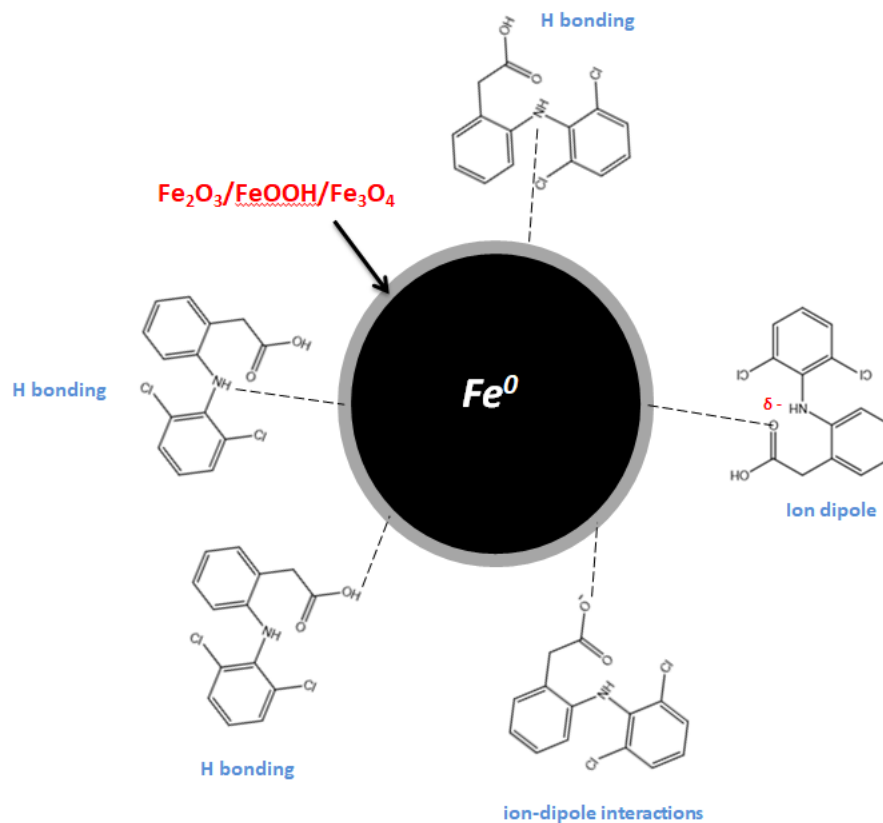
Scheme 5: Magnetic nanoparticles schematic model (nZVI, and  $\text{Fe}_3\text{O}_4$ ).

For nZVI, there were limited studies on using these nanoparticles alone for removing pharmaceuticals in water (Liu et al. 2019). Oxidation of nZVI is very common where these nanoparticles undergo oxidation by oxidants like water or dissolved oxygen in the atmosphere (Sravanthi, Ayodhya, and Yadgiri Swamy 2018). As nZVI corrode in natural water (pH 4-9), producing hydrated iron oxide  $\text{Fe}_2\text{O}_3 \cdot x\text{H}_2\text{O}$ ,  $\text{FeOOH}$ , and  $\text{Fe}_3\text{O}_4$  on the metal surface which form stronger interactions with different groups such as  $-\text{NH}-$ ,  $=\text{O}$ ,  $-\text{COOH}$ , and N of the targeted pharmaceuticals through H bonding

which improves the removal process by nZVI as presented in Scheme 6 (Rubio-Retama et al. 2010). In this research, the anionic DCF molecules can develop ion-dipole interactions with the polar –OH groups on the nZVI (Punyapalakul et al. 2013).

Scheme 6 shows the possible interactions between nZVI and DCF drug. DCF molecules have functional groups like carboxylate or NH group, they can be physisorbed at the nZVI surface in aqueous media: the functional groups interact with the protonated or deprotonated OH groups on the surface of the NPs through electrostatic interactions. Molecules, on the other hand, can react with the NP surface's –OH groups either by H-bonding or ion-dipole interactions (Cotin et al. 2018). The –OH groups on the surface are amphoteric, and the surface charge may be altered by adjusting the pH. The surface of the iron oxide NPs can thus be positively or negatively charged depending on the pH of the solution. The pH at which the surface has equal numbers of positive and negative charges is known as the isoelectric point (IEP). The NPs are positively charged at acidic pH and negatively charged at basic pH.





**Scheme 6: nZVI–DCF possible interaction model at acidic and basic media**

Another study described in Figure 45 has showed that adsorption is affected by the attraction force either between the free electron pair of the  $\pi$  electrons in the DCF two phenyl rings and the vacant orbitals of NPs or between nitrogen and oxygen (heterogeneous atoms) with the vacant orbitals of nZVI by physical interactions (AL-abbassi et al. 2020).

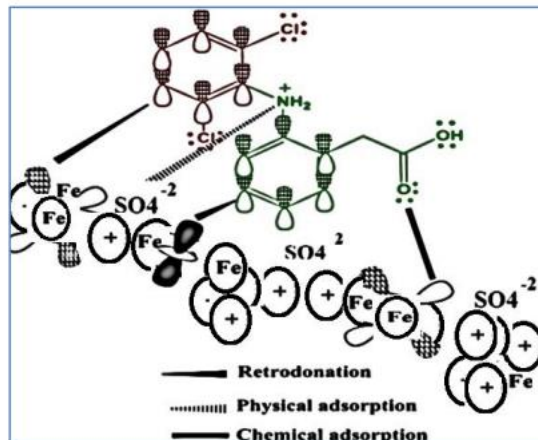


**Figure 45: Adsorption mechanism of DCF drug on iron particles (AL-abbassi et al. 2020)**

The energy of the highest occupied molecular orbital (HOMO) of DCF has been stated to be high (-4.695 eV) which mainly shows that DCF has the ability to attack another electrophile and donate electrons to other molecules/particles which have empty orbitals as can be seen in Figure 46.

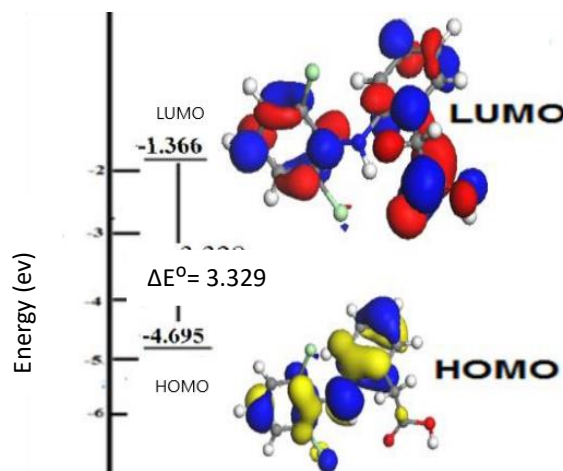


**Figure 46: A computer- optimized DCF drug that constructs HOMO & LUMO orbits (AL-abbassi et al. 2020)**

The energy gap between HOMO and lowest occupied molecular orbital (LUMO) in Figure 46 describes the reactivity of drugs such as DCF on metal surfaces. Therefore, larger the energy gap the weaker the bonds (AL-abbassi et al. 2020).

One thing that should be taken into consideration is that soft acids (more electrons, more polarizable, and larger size) tend to react with soft bases (soft-soft combination) and hard acids (larger nuclear charge and smaller size) form stronger interactions with hard bases (hard-hard combination). Furthermore, MFA is known with having a COOH group which is considered to be a hard acid and prefers bonding with iron of a 4 oxidation state. This hypothesis can also assess which NP has a stronger interaction with the pharmaceuticals used (MFA and DCF).

## Chapter Four: Conclusion

---

### 4. Conclusion

The main aim of this study was to assess the pharmaceuticals' removal in aqueous solutions using electrochemical techniques. The investigation was tested towards MFA and DCF in the presence of two types of NPs (IO-NPs and nZVI). Glassy carbon electrode showed a great potential in detecting both drugs with a high sensitivity.

Firstly, the study involved different electrochemical techniques at relatively low concentrations of DCF and MFA in the presence of NPs. Then, a comparison of the results obtained has been performed using two types of working electrodes; glassy carbon electrode and gold working electrode. The detection limit of GCE was higher than Au electrode and gave more promise on detection the concentration of MFA and DCF.

Secondly, IO-NPs and nZVI were used in order to adsorb pharmaceuticals from water samples. Removal was obtained for both drugs and both NPs. Afterwards, different parameters were studied including NPs dose, contact time, scan rate, pH, and temperature in order to find the optimum conditions for the highest removal percentage. For DCF, the highest percentage was obtained by using nZVI at room temperature under acidic media immediately. On the other hand, MFA was removed

after 7 minutes at room temperature by using IO-NPs. The variation in removal efficiency was calculated and extent of the reaction was obtained for the removal process.

Finally, explanations were offered to support the obtained data in this research.

## Chapter Five: Future Studies and Recommendations

---

### 5. Recommendations:

#### *For studying MFA removal:*

1. The first stage would be investigating the usage of other types of NPs other than IO-NPs such as silica nanoparticles for a higher percentage removal due to their high melting point, stability, low toxicity, and great intrinsic reactive sites.
2. Next stage would be investigating the removal process using different types of working electrodes mainly pencil graphite. The graphite electrode is made up of 65% graphite. The presence of  $sp^2$  hybridized carbon provides various unique qualities, including excellent adsorption, electrical conductivity, and a low background current (David et al. 2022).
3. Further research needs to investigate the mechanism of pharmaceuticals' removal by DigiSim® for CV scans in order to observe changes in speed of reaction due to NPs addition.
4. Scale up the removal process by performing a series of columns to separate pharmaceuticals from water samples by the adsorption on the NPs surface.

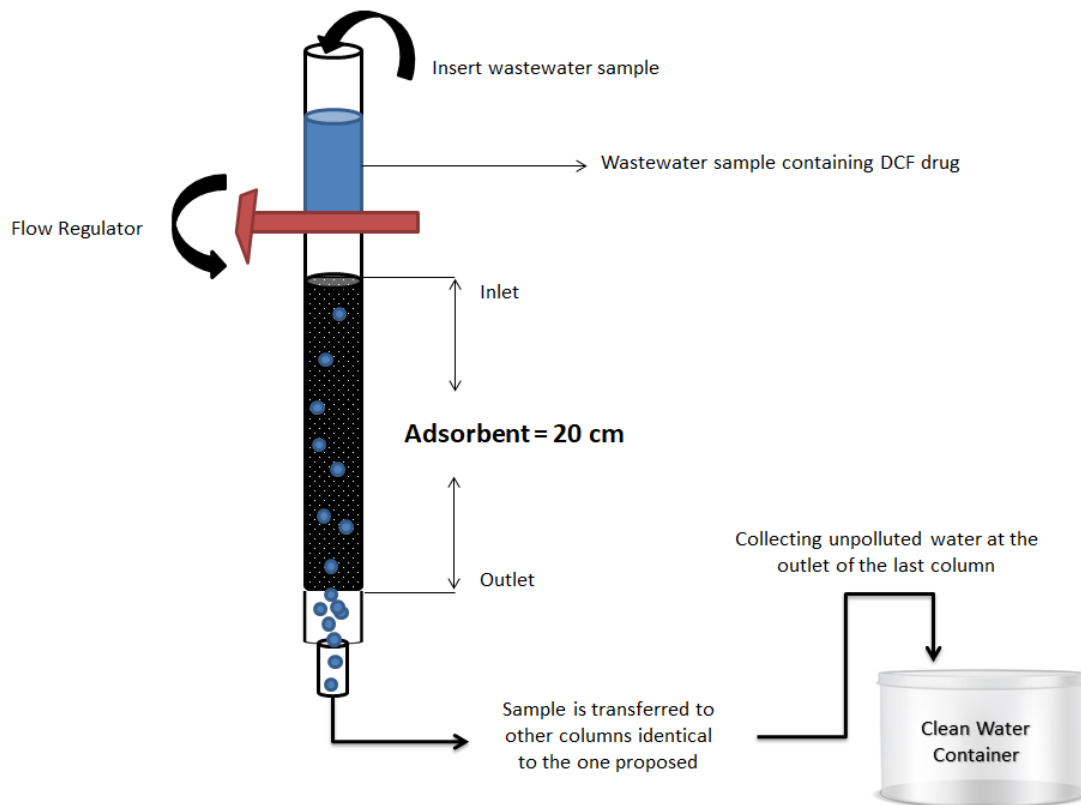
***For studying DCF removal:***

1. Initially, a further Research needs to investigate the mechanism of using nZVI in this study to remove DCF drug by DigiSim® for CV scans in order to observe changes in speed of reaction due to NPs addition.
2. Test the sensor's selectivity by using two different chemicals and efficiently separate them by the adsorption of only one on the NPs surface depending on the electrostatic interactions strength while keeping the other one in the water sample.
3. The following stage would focus on investigating real concentrations of DCF in wastewater, and use the NPs to remove them.
4. Wastewater recycling and reuse might be a viable option for unpolluted water sources, as well as a potential solution to water shortage in Palestine. Therefore, the last stage would mainly focus on scaling up the removal process by performing a station to expand the scale by building series of columns filled with nZVI where wastewater can go through it in order to remove the desired contaminants.

***Adsorption investigations in continuous mode***

The adsorbent will be placed within a glass column and utilized for DCF adsorption and removal from wastewater samples. Scheme 7 shows a schematic depiction of a proposed glass column.

The glass column will be about 20 cm in length and 2 cm in diameter. A given amount of nZVI will be placed into a glass column, and wastewater sample will be allowed to flow through it at a certain pace. The concentration of DCF will be measured before and after treatment with a CHI760 instrument.



**Scheme 7: Proposed small experimental station of nZVI adsorbent packed inside a glass column**



## **Bibliography**

Adeyeye, Christianah M., and Pui Kai Li. 1990. "Diclofenac Sodium." *Analytical Profiles of Drug Substances and Excipients* 19 (C): 123–44.

[https://doi.org/10.1016/S0099-5428\(08\)60366-4](https://doi.org/10.1016/S0099-5428(08)60366-4).

Ahmad, Tokeer, Ruby Phul, and Huma Khan. 2019. "Iron Oxide Nanoparticles: An Efficient Nano-Catalyst." *Current Organic Chemistry*.

<https://doi.org/10.2174/1385272823666190314153208>.

AL-abbassi, Aisha, Gehan

Tafiler:///C:/Users/User/Desktop/everything/university/inorganic/inorganic book.pdfher, Emdallah Matrood, Abdulrahman Dnkm, Akram Sallh, Raga Izrik, and Mohammed Suliman. 2020. "Study of the Behavior of Sodium Diclofenac Expired Drug as an Corrosion Inhibitor of Iron in Sulfuric Acid Using UV-VIS Spectrophotometry." *International Journal of Scientific Research in Science, Engineering and Technology*, no. March: 233–42.

<https://doi.org/10.32628/ijrsrset207248>.

Al-Jabari, Mohammed H., S. Sulaiman, Shahid Ali, Reem Barakat, Asem Mubarak, and Safyan Akram Khan. 2019. "Adsorption Study of Levofloxacin on Reusable Magnetic Nanoparticles: Kinetics and Antibacterial Activity." *Journal of Molecular Liquids* 291: 111249. <https://doi.org/10.1016/j.molliq.2019.111249>.

- Al-Jabari, Mohammed, Imtiaz Khalid, Saleh Sulaiman, Israa Alawi, and Jameleh Shilo. 2018. "Synthesis, Characterization, Kinetic and Thermodynamic Investigation of Silica Nanoparticles and Their Application in Mefenamic Acid Removal from Aqueous Solution." *Desalination and Water Treatment* 129 (January): 160–67. <https://doi.org/10.5004/dwt.2018.23083>.
- Al-Kindi, Ghayda Y., Faris H. Al Ani, Noor Kh Al-Bidri, and Husam A. Alhaidri. 2021. "Diclofenac Removal from Wastewater by Activated Carbon." *IOP Conference Series: Earth and Environmental Science* 779 (1). <https://doi.org/10.1088/1755-1315/779/1/012091>.
- Ali, Attarad, Hira Zafar, Muhammad Zia, Ihsan ul Haq, Abdul Rehman Phull, Joham Sarfraz Ali, and Altaf Hussain. 2016. "Synthesis, Characterization, Applications, and Challenges of Iron Oxide Nanoparticles." *Nanotechnology, Science and Applications*. Dove Medical Press Ltd. <https://doi.org/10.2147/NSA.S99986>.
- Aragaw, Tadele Assefa, Fekadu Mazengiaw Bogale, and Belete Asefa Aragaw. 2021. "Iron-Based Nanoparticles in Wastewater Treatment: A Review on Synthesis Methods, Applications, and Removal Mechanisms." *Journal of Saudi Chemical Society* 25 (8): 101280. <https://doi.org/10.1016/J.JSCS.2021.101280>.
- Baalousha, M., J. R. Lead, and Y. Ju-Nam. 2011. "Natural Colloids and Manufactured Nanoparticles in Aquatic and Terrestrial Systems." *Treatise on Water Science* 3 (January): 89–129. <https://doi.org/10.1016/B978-0-444-53199->

5.00053-1.

- Bakr, A. A., N. A. Sayed, T. M. Salama, I. Othman Ali, R. R. Abdel Gayed, and N. A. Negm. 2018. "Potential of Mg–Zn–Al Layered Double Hydroxide (LDH)/Montmorillonite Nanocomposite in Remediation of Wastewater Containing Manganese Ions." *Research on Chemical Intermediates* 44 (1): 389–405. <https://doi.org/10.1007/s11164-017-3110-5>.
- Bard, Allen J, and Larry R Faulkner. 2001. *Electrochemical Methods - Fundamentals and Applications. Electrochemical Methods - Fundamentals and Applications*.
- Beiraghi, Asadollah, Kamyar Pourghazi, Mitra Amoli-Diva, and Akbar Razmara. 2014. "Magnetic Solid Phase Extraction of Mefenamic Acid from Biological Samples Based on the Formation of Mixed Hemimicelle Aggregates on Fe<sub>3</sub>O<sub>4</sub> Nanoparticles Prior to Its HPLC-UV Detection." *Journal of Chromatography B: Analytical Technologies in the Biomedical and Life Sciences* 945–946: 46–52. <https://doi.org/10.1016/j.jchromb.2013.11.039>.
- Biotechnology. 2022a. "PubChem Compound Summary for CID 5018304, Diclofenac Sodium." 2022. <https://pubchem.ncbi.nlm.nih.gov/compound/Diclofenac-sodium>.
- Biotechnology, National Center for. 2022b. "PubChem Compound Summary for CID 4044, Mefenamic Acid." 2022. <https://pubchem.ncbi.nlm.nih.gov/compound/Mefenamic-acid>.

- Bukkitgar, Shikandar D., Nagaraj P. Shetti, Raviraj M. Kulkarni, Kakarla Raghava Reddy, Shyam S. Shukla, Viswanathan S. Saji, and Tejraj M. Aminabhavi. 2019. "Electro-Catalytic Behavior of Mg-Doped ZnO Nano-Flakes for Oxidation of Anti-Inflammatory Drug." *Journal of The Electrochemical Society* 166 (9): B3072–78. <https://doi.org/10.1149/2.0131909jes>.
- Bukkitgar, Shikandar D., Nagaraj P. Shetti, Raviraj M. Kulkarni, and Mohammed Wasim. 2018. "Electrochemical Behavior of Mefenamic Acid at Zinc Oxide Nanoparticles Modified Carbon Paste Electrode." *Materials Today: Proceedings* 5 (10): 21458–65. <https://doi.org/10.1016/j.matpr.2018.06.555>.
- Bukkitgar, Shikandar D., Nagaraj P. Shetti, Deepti S. Nayak, Gangadhar B. Bagehalli, and Sharanappa T. Nandibewoor. 2014. "Electrochemical Sensor for the Detection of Mefenamic Acid in Pharmaceutical Sample and Human Urine at Glassy Carbon Electrode." *Der Pharma Chemica* 6 (2): 258–68.
- Carmo, Marcelo, David L. Fritz, Jürgen Mergel, and Detlef Stolten. 2013. "A Comprehensive Review on PEM Water Electrolysis." *International Journal of Hydrogen Energy* 38 (12): 4901–34. <https://doi.org/10.1016/j.ijhydene.2013.01.151>.
- Colombo, Renata, Tanare C.R. Ferreira, Renato A. Ferreira, and Marcos R.V. Lanza. 2016. "Removal of Mefenamic Acid from Aqueous Solutions by Oxidative Process: Optimization through Experimental Design and HPLC/UV Analysis."

*Journal of Environmental Management* 167: 206–13.

<https://doi.org/10.1016/j.jenvman.2015.11.029>.

Cotin, G., S. Piant, D. Mertz, D. Felder-Flesch, and S. Begin-Colin. 2018. “Iron Oxide Nanoparticles for Biomedical Applications: Synthesis, Functionalization, and Application.” *Iron Oxide Nanoparticles for Biomedical Applications*, January, 43–88. <https://doi.org/10.1016/B978-0-08-101925-2.00002-4>.

Crini, Grégorio, and Eric Lichtfouse. 2019. “Advantages and Disadvantages of Techniques Used for Wastewater Treatment.” *Environmental Chemistry Letters* 17 (1): 145–55. <https://doi.org/10.1007/s10311-018-0785-9>.

Dadfar, Seyed Mohammadali, Karolin Roemhild, Natascha I. Drude, Saskia von Stillfried, Ruth Knüchel, Fabian Kiessling, and Twan Lammers. 2019. “Iron Oxide Nanoparticles: Diagnostic, Therapeutic and Theranostic Applications.” *Advanced Drug Delivery Reviews*. <https://doi.org/10.1016/j.addr.2019.01.005>.

David, Iulia Gabriela, Mihaela Buleandra, Dana Elena Popa, Mihaela Carmen Cheregi, Vasile David, Emilia Elena Iorgulescu, and Georgiana Oana Tartareanu. 2022. “Recent Developments in Voltammetric Analysis of Pharmaceuticals Using Disposable Pencil Graphite Electrodes.” *Processes* 10 (3): 1–29. <https://doi.org/10.3390/pr10030472>.

Dolatabadi, Maryam, Saeid Ahmadzadeh, and Mohammad T. Ghaneian. 2020. “Mineralization of Mefenamic Acid from Hospital Wastewater Using Electro-

Fenton Degradation: Optimization and Identification of Removal Mechanism Issues.” *Environmental Progress and Sustainable Energy* 39 (3): 0–1.  
<https://doi.org/10.1002/ep.13380>.

Doménech-Carbó, Antonio, Leandro Machado De Carvalho, Mariele Martini, Drochss P. Valencia, and Gerardo Cebrián-Torrejón. 2015. *Electrochemical Monitoring of the Pharmacological Activity of Natural Products. Studies in Natural Products Chemistry*. Vol. 45. Elsevier. <https://doi.org/10.1016/B978-0-444-63473-3.00003-4>.

Eljamal, Ramadan, Osama Eljamal, Ahmed M.E. Khalil, Bidyut Baran Saha, and Nobuhiro Matsunaga. 2018. “Improvement of the Chemical Synthesis Efficiency of Nano-Scale Zero-Valent Iron Particles.” *Journal of Environmental Chemical Engineering* 6 (4): 4727–35. <https://doi.org/10.1016/j.jece.2018.06.069>.

Farghaly, O. A., R. S. Abdel Hameed, and Abd Alhakeem H. Abu-Nawwas. 2014. “Electrochemical Analysis Techniques: A Review on Recent Pharmaceutical Applications.” *International Journal of Pharmaceutical Sciences Review and Research* 25 (2): 37–45.

Feier, Bogdan, Anca Florea, Cecilia Cristea, and Robert Săndulescu. 2018. “Electrochemical Detection and Removal of Pharmaceuticals in Waste Waters.” *Current Opinion in Electrochemistry* 11: 1–11.  
<https://doi.org/10.1016/j.coelec.2018.06.012>.

- Galdames, Alazne, Leire Ruiz-Rubio, Maider Orueta, Miguel Sánchez-Aralluz, and José Luis Vilas-Vilela. 2020. "Zero-Valent Iron Nanoparticles for Soil and Groundwater Remediation." *International Journal of Environmental Research and Public Health* 17 (16): 1–23. <https://doi.org/10.3390/ijerph17165817>.
- Genuzio, F, A Sala, Th Schmidt, D Menzel, and H Freund. 2016. "Surface Science Phase Transformations in Thin Iron Oxide Films : Spectromicroscopic Study of Velocity and Shape of the Reaction Fronts ☆." *Surface Science* 648: 177–87. <https://doi.org/10.1016/j.susc.2015.11.016>.
- Gupta, Vinod K., Rajeev Jain, Keisham Radhapyari, Nimisha Jadon, and Shilpi Agarwal. 2011. "Voltammetric Techniques for the Assay of Pharmaceuticals-A Review." *Analytical Biochemistry* 408 (2): 179–96. <https://doi.org/10.1016/j.ab.2010.09.027>.
- Guzmán-Hernández, D. S., M. M. Cid-Cerón, M. Romero-Romo, M. T. Ramírez-Silva, M. E. Páez-Hernández, S. Corona-Avenidaño, and M. Palomar-Pardavé. 2017. "Taking Advantage of CTAB Micelles for the Simultaneous Electrochemical Quantification of Diclofenac and Acetaminophen in Aqueous Media." *RSC Advances* 7 (64): 40401–10. <https://doi.org/10.1039/c7ra07269d>.
- Heim, Carolin, Mohamad Rajab, Giorgia Greco, Sylvia Grosse, Jörg E. Drewes, Thomas Letzel, and Brigitte Helmreich. 2020. "Fate of Diclofenac and Its Transformation and Inorganic By-Products in Different Water Matrices during



Electrochemical Advanced Oxidation Process Using a Boron-Doped Diamond Electrode.” *Water (Switzerland)* 12 (6). <https://doi.org/10.3390/W12061686>.

Iriarte-Mesa, Claudia, Yeisy C. López, Yasser Matos-Peralta, Karen de la Vega-Hernández, and Manuel Antuch. 2020. *Gold, Silver and Iron Oxide Nanoparticles: Synthesis and Bionanoconjugation Strategies Aimed at Electrochemical Applications. Topics in Current Chemistry*. Vol. 378. Springer International Publishing. <https://doi.org/10.1007/s41061-019-0275-y>.

Jin, Wei, and Govindhan Maduraiveeran. 2017. “Electrochemical Detection of Chemical Pollutants Based on Gold Nanomaterials.” *Trends in Environmental Analytical Chemistry* 14 (April): 28–36.  
<https://doi.org/10.1016/j.teac.2017.05.001>.

Jonoush, Zohreh Akbari, Abbas Rezaee, and Ali Ghaffarinejad. 2020. “Electrocatalytic Nitrate Reduction Using Fe<sup>0</sup>/Fe<sub>3</sub>O<sub>4</sub> Nanoparticles Immobilized on Nickel Foam: Selectivity and Energy Consumption Studies.” *Journal of Cleaner Production* 242: 118569.  
<https://doi.org/10.1016/j.jclepro.2019.118569>.

Kan, Xianwen, Zhirong Geng, Yao Zhao, Zhilin Wang, and Jun Jie Zhu. 2009. “Magnetic Molecularly Imprinted Polymer for Aspirin Recognition and Controlled Release.” *Nanotechnology* 20 (16). <https://doi.org/10.1088/0957-4484/20/16/165601>.

- Kedarnath., C.H. SwathiC.V.S. SubrahmanyamS.A. Satheshbabu Puvvadi. 2011.  
“Solubilization of Mefanamic Acid.”
- Kharisov, Boris I., H. V.Rasika Dias, Oxana V. Kharissova, Alejandro Vázquez,  
Yolanda Peña, and Idalia Gómez. 2014. “Solubilization, Dispersion and  
Stabilization of Magnetic Nanoparticles in Water and Non-Aqueous Solvents:  
Recent Trends.” *RSC Advances* 4 (85): 45354–81.  
<https://doi.org/10.1039/c4ra06902a>.
- Kincl, Maja, Marija Meleh, Marjan Veber, and Franc Vrečer. 2004. “Study of  
Physicochemical Parameters Affecting the Release of Diclofenac Sodium from  
Lipophilic Matrix Tablets.” *Acta Chimica Slovenica* 51 (3): 409–25.
- Koul, Bhupendra, Anil Kumar Poonia, Dhananjay Yadav, and Jun O. Jin. 2021.  
“Microbe-Mediated Biosynthesis of Nanoparticles: Applications and Future  
Prospects.” *Biomolecules* 11 (6). <https://doi.org/10.3390/biom11060886>.
- Kumari, S. Chaitanya, Vivek Dhand, and P. Naga Padma. 2021. “Green Synthesis of  
Metallic Nanoparticles: A Review.” *Nanomaterials*, 259–81.  
<https://doi.org/10.1016/b978-0-12-822401-4.00022-2>.
- Lakard, Sophie, Ileana-Alexandra Pavel, and Boris Lakard. 2021. “Electrochemical  
Biosensing of Dopamine Neurotransmitter: A Review.”  
<https://doi.org/10.3390/bios11060179>.

- Lasia, Andrzej. 2013. "Advanced Electrochemistry Interfaces , Thermodynamics , and Electrochemical Techniques Andrzej Lasia Département de Chimie Université de Sherbrooke." *Thesis*, no. February.
- Leftheriotis, G., S. Papaefthimiou, and P. Yianoulis. 2007. "Dependence of the Estimated Diffusion Coefficient of  $\text{Li}_x\text{WO}_3$  Films on the Scan Rate of Cyclic Voltammetry Experiments." *Solid State Ionics* 178 (3–4): 259–63. <https://doi.org/10.1016/j.ssi.2006.12.019>.
- Liu, Ying Ying, David W. Blowes, Carol J. Ptacek, and Laura G. Groza. 2019. "Removal of Pharmaceutical Compounds, Artificial Sweeteners, and Perfluoroalkyl Substances from Water Using a Passive Treatment System Containing Zero-Valent Iron and Biochar." *Science of the Total Environment* 691: 165–77. <https://doi.org/10.1016/j.scitotenv.2019.06.450>.
- Maria, Ana, Oliveira Brett, Silvia H P Serrano, Instituto De Quimica, Universidade De Szo Paulo, and Sbo Paulo. 1997. "Comparison of the Voltammetric Behavior of Metronidazole at a DNA-Modified Glassy Carbon Electrode, a Mercury Thin Film Electrode and a Glassy Carbon Electrode," no. 2: 110–14.
- Martínez-Huitle, Carlos A., Manuel A. Rodrigo, Ignasi Sirés, and Onofrio Scialdone. 2015. "Single and Coupled Electrochemical Processes and Reactors for the Abatement of Organic Water Pollutants: A Critical Review." *Chemical Reviews* 115 (24): 13362–407. <https://doi.org/10.1021/acs.chemrev.5b00361>.

- Mekassa, Birhanu, Priscilla G.L. Baker, Bhagwan Singh Chandravanshi, and Merid Tessema. 2018. "Synthesis, Characterization, and Preparation of Nickel Nanoparticles Decorated Electrochemically Reduced Graphene Oxide Modified Electrode for Electrochemical Sensing of Diclofenac." *Journal of Solid State Electrochemistry* 22 (11): 3607–19. <https://doi.org/10.1007/s10008-018-4071-3>.
- Mendoza, S, E Bustos, J Manriquez, and LA Godinez. 2015. "Volumetric Techniques." *Agricultural and Food Electroanalysis*.
- Mendoza, Sandra, Erika Bustos, Juan Manríquez, and Luis A. Godínez. 2015. "Voltammetric Techniques." *Agricultural and Food Electroanalysis*, 21–48. <https://doi.org/10.1002/9781118684030.ch2>.
- Mirceski, Valentin, Sławomira Skrzypek, and Leon Stojanov. 2018. "Square-Wave Voltammetry." *ChemTexts* 4 (4): 0. <https://doi.org/10.1007/s40828-018-0073-0>.
- N.Al-Rimawi, Leena, Mohammed H. Al-Jabari, Saleh M. Sulaiman, Mazen K. Nazal, and Abdulla S. Idrees. 2022. "Pencil Graphite Synergistic Improvement of Zero-Valent Iron Composite for the Removal of Diclofenac Sodium in Aqueous Solutions: Kinetics and Comparative Study." *Advanced Powder Technology* 33 (6): 103610. <https://doi.org/10.1016/j.appt.2022.103610>.
- Niazi, Ali, Mahtab D.Torkman, and Neda Khorshidi. 2015. "Spectrophotometric Determination of Mefenamic Acid in Biological Samples Using Magnetic Iron Oxide Nanoparticles as a Sorbent for Solid Phase Extraction." *Journal of*

*Nanoanalysis* 2 (2): 46–56.

Panda, Bibhu Prasad, C.S Patro, D Kesharwani, and M.E.B Rao. 2013. “Optimization of Diclofenac Sodium Orodispersible Tablets with Natural Disintegrants Using Response Surface Methodology.” *International Journal of Pharmaceutical Sciences and Nanotechnology* 6 (3): 2172–80.

<https://doi.org/10.37285/ijpsn.2013.6.3.9>.

Panina, Larissa. 2011. “Electromagnetic Sensor Technology for Biomedical Applications.” *Recent Application in Biometrics*. <https://doi.org/10.5772/17746>.

Patil, Roopa H., Praveen N. Naik, and Sharanappa T. Nandibewoor. 2009.

“Mechanistic Investigation of Oxidation of Diclofenac Sodium by Diperoxidocuprate(III) Complex in Aqueous Alkaline Medium.” *Progress in Reaction Kinetics and Mechanism* 34 (4): 329–46.

<https://doi.org/10.3184/146867809X466799>.

Petar TUDJA, a M. Zahirul I. KHAN. 2001. “Thermal Behaviour of Diclofenac Sodium: Decomposition and Melting Characteristics.”

Prakash Rao, and Michael Muller. 2007. “Industrial Oxygen: Its Generation and Use.” *2007 ACEEE Summer Study on Energy Efficiency in Industry*, 124–35.

[http://aceee.org/files/proceedings/2007/data/papers/78\\_6\\_080.pdf](http://aceee.org/files/proceedings/2007/data/papers/78_6_080.pdf).

Pramudita, Daniel, Irwan Iskandar, and Antonius Indarto. 2018. “Nano-Enhanced

Materials for Reclamation of Mine Spoils.” *Bio-Geotechnologies for Mine Site Rehabilitation*, January, 201–14. <https://doi.org/10.1016/B978-0-12-812986-9.00012-9>.

Punyapalakul, Patiparn, Kuntida Suksomboon, Panida Prarat, and Sutha Khaodhiar. 2013. “Effects of Surface Functional Groups and Porous Structures on Adsorption and Recovery of Perfluorinated Compounds by Inorganic Porous Silicas.” *Separation Science and Technology (Philadelphia)* 48 (5): 775–88. <https://doi.org/10.1080/01496395.2012.710888>.

Razmi, Habib, Leyli Ezzati, and Zeynab Khorablou. 2019. “Direct Electrochemical Synthesis of Graphene Oxide/Cobalt Oxide Nanocomposite on Pencil Graphite Electrode for Highly Sensitive and Selective Detection of Insulin in Pharmaceutical Samples.” *Journal of The Electrochemical Society* 166 (12): B961–68. <https://doi.org/10.1149/2.0621912jes>.

Rubio-Retama, J., N. E. Zafeiropoulos, B. Frick, T. Seydel, and E. López-Cabarcos. 2010. “Investigation of the Relationship between Hydrogen Bonds and Macroscopic Properties in Hybrid Core-Shell  $\gamma$ -Fe<sub>2</sub>O<sub>3</sub>-P(NIPAM-AAS) Microgels.” *Langmuir* 26 (10): 7101–6. <https://doi.org/10.1021/la904452c>.

Sataloff, Robert T, Michael M Johns, and Karen M Kost. 2006. *Atkins' Physical Chemistry*.

Scholz, Fritz. 2015. “Voltammetric Techniques of Analysis: The Essentials.”

*ChemTexts* 1 (4): 1–24. <https://doi.org/10.1007/s40828-015-0016-y>.

Sharma, Bharat Bhushan, and Ananth Govind Rajan. 2022. “Interactions Modulate Water Desalination Via.”

Sharma, Swati. 2018. “Glassy Carbon: A Promising Material for Microand Nanomanufacturing.” *Materials* 11 (10). <https://doi.org/10.3390/ma11101857>.

Shigemitsu, Tsukasa, Goro Matsumoto, and Susumu Tsukahara. 1979. “Electrical Properties of Glassy-Carbon Electrodes.” *Medical & Biological Engineering & Computing* 17 (4): 465–70. <https://doi.org/10.1007/BF02447059>.

Singh, Ritu, Virendra Misra, and Rana Pratap Singh. 2011. “Synthesis, Characterization and Role of Zero-Valent Iron Nanoparticle in Removal of Hexavalent Chromium from Chromium-Spiked Soil.” *Journal of Nanoparticle Research* 13 (9): 4063–73. <https://doi.org/10.1007/s11051-011-0350-y>.

Sompornpailin, Dujduan, Chalita Ratanatawanate, Chanchai Sattayanon, Supawadee Namuangruk, and Patiparn Punyapalakul. 2020. “Selective Adsorption Mechanisms of Pharmaceuticals on Benzene-1,4-Dicarboxylic Acid-Based MOFs: Effects of a Flexible Framework, Adsorptive Interactions and the DFT Study.” *Science of the Total Environment* 720: 137449. <https://doi.org/10.1016/j.scitotenv.2020.137449>.

Sravanthi, K., D. Ayodhya, and P. Yadgiri Swamy. 2018. “Green Synthesis,

Characterization of Biomaterial-Supported Zero-Valent Iron Nanoparticles for Contaminated Water Treatment.” *Journal of Analytical Science and Technology* 9 (1). <https://doi.org/10.1186/s40543-017-0134-9>.

Sulaiman, S., and T. Shahwan. 2017. “Mefenamic Acid Stability and Removal from Wastewater Using Bentonite-Supported Nanoscale Zero-Valent Iron and Activated Charcoal.” *Desalination and Water Treatment* 97: 175–83. <https://doi.org/10.5004/dwt.2017.21633>.

Sulaiman, Saleh M., and Mohammed H. Al-Jabari. 2021. “Enhanced Adsorptive Removal of Diclofenac Sodium from Aqueous Solution by Bentonite-Supported Nanoscale Zero-Valent Iron.” *Arab Journal of Basic and Applied Sciences* 28 (1): 51–63. <https://doi.org/10.1080/25765299.2021.1878655>.

Swain, Ranjit Prasad, R. Nagamani, and Satyajit Panda. 2015. “Formulation, in Vitro Characterization and Stability Studies of Fast Dispersing Tablets of Diclofenac Sodium.” *Journal of Applied Pharmaceutical Science* 5 (7): 94–102. <https://doi.org/10.7324/JAPS.2015.50715>.

Takamoto, Satoshi, Nobuo Sakura, Akira Namera, and Mikio Yashiki. 2004. “Monitoring of Urinary Acrolein Concentration in Patients Receiving Cyclophosphamide and Ifosfamide.” *Journal of Chromatography B: Analytical Technologies in the Biomedical and Life Sciences* 806 (1): 59–63. <https://doi.org/10.1016/j.jchromb.2004.02.008>.



- Tambe Patil, Bapusaheb B. 2015. "Wastewater Treatment Using Nanoparticles." *Journal of Advanced Chemical Engineering* 5 (3). <https://doi.org/10.4172/2090-4568.1000131>.
- Townshen, A. 1983. *Principles of Instrumental Analysis. Analytica Chimica Acta*. Vol. 152. [https://doi.org/10.1016/s0003-2670\(00\)84936-3](https://doi.org/10.1016/s0003-2670(00)84936-3).
- Trakal, Lukáš, Martina Vítková, Barbora Hudcová, Luke Beesley, and Michael Komárek. 2019. "Biochar and Its Composites for Metal(Loid) Removal From Aqueous Solutions." *Biochar from Biomass and Waste: Fundamentals and Applications*, January, 113–41. <https://doi.org/10.1016/B978-0-12-811729-3.00007-8>.
- Wan Nor, Wan Fatimah Khairunisa, Siti Kamilah Che Soh, Alyza Azzura Abd Rahman Azmi, Mohd Sukeri Mohd Yusof, and Mustaffa Shamsuddin. 2018. "Synthesis and Physicochemical Properties of Magnetite Nanoparticles (Fe<sub>3</sub>O<sub>4</sub>) as Potential Solid Support for Homogeneous Catalysts." *Malaysian Journal of Analytical Sciences* 22 (5): 768–74. <https://doi.org/10.17576/mjas-2018-2205-04>.
- Wasser, Dvgw-technologiezentrum, and Karlsruher Str. 2013. "Prüfbericht BMBF-Jordanien-Projekt Prüfbericht BMBF-Jordanien-Projekt," no. 000120969.
- Werner, Jeffrey J., Kristopher McNeill, and William A. Arnold. 2005. "Environmental Photodegradation of Mefenamic Acid." *Chemosphere* 58 (10):

1339–46. <https://doi.org/10.1016/j.chemosphere.2004.10.004>.

Widrig, Cindra A., Marc D. Porter, Michael D. Ryan, Timothy G. Strein, and Andrew G. Ewing. 1990. “Dynamic Electrochemistry: Methodology and Application.” *Analytical Chemistry* 62 (12): 101–13. <https://doi.org/10.1021/ac00211a009>.

Yan, David, Martin Z. Bazant, P. M. Biesheuvel, Mary C. Pugh, and Francis P. Dawson. 2017. “Theory of Linear Sweep Voltammetry with Diffuse Charge: Unsupported Electrolytes, Thin Films, and Leaky Membranes.” *Physical Review E* 95 (3): 1–20. <https://doi.org/10.1103/PhysRevE.95.033303>.

Yang, Jinyue, Baohong Hou, Jingkang Wang, Beiqian Tian, Jingtao Bi, Na Wang, Xin Li, and Xin Huang. 2019. “Nanomaterials for the Removal of Heavy Metals from Wastewater.” *Nanomaterials* 9 (3). <https://doi.org/10.3390/nano9030424>.

Yang, Kun, Huabei Peng, Yuhua Wen, and Ning Li. 2010. “Re-Examination of Characteristic FTIR Spectrum of Secondary Layer in Bilayer Oleic Acid-Coated Fe<sub>3</sub>O<sub>4</sub> Nanoparticles.” *Applied Surface Science* 256 (10): 3093–97. <https://doi.org/10.1016/j.apsusc.2009.11.079>.

Yilmaz, Bilal, Selcuk Kaban, Bilge Kagan Akcay, and Ulvihan Ciltas. 2015. “Differential Pulse Voltammetric Determination of Diclofenac in Pharmaceutical Preparations and Human Serum.” *Brazilian Journal of Pharmaceutical Sciences* 51 (2): 285–94. <https://doi.org/10.1590/S1984-82502015000200005>.

- Yu, Haichi, Jianhang Jiao, Qiuju Li, and Yingzhi Li. 2021. "Electrochemical Determination of Diclofenac Sodium in Pharmaceutical Sample Using Copper Nanoparticles/Reduced Graphene Oxide Modified Glassy Carbon Electrode." *International Journal of Electrochemical Science* 16: 1–12.  
<https://doi.org/10.20964/2021.10.19>.
- Yu, Hui, Er Nie, Jun Xu, Shuwen Yan, William J. Cooper, and Weihua Song. 2013. "Degradation of Diclofenac by Advanced Oxidation and Reduction Processes: Kinetic Studies, Degradation Pathways and Toxicity Assessments." *Water Research* 47 (5): 1909–18. <https://doi.org/10.1016/j.watres.2013.01.016>.
- Yu, Shi, and Can Moog Chow. 2004. "Carboxyl Group (-CO<sub>2</sub>H) Functionalized Ferrimagnetic Iron Oxide Nanoparticles for Potential Bio-Applications." *Journal of Materials Chemistry* 14 (18): 2781–86. <https://doi.org/10.1039/b404964k>.
- Zhu, Chengzhou, Guohai Yang, He Li, Dan Du, and Yuehe Lin. 2015. "Electrochemical Sensors and Biosensors Based on Nanomaterials and Nanostructures." *Analytical Chemistry* 87 (1): 230–49.  
<https://doi.org/10.1021/ac5039863>.
- Zia, Muhammad, Abdul Rehman Phull, and Joham Sarfraz Ali. 2016. "Challenges of Iron Oxide Nanoparticles," 49–67.